

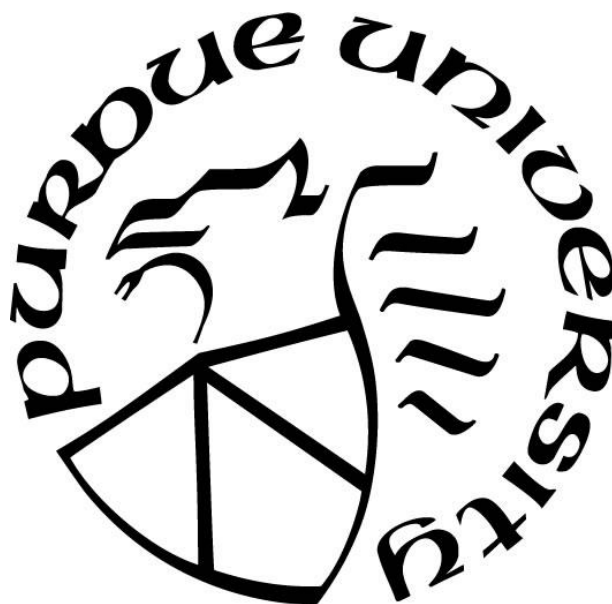
**STRUCTURAL AND FUNCTIONAL STUDIES OF *NEISSERIA*
LACTOFERRIN BINDING PROTEINS**

by
Ravi Yadav

A Dissertation

*Submitted to the Faculty of Purdue University
In Partial Fulfillment of the Requirements for the degree of*

Doctor of Philosophy



Department of Biological Sciences

West Lafayette, Indiana

December 2021

THE PURDUE UNIVERSITY GRADUATE SCHOOL
STATEMENT OF COMMITTEE APPROVAL

Dr. Nicholas Noinaj, Chair

Department of Biological Sciences

Prof. Cynthia V. Stauffacher

Department of Biological Sciences

Dr. Angeline Lyon

Department of Chemistry and Biological Sciences

Prof. Mohamed N. Seleem

Department of Biomedical Sciences and Pathobiology, Virginia Tech

Approved by:

Dr. Jason Cannon

and

Dr. Janice Evans

*Dedicated to my parents, Rampal and Sunita,
my brother Amit, and my cousins Kajal and Kiran*

ACKNOWLEDGEMENT

My time at Purdue University has been filled with fun and exciting memories both in and outside the lab. First and foremost, I would like to thank my advisor, Dr. Nicholas Noinaj. He has constantly guided and provided me with the freedom needed to pursue my lab work. From teaching me how to set up crystal trays, collecting data at the beamline, working on manuscripts, and to asking the right questions, Nick has always been there. Some of my favorite memories include our frequent trips to Chicago for data collection at Advanced Photon Source (APS) and eating at Buona Beef (even though I am a vegetarian). Nick also supported me to attend and present at various training courses, symposiums, and conferences, both at Purdue and across the US. He has been a good mentor outside the lab as well. He taught me how to drive and let me practice with him on our trips to Chicago. I have shared many “firsts” with him: first deep-dish pizza, first whisky shot, and first trip to Krispy Kreme. While I could go on for many pages about all our shared adventures, I ultimately want to say that he has been the best advisor I could have hoped for. I am sincerely grateful for his wonderful mentorship, and I hope we can continue this bond even as I move on from Purdue.

The Noinaj lab members, both past and present, have created an amazing environment to foster friendships, collaboration, and growth, both as scientists and human beings. I would like to thank them for their help and support throughout my time in the lab. I would like to thank Dr. Jeremy Bakelar (now a professor at Dixie State University), Dr. Patrick O’Neil, Richard Bekeris, and Austin Campbell for welcoming me in the lab and encouraging my excitement about the amazing world of membrane proteins. Also, over the years, Robert Stephenson, Dr. Karl Lundquist, Maxine Bi, Hannah Eikelburg, Lindsey Wilson, James Wellnitz, and many more, have been wonderful colleagues, both in their helpful suggestions and comradery. In particular, former undergraduate, Srinivas Govindan, worked with me on my thesis project and helped with purifying protein for subsequent biochemical and biophysical studies. I really appreciated his help with the project and giving me a chance to develop mentoring skills. Finally, I am thankful for the current Noinaj lab members: Runrun Wu, Karthik Srinivasan, Claire Overly, Evan Billings, Shubham Dubey, Dr. Alope Bera, Ryan Peters, and John Stambaugh for their assistance in the lab and giving me helpful feedback for my thesis defense presentation. They have been wonderful friends who were always open to discussions about research, politics, music, religion, and life in general.

As one person cannot do it all, I also had wonderful collaborators to help with research. Dr. Courtney Daczkowski in Prof. Andrew Mesecar's lab at Purdue University performed isothermal titration calorimetry studies to test the effect of LbpB mutations on lactoferrin binding. Dr. Satchal Eramilli in Prof. Anthony Kossiakoff's lab at University of Chicago performed phage-display screening to identify the Fab fragment for structural studies. Several beamline scientists at APS, especially Dr. Srinivas Chakravarthy, have helped with training, data collection, and analysis. Dr. Thomas Klose and Runrun helped with cryo-electron microscopy (cryo-EM) data collection. I also had the pleasure to work with Dr. Rong Huang and her lab members, Dr. Dongxing Chen, Dr. Iredia D. Iyamu, and Dr. Youchao Deng on the structural studies of methyltransferase. Working with them helped me in honing my crystallographic skills. Additionally, I would like to extend a big thank you to Prof. Robert Stahelin for allowing me access to SPR and ITC instruments.

My thesis advisory committee members, Prof. Cynthia Stauffacher, Dr. Angeline Lyon, and Prof. Mohamed Seleem, have provided guidance and valuable suggestions throughout my time as a graduate student. They always ask insightful questions and helped me in recognizing the strengths and weakness in my experimental approach in order to grow as a scientist. Prof. Cynthia Stauffacher has especially been a wonderful teacher, as I have been a student in many of her courses. Additionally, Prof. Carol Post and Prof. Nikolai Skrynnikov were part of my preliminary examination committee and supported me to be confident and think independently as a scientist.

I have been fortunate to have my graduate studies be funded through various fellowships and assistantships. I would like to extend special thanks to the PULSe graduate program for awarding me the Lynn fellowship, to the Executive Vice President for Research and Partnerships (EVPRP) for the PRF fellowship, and to the Department of Biological Sciences for the Bilsland dissertation fellowship. Also, thank you to the Purdue Graduate Student Government (PGSG) for the travel award to attend the Gordon Research Conference. Additionally, my thesis project has been funded through Indiana CTSI.

The graduate school journey is a long one. Many friends, both at and away from Purdue, have made it interesting and fun filled. Dr. Pooja Kesari is one of the smartest and most hard-working people that I know. When I was an undergraduate researcher in Prof. Pravindra Kumar's lab at Indian Institute of Technology Roorkee, she taught me almost everything I knew before joining graduate school. She was my teaching assistant, later a lab colleague, and now she is one

of my closest friends. She deserves a sincere thank you for showing me the ropes of structural and computational biology research. Additionally, although I was assigned to be her mentor as she started graduate school, Surbhi Sood has become one of my best friends. She always listens to my complaints and offers advice. I have really enjoyed our impromptu long drives and carefree exploration of the countryside in Indiana. She motivates me to be a better scientist and a better person overall. She pushes me to get out of my comfort zone, and I am extremely thankful to her for that. Karthik Srinivasan has also been a wonderful friend. We have gone on many hiking trips, road trips (to 20+ states throughout the Midwest and East coast), dinner parties, and so on. I have enjoyed our friendship and exploration of the unknown both in and outside the lab. Additional thanks also go out to Mackenzie Chapman, Clint Gabel, Ali Camara, Luying Chen, Sudhanshu Shekhar, Pranav Salunke, John Hausman, Dr. Vatsal Purohit, Dr. Carlos Brito, Dr. Emma Lendy, Dr. Alisha Dhiman, Dr. Sandeep Ravala, Dr. Rajesh Sharma, Dave Stephens, and Jackie Stephens for making graduate school an enjoyable ride.

I must thank my partner, Kayla Perri, for all the support she has provided over the years. A smart and hard-working graduate student herself, she understood my time commitment to research and weird working hours. She allows me to be my authentic self and goofs around with me. She also encouraged me to write my thesis and assisted with editing it. I would like to thank her family as well for being so kind and welcoming: her parents, Gregg and Lisa Perri, and her sisters.

Finally, I would like to thank my parents, Sunita Devi and Rampal Yadav, my brother, Amit, my aunt, Mamta Devi, my cousins, Kajal and Kiran, and my extended family. This thesis is dedicated to them for making me the person I am today. They have not seen me in person in over 5 years, but they are always there as a constant reminder about why life is beautiful and wonderful. I am forever indebted to them for their sacrifices and allowing me to follow my dreams.

TABLE OF CONTENTS

LIST OF TABLES	10
LIST OF FIGURES	11
LIST OF SYMBOLS, ABBREVIATIONS AND NOMENCLATURE	18
ABSTRACT	20
CHAPTER 1. INTRODUCTION	22
1.1 <i>Neisseria</i>	22
1.2 TonB-ExbB-ExbD inner membrane complex	23
1.3 TonB-dependent transporters	26
1.4 Iron acquisition	27
1.4.1 Transferrin binding proteins	29
1.4.2 Lactoferrin binding proteins	32
1.4.3 Hemoglobin-haptoglobin utilization proteins	37
1.4.4 Hemoglobin receptor	41
CHAPTER 2. STRUCTURAL BASIS FOR LBPB'S ROLE IN IRON IMPORT IN <i>NEISSERIA</i>	43
2.1 Abstract	43
2.2 Introduction	43
2.3 Methods	44
2.3.1 Construct design and cloning	44
2.3.2 Protein expression and purification	45
2.3.3 Formation of the LbpB-lactoferrin complex	47
2.3.4 Small-angle X-ray scattering (SAXS) data collection and processing	47
2.3.5 Crystallization, data collection and data processing	48
2.3.6 Structure determination	48
2.3.7 Solid-phase binding assay	49
2.3.8 Enzyme-linked immunosorbent assays	51
2.3.9 Isothermal titration calorimetry	52
2.3.10 Sample preparation and data collection for cryo-EM	52
2.3.11 Cryo-EM data processing and model building	53
2.4 Results	56

2.4.1	Protein production.....	56
2.4.2	SEC-SAXS characterization of <i>NmLbpB</i>	56
2.4.3	<i>NmLbpB</i> forms a stable complex with lactoferrin.....	58
2.4.4	SEC-SAXS characterization of <i>NgLbpB</i> and <i>NgLbpB</i> -lactoferrin complex.....	60
2.4.5	The N-lobe of <i>NmLbpB</i> binds to lactoferrin.....	61
2.4.6	The X-ray crystal structure of the <i>NmLbpB</i> -lactoferrin complex.....	62
2.4.7	The cryo-EM structure of the <i>NgLbpB</i> -lactoferrin complex	63
2.4.8	Comparison of the <i>NmLbpB</i> -lactoferrin crystal structure with the SAXS structure	65
2.4.9	Structural features of <i>NmLbpB</i> in complex with lactoferrin	66
2.4.10	The binding interface between <i>LbpB</i> and lactoferrin	68
2.4.11	Probing the <i>LbpB</i> -lactoferrin interaction interface using mutagenesis	70
2.5	Discussion and conclusion	73
CHAPTER 3. STRUCTURAL INSIGHT INTO LACTOFERRICIN BINDING TO LBPB		78
3.1	Abstract	78
3.2	Introduction	78
3.3	Methods.....	79
3.3.1	Construct design and cloning.....	79
3.3.2	Protein expression and purification	79
3.3.3	Isothermal titration calorimetry	80
3.3.4	SEC-SAXS analysis of the <i>Nme LbpB</i> - <i>Lfcn</i> complex	81
3.3.5	Biotinylation and streptavidin pull-down	81
3.3.6	Selection of phage display Fabs.....	82
3.3.7	Fab expression and purification	83
3.3.8	Formation of the C-lobe- <i>Lfcn</i> -Fab complexes	83
3.3.9	Crystallization and data collection.....	84
3.3.10	Data processing, structure determination, and refinement.....	84
3.4	Results	84
3.4.1	The C-lobe anionic loops of <i>LbpB</i> contribute to <i>Lfcn</i> binding	84
3.4.2	<i>Lfcn</i> binds to <i>LbpB</i> at a site distinct from lactoferrin.....	88
3.4.3	<i>Lfcn</i> binding induces conformational changes in <i>LbpB</i>	90
3.4.4	Using Fabs as chaperones to determine the <i>LbpB</i> - <i>Lfcn</i> structure	91
3.5	Discussion and conclusion	94

CHAPTER 4. STRUCTURAL INSIGHT INTO IRON EXTRACTION FROM LACTOFERRIN BY LBPA IN <i>NEISSERIA</i>	97
4.1 Abstract	97
4.2 Introduction	97
4.3 Methods	98
4.3.1 Construct design and cloning.....	98
4.3.2 Protein expression and purification	98
4.3.3 Formation of the <i>NmLbpA</i> -lactoferrin complex	99
4.3.4 Grid preparation and cryo-EM data collection	100
4.3.5 Cryo-EM data processing, model building, and refinement	100
4.4 Results	102
4.4.1 Purification of the <i>NmLbpA</i> -lactoferrin complex.....	102
4.4.2 The cryo-EM reconstruction of the <i>NmLbpA</i> -lactoferrin complex	104
4.4.3 The <i>NmLbpA</i> -lactoferrin structure	105
4.4.4 <i>NmLbpA</i> -mediated iron extraction from lactoferrin upon binding.....	108
4.5 Discussion and conclusion	109
CHAPTER 5. SUMMARY AND FUTURE DIRECTIONS.....	113
5.1 Dual function of LbpB	114
5.2 Outstanding questions	115
REFERENCES	116
VITA.....	129
PUBLICATIONS.....	130

LIST OF TABLES

Table 2.1. Data collection, processing, and refinement parameters for the <i>NmLbpB</i> -lactoferrin crystal structure. The final model has been deposited into PDB databases with ID 7JRD.	50
Table 2.2. Cryo-EM data collection, processing, refinement, and validation statistics for the <i>NgLbpB</i> -lactoferrin complex. The final map and model have been deposited into EMDB and PDB databases with ID EMD-24233 and 7N88, respectively.....	54
Table 2.3 Summary of SEC-SAXS parameters. Lactoferrin has a calculated molecular weight (MW) of 76.3 kDa and <i>NmLbpB</i> 79.5 kDa.	58
Table 2.4. Summary of interactions between <i>NmLbpB</i> and lactoferrin. The binding interface information was obtained by QtPISA analysis.	69
Table 2.5. Summary of interactions between <i>NgLbpB</i> and lactoferrin. The binding interface information was obtained by QtPISA analysis.	70
Table 2.6. Summary of ITC data for lactoferrin titrations with <i>NmLbpB</i>	72
Table 3.1. Data collection, processing, and refinement parameters for the <i>NmLbpB</i> C-lobe in complex with Lfcn and MP1/MP2 structures.	86
Table 3.2. Summary of ITC data showing thermodynamic parameters for Lfcn titrations with wild-type and loop-deletion mutants of <i>NmLbpB</i> . ΔH , enthalpy change; K_d , dissociation constant, and ΔS , entropy change.	87
Table 3.3. Summary of thermodynamic parameters for lactoferrin and Lfcn titrations with <i>NmLbpB</i> . These parameters were obtained using a Nano ITC calorimeter (TA Instruments).....	89
Table 3.4. Summary of complementarity-determining regions (CDRs) of Fabs identified through phage-display selection against biotinylated <i>NmLbpB</i> C-lobe.....	92
Table 4.1. Cryo-EM data collection, processing, refinement, and validation statistics for the <i>NmLbpA</i> -lactoferrin complex.....	101

LIST OF FIGURES

Figure 1.1. The ExbB ₅ -ExbD ₂ cryo-EM structure. Orthogonal views of ExbB ₅ -ExbD ₂ cryo-EM structure (PDB ID: 6TYI ³⁷). Two copies of ExbD (red) are positioned within the transmembrane pore of pentameric ExbB.	24
Figure 1.2. The ExbB ₆ -ExbD ₃ cryo-EM structure. Orthogonal views of ExbB ₆ -ExbD ₃ cryo-EM structure (PDB ID: 5ZFU ³²). Three copies of ExbD (red) are positioned within the transmembrane pore of hexameric ExbB.	25
Figure 1.3. The structure of BtuB in complex with TonB. (A) Orthogonal views of BtuB structure (PDB ID: 2GUF ⁴⁹). The structure contains a 22-stranded β -barrel (green) occluded with plug domain (blue). (B) Crystal structure of BtuB in complex with TonB (PDB ID: 2GSK ⁵⁵) showed that TonB-box interacts with TonB (cyan) through β -strand pairing.	26
Figure 1.4. <i>Neisserial</i> outer membrane systems for iron acquisition from host proteins. TbpA/B, transferrin binding protein A/B; LbpA/B, lactoferrin binding protein A/B; HpuA/B, hemoglobin-haptoglobin utilization protein A/B; HmbR, hemoglobin receptor; FbpA/B/C, ferric binding protein A/B/C. The outer membrane proteins bind to host proteins, extract iron/heme and transport across the membrane using proton motive force from TonB-ExbB-ExbD. For Tbp/Lbp systems, iron is transported across the periplasm by FbpA, and across the inner membrane by FbpBC transporter. Figure was created using BioRender.	28
Figure 1.5. The structure of transferrin. Transferrin (PDB ID: 3V83 ⁴³) is composed of N- and C-lobe. Each lobe contains an iron ion (brown sphere) and a carbonate ion (stick).	29
Figure 1.6. The structure of the TbpA-transferrin complex. The C-lobe of transferrin (purple blue) interacts with TbpA (PDB ID: 3V8X ⁴³). The TbpA structure contains a β -barrel (green) domain occluded with plug domain (grey). TbpA plug domain also contains an iron coordination motif EIEYE (red sphere). The extracellular loop 3 helix finger (pale green) positions inside a cleft in transferrin C-lobe.	30
Figure 1.7. The structure of the TbpB-transferrin complex. The C-lobe of transferrin (purple blue) interacts with N-lobe of TbpB (PDB ID: 3VE1 ¹²¹). The iron (brown) and carbonate ions are shown as sphere and stick, respectively.	31
Figure 1.8. The structures of lactoferrin. (A) Crystal structure of holo-lactoferrin (PDB ID 2BJJ ¹²⁴). Lactoferrin is composed of two lobe N-lobe and C-lobe and binds to one iron ion in each lobe. In iron-bound state, lactoferrin attains closed conformation. (B) Crystal structures of apo-lactoferrin (PDB ID: 1LFH ¹²⁵) with N-lobe in open and C-lobe in closed conformation. (C) Crystal structure of apo-lactoferrin (PDB ID: 1DTZ ¹²⁶) with both lobes in open conformation.	33
Figure 1.9. The structures of the N-lobe of LbpB. Crystal structure LbpB N-lobe from <i>Nme</i> (PDB ID 4U9C ¹⁴²) (A) and <i>M. bovis</i> (PDB ID 3UAQ ¹⁴¹) (B). N-lobe is composed of a N-terminal handle domain and an eight-stranded β -barrel domain.	36
Figure 1.10. The dual functions of LbpB. LbpA and LbpB acquire iron from lactoferrin and transport across the membrane using TonB-ExbB-ExbD system generated proton motive force.	

Subsequently, iron is transported across the periplasm and inner membrane by FbpA and FbpBC proteins, respectively. In addition, LbpB binds to host cationic antimicrobial peptide lactoferricin and protects the pathogen from its antimicrobial activity. Figure was created using BioRender. 37

Figure 1.11. The heme binding proteins. (A) Hb is an $\alpha_2\beta_2$ tetramer and contains four heme groups (PDB ID: 5NI1¹⁴⁹). (B) Hb-Hp structure shows that serine protease domain of Hp interacts with $\alpha\beta$ dimer of hemoglobin (PDB ID: 4WJG¹⁵⁵). CCP, complement control protein; Hb, hemoglobin. 38

Figure 1.12. The HpuA-Hb crystal structure. (A) *KdHpuA* structure (PDB ID: 5EC6¹⁶⁶) is composed of an N-terminal β -sandwich and a C-terminal β -barrel domain. These domains contain long surface exposed loops that mediate Hb binding. (B) C-terminal β -barrel domain structure of *NgHpuA* (PDB ID: 5EE2¹⁶⁶). (C) Structure of *KdHpuA* in complex with human Hb $\alpha\beta$ dimer (PDB ID: 5EE4¹⁶⁶). Surface-exposed loops of HpuA interact with both chains of Hb. Hb, hemoglobin. 39

Figure 2.1. Recombinant LbpBs from *Nme* and *Ngo* bind to lactoferrin. (A) *NmLbpB* and *NgLbpB* construct used in the current study. (B) Purification of recombinant *NmLbpB* using size-exclusion chromatography. The red and black arrows represent void and *NmLbpB* elution peaks, respectively. (C) Sodium dodecyl sulphate-polyacrylamide gel electrophoresis (SDS-PAGE) analysis of *NmLbpB* elution peak. The *NgLbpB* was purified using similar procedure. (D) Solid-phase binding assays of holo-lactoferrin binding to recombinantly purified LbpB. 56

Figure 2.2. SAXS characterization of *NmLbpB*. (A) Static-SAXS plots (log-log) of *NmLbpB* at three different concentrations, 3.41 mg/mL [green], 1.7 mg/mL [orange] and 0.85 mg/mL [blue]. The blank is shown in grey. The black arrow points to non-perpendicular intersection of the curve with y-axis suggesting unstable sample. The inset shows Guinier plots for the SAXS curves. The plots have been offset for clarity. The red arrow points to upward curve at low q suggesting aggregation. SEC-SAXS scattering profile of *NmLbpB* (B) and associated Guinier plot (inset), and P(r) function (C). 57

Figure 2.3. Formation of the *NmLbpB*-lactoferrin complex. (A) Size-exclusion chromatography (SEC) chromatographs of *NmLbpB* only, lactoferrin only and *NmLbpB*-lactoferrin complex. A left shift of the complex peak compared to individual components indicates complex formation. (B) Sodium dodecyl sulphate-polyacrylamide gel electrophoresis (SDS-PAGE) analysis of elution peaks from A depicts complex formation associated with peak 3 (lane 4). 58

Figure 2.4. SAXS characterization of the *NmLbpB*-lactoferrin complex. (A) Static-SAXS plots (log-log) of *NmLbpB*-lactoferrin complex at three different concentrations, 0.59 mg/mL [blue], 1.19 mg/mL [orange], and 2.38 mg/mL [green]. The blank is shown in grey. The black arrow points to perpendicular intersection of the curve with y-axis suggesting a stable sample. The inset shows Guinier plots for the SAXS curves. The plots have been offset for clarity. The green arrow points to linear plot at low q suggesting stable monodisperse sample. SEC-SAXS scattering profile of *NmLbpB*-lactoferrin complex (B) and associated Guinier plot (inset), and P(r) function (C). Both Static and SEC-SAXS data show similar results suggesting that *NmLbpB* forms a stable complex with lactoferrin. 59

Figure 2.5. Formation of the *NgLbpB*-lactoferrin complex. (A) Purification of *NgLbpB*-lactoferrin complex using SEC. (C) SDS-PAGE analysis of *NmLbpB*-lactoferrin elution peak from panel C shows complex formation. 60

Figure 2.6. SEC-SAXS characterization of *NgLbpB* alone and in complex with lactoferrin. SEC-SAXS scattering profile (top panel) and associated Guinier plot (middle panel) and pair-distance distribution function $P(r)$ (bottom panel) of *NgLbpB* alone (A) and in complex with lactoferrin (B). The black arrow points to D_{max} in the $P(r)$ function. The SEC-SAXS showed that *NgLbpB* is a monomer in solution and forms 1:1 complex with lactoferrin. 61

Figure 2.7. Solid-phase binding assay to assess lactoferrin binding to *NmLbpB* constructs. The lactoferrin binds to full-length and N-lobe *NmLbpB*, but not C-lobe only. 62

Figure 2.8. The crystal structure of *NmLbpB*-lactoferrin complex. (A) Orthogonal views of *NmLbpB*-lactoferrin complex crystal structure with *NmLbpB* in green, lactoferrin in light blue, iron as brown sphere, and carbonate as yellow stick. The inset shows iron coordination in C-lobe of lactoferrin near the LbpB binding interface. (B) *NmLbpB*-lactoferrin crystal structure colored based on B-factor. Yellow color represents high whereas blue represents low B-factor. The C-lobe of *NmLbpB* has higher B-factor suggesting higher flexibility relative to rest of the molecule. The black arrow indicates the disordered anionic loops. (C) Comparison of calculated scattering curve of *NmLbpB*-lactoferrin structure (red line) with the experimental scattering profile (olive). The top panel display the fit of the data and bottom panel shows the residual. The comparison suggests that crystal structure is in-agreement with ‘in-solution’ structure. 63

Figure 2.9. Cryo-EM data processing workflow for *NgLbpB*-lactoferrin complex. Representative cryo-EM micrograph from 4966 movies. Beam induced motion was corrected and contrast transfer function (CTF) parameters were calculated. Particle were picked, extracted, and classified into 2D classes. Representative 2D class averages show different orientations of the particles. The red arrow indicates the blurred region. The selected particles were filtered through two rounds of *ab-initio* reconstructions followed by heterogeneous refinement. Boxed classes were selected for further processing. Finally, a class containing 127,832 particles was subjected to non-uniform refinement to obtain final 3D reconstruction map at 3.65 Å. Gold-standard Fourier shell correlation (GSFSC) curve of *NgLbpB*-lactoferrin map with the horizontal blue line indicating 0.143 cutoff for resolution estimation. 64

Figure 2.10. The 3.65 Å cryo-EM reconstruction of the *NgLbpB*-lactoferrin complex. (A) Orthogonal views of the *NgLbpB*-lactoferrin complex cryo-EM map with *NgLbpB* (green) and lactoferrin (violet) models docked in it. (B) *NgLbpB*-lactoferrin cryo-EM map surface colored based on local resolution. (C) Visualization of final cryo-EM map quality with map shown in grey transparent surface, secondary structure elements in cartoon and residues shown in sticks. *NgLbpB* and lactoferrin are colored green and violet, respectively. 65

Figure 2.11. Structural comparisons of *NmLbpB* and lactoferrin with uncomplexed structures. Structural alignment of *NmLbpB* (green) with *NmTbpB* (grey) (PDB ID 3V8U⁴³) (A) and *NmLbpB* N-lobe (cyan) (PDB ID 4U9C¹⁴²) (B). (C) Superposition of lactoferrin from the complex (light blue) with holo-lactoferrin (grey) (PDB ID 2BJJ¹²⁴) suggests lactoferrin adopts iron-bound closed conformation. 66

Figure 2.12. The <i>NmLbpB</i> -lactoferrin binding interface. <i>NmLbpB</i> interacts with both the C1 and C2 subdomains of lactoferrin with 1760.8 Å ² buried surface area.	68
Figure 2.13. Probing the lactoferrin binding interface of <i>NmLbpB</i> . (A) The zoomed view of residues along the lactoferrin binding interface in <i>NmLbpB</i> . Residues are colored based on the effect of point mutation on lactoferrin binding. Residues with significant (red), moderate (yellow), and no (green) effect on lactoferrin binding upon mutations are shown in sticks. Representative results of solid-phase binding assay (B) and ELISA (C) to test the effects of point-mutations of <i>NmLbpB</i> on lactoferrin binding.	71
Figure 2.14. ITC analysis of lactoferrin binding to select <i>NmLbpB</i> mutants. ITC analysis of lactoferrin binding to <i>NmLbpB</i> wild-type (A) and point mutants (B-F). Top panels display the raw ITC data whereas bottom panels show the associated isotherms upon single binding site model fitting.....	72
Figure 2.15. Probing the lactoferrin binding interface of <i>NgLbpB</i> . Representative results of solid-phase binding assay (A) and ELISA (B) to test the lactoferrin binding show that point mutants K135E and D139K completely abolish lactoferrin binding as compared to wild-type <i>NgLbpB</i> . D202K mutant <i>NgLbpB</i> also shows significant reduction in lactoferrin binding.	73
Figure 2.16. Structural comparison of <i>NgLbpB</i> -lactoferrin cryo-EM structure with the <i>NmLbpB</i> -lactoferrin crystal structure. (A) <i>NmLbpB</i> -lactoferrin (green/violet) and <i>NgLbpB</i> -lactoferrin (grey) show similar architecture with almost identical binding interface (grey dashed box). Alignment along the LbpB-lactoferrin binding interface showed ~12° rigid body rotation of lactoferrin in <i>NgLbpB</i> -lactoferrin.....	75
Figure 2.17. Comparison of the <i>NmLbpB</i> -lactoferrin and <i>NmTbpB</i> -transferrin structures. Both complexes have similar architecture such that C-lobes of lactoferrin (light blue) and transferrin (grey) interact with N-lobe of <i>NmLbpB</i> (green) and <i>NmTbpB</i> (grey), respectively.	76
Figure 2.18. The role of LbpB in iron import. We propose that LbpB binds to lactoferrin and locks it in an iron-bound closed conformation for delivery to LbpA for iron import.....	77
Figure 3.1. Lfcn binding to <i>NmLbpB</i> . (A) ITC raw data (top) and isotherm (bottom) for Lfcn titration with <i>NmLbpB</i> . Putative Lfcn binding site in <i>NmLbpB</i> shown in cartoon (B) and electrostatic potential surface (C). The surface exposed loops are colored orange. As some of these loops are missing from the structure, an accurate electrostatic potential surface couldn't be created. However, the resolved structure clearly shows a large patch of anionic surface that can accommodate Lfcn binding.....	87
Figure 3.2. Probing the putative Lfcn binding site of <i>NmLbpB</i> . ITC raw data (top) and isotherm (bottom) for Lfcn titration with <i>NmLbpB</i> mutants. Single loop deletions do not have significant effect on Lfcn binding (A-F), however double loop deletion mutant Δ445-526_665-698 significantly reduces Lfcn binding (G).	88
Figure 3.3. <i>NmLbpB</i> binds to both lactoferrin and Lfcn independently. ITC raw data (top) and isotherm (bottom) for Lfcn titration with <i>NmLbpB</i> -lactoferrin complex (A) and lactoferrin titration with <i>NmLbpB</i> in absence (B) and presence (C) of Lfcn. A schematic for the titration experiment is shown on top of each panel. Presence of lactoferrin does not interfere with Lfcn binding to <i>NmLbpB</i> and <i>vice-versa</i>	89

Figure 3.4. SEC-SAXS characterization of *NmLbpB*-Lfcn complex. Comparison of SEC-SAXS scattering profile (top panel) and zoomed view of low q-range (middle panel) and pair-distance distribution function $P(r)$ (bottom panel) of *NmLbpB* alone (green) with *NmLbpB*-Lfcn complex (grey) (A) and *NmLbpB*-lactoferrin alone (olive) and in complex with Lfcn (blue) (B). The black arrow points to the differences in the scattering profile at low q-range (0.05 - 0.08) (middle panel). The SEC-SAXS analysis showed that Lfcn binding induces small conformational change in *NmLbpB*. 90

Figure 3.5. Phage-display Fab screening. (A) Streptavidin pull-down to assess the biotinylation efficiency of *NmLbpB* C-lobe biotinylation. M - marker; 1 - non-biotinylated protein; 2 - unbound; 3 - wash; 4 - final (strep beads); 5 - biotinylated protein; 6 - unbound; 7 - wash; and 8 - final (strep beads). (B) Single-point ELISA assay to assess the unique binders against buffer (background, green), biotinylated *NmLbpB* C-lobe in absence (no peptide, blue) and presence (peptide, red) of Lfcn. The unique binders with sufficient signal labelled MP1-5 were selected for further characterization. 91

Figure 3.6. Purification of the *NmLbpB* C-lobe in complex with Lfcn and Fab fragments. (A) SEC chromatographs of C-lobe alone (black), C-lobe in complex with Lfcn and MP1 (red), and C-lobe in complex with Lfcn and MP2 (green) purification. The elution peak shows a leftward shift in presence of Fab fragments suggesting complex formation. (D) SDS-PAGE analysis of elution peaks from panel C shows co-elution of Fabs with C-lobe. 93

Figure 3.7. The crystal structure of *NmLbpB* C-lobe-Lfcn-MP1 complex. (A) The asymmetric unit contains three C-lobe-Lfcn-MP1 complexes. For clarity, one complex between C-lobe (green) and MP1 (light chain – cyan, heavy chain – magenta) is shown. MP1 primarily binds with handle domain of C-lobe (dashed box). (B) Zoomed view of C-lobe - MP1 binding interface. The interface residues are shown in stick with same color scheme as panel A. 94

Figure 3.8. The crystal structure of *NmLbpB* C-lobe-Lfcn-MP2 complex. (A) The asymmetric unit contains two C-lobe-Lfcn-MP2 complexes. For clarity, one complex between C-lobe (green) and MP2 (light chain – cyan, heavy chain – magenta) is shown. MP2 primarily binds with β -barrel domain of C-lobe (dashed box). (B) Zoomed view of C-lobe - MP2 binding interface. The interface residues are shown in stick with same color scheme as panel A. 95

Figure 3.9. The MP1 and MP2 binding sites. MP1 (grey cartoon) and MP2 (cyan-magenta cartoon) recognize distinct epitopes on *NmLbpB* C-lobe (green surface). The inset shows a zoomed view of C-lobe – MP1/MP2 binding interface. The blue and black rectangles represent the unique binding sites of MP1 and MP2, respectively whereas the red oval shows the overlap in the binding sites. 95

Figure 3.10. A model for the dual functions of LbpB. We propose that LbpB binds to lactoferrin through its N-lobe and shuttles the iron-bound lactoferrin to LbpA for iron extraction. Simultaneously, anionic loops in the C-lobe of LbpB sequester Lfcn peptide and neutralize its antimicrobial effects, thus protecting the bacteria from innate immune defense system. Figure 3.9. The MP1 and MP2 binding sites. MP1 (grey cartoon) and MP2 (cyan-magenta cartoon) recognize distinct epitopes on *NmLbpB* C-lobe (green surface). The inset shows a zoomed view of C-lobe – MP1/MP2 binding interface. The blue and black rectangles represent the unique binding sites of MP1 and MP2, respectively whereas the red oval shows the overlap in the binding sites. 95

Figure 3.10. A model for the dual functions of LbpB. We propose that LbpB binds to lactoferrin through its N-lobe and shuttles the iron-bound lactoferrin to LbpA for iron extraction. Simultaneously, anionic loops in the C-lobe of LbpB sequester LfcN peptide and neutralize its antimicrobial effects, thus protecting the bacteria from innate immune defense system. 96

Figure 4.1. Formation of the *NmLbpA*-lactoferrin complex. (A) Size-exclusion chromatography (SEC) purification of *NmLbpA*-lactoferrin complex. (B) SDS-PAGE analysis of elution peak from panel A shows co-elution of *NmLbpA* and lactoferrin suggesting complex formation. 102

Figure 4.2: The cryo-EM data processing workflow for the *NmLbpA*-lactoferrin complex. Representative cryo-EM micrograph from 2645 movies. Beam induced motion was corrected and contrast transfer function (CTF) parameters were calculated. Particle were picked, extracted, and subjected to 2 rounds of 2D classification. Representative 2D class averages show different orientations of the particles. The selected particles were filtered through four rounds of *ab-initio* reconstructions followed by heterogeneous refinement. Boxed class was selected for further processing. Finally, a class containing 40,173 particles was subjected to non-uniform refinement and local refinement to obtain a map at 4.2 Å. This map was used as template for particle picking. Particles were extracted and processed to yield a final reconstruction at 4.1 Å. GSFSC curve of *NmLbpA*-Lactoferrin map with the horizontal blue line indicating 0.143 cutoff for resolution estimation. 103

Figure 4.3. The cryo-EM map and model of *NmLbpA*-lactoferrin complex. Two different views of the cryo-EM map (A) and fitted model (B) of *NmLbpA* (orange) bound to lactoferrin (marine blue). 104

Figure 4.4. The structure of the *NmLbpA*-lactoferrin complex. *NmLbpA* (orange) binds to lactoferrin (marine blue) at the surface of the pathogen. The iron atom in the lactoferrin is shown as brown sphere. 105

Figure 4.5. Structural features of the *NmLbpA*-lactoferrin complex. (A) *NmLbpA* is composed of an N-terminus plug domain (blue) and C-terminus 22-stranded β -barrel (orange). The plug domain contains a surface exposed loop termed plug loop (green) and an iron-coordination motif (red) in the lumen of the barrel. (B) Lactoferrin (blue) is composed of two lobes, N- and C-lobe. The N-lobe of lactoferrin contains an iron atom (red sphere). 106

Figure 4.6. The *NmLbpA*-lactoferrin binding interface. (A) Lactoferrin C-lobe (marine blue) binds to an extensive interface along with extracellular loops (ECL) of *NmLbpA* (orange). The binding interface can be divided into three regions (dashed boxes and oval). (B) At site 1, C2 subdomain of Lactoferrin interacts with ECL2, 3 and 5 of *NmLbpA*. (C) At site 2, C1 subdomain contacts with ECL5, 7, 8 and 10. Furthermore, plug loop from the lumen of the barrel docks into a hydrophobic pocket of C1 subdomain (inset). (D) A helix in the ECL3 (L3 helix finger) docks at the edge of the cleft between C1 and C2 subdomains of lactoferrin. 107

Figure 4.7. A structural comparison of apo-, holo-, and LbpA-bound lactoferrin. (A) An alignment of lactoferrin N-lobe from the complex (marine) with holo-lactoferrin N-lobe (grey; PDB ID 2BJJ¹²⁴). Structural alignment of lactoferrin C-lobe from the complex (marine) with holo-lactoferrin C-lobe (B), apo-lactoferrin C-lobe (yellow; PDB ID 1DTZ¹²⁶) (C) and both holo- and apo-lactoferrin (D). The curved black arrow represents the rotation of C2 subdomain from closed

to open intermediate conformation. The Red arrow represents the rotation of C2 subdomain from intermediate to fully open conformation. The iron ion is shown as brown sphere..... 108

Figure 4.8. A structural comparison of LbpA-lactoferrin with TbpA-transferrin. (A) Structural superposition of LbpA-lactoferrin (orange/marine blue) structure with TbpA-transferrin structure (PDB ID 3V8X⁴³, grey) shows similar architecture of these complexes. However, there are differences in the conformation of the extracellular loops (B), the plug loop (C), and L3 helix finger (D) 110

Figure 4.9. *In-silico* complex formation between *Nm*LbpA, *Nm*LbpB, and lactoferrin. The N-lobe of lactoferrin from LbpB-lactoferrin structure was aligned with the N-lobe of lactoferrin in LbpA-lactoferrin. The modelled complex suggests that LbpA and LbpB bind to distinct sites on lactoferrin (white oval). In the triple complex, LbpA and LbpB form minimal contact with each other (red arrow). 111

Figure 4.10. A plausible conformation change driver in LbpA. (A) Residue R588 of lactoferrin C2 subdomain undergoes large conformational shift from holo-lactoferrin (grey) to apo-lactoferrin (marine blue) upon binding to LbpA (electrostatic potential surface). The local charge distribution at the L3 helix finger might be causing the conformation transition from holo- to apo-lactoferrin. 112

LIST OF SYMBOLS, ABBREVIATIONS AND NOMENCLATURE

Å	Angstrom (10^{-10} m)
ATP	Adenosine triphosphate
BAM	β -barrel assembly machine
BME	β -mercaptoethanol
BSA	Bovine serum albumin
CCP4	Collaborative computational project number 4
CDC	Center for Disease Control and Prevention
Cryo-EM	Cryo-electron microscopy
CTF	Contrast transfer function
DDM	n-dodecyl- β -D-maltoside
ΔH	Enthalpy change
ΔS	Entropy change
DNA	Deoxyribonucleic acid
e^-	Electron
<i>E. coli</i>	Escherichia coli
ELISA	Enzyme-linked immunosorbent assay
eV	Electronvolt
Fab	Antigen-binding fragment
FbpA/B/C	Ferric binding protein A/B
Fe^{3+}	Ferric ion
FSC	Fourier Shell Correlation
HmbR	Hemoglobin receptor
HpuA/B	Hemoglobin-haptoglobin utilization proteins A/B
HRP	Horseradish peroxidase
IPTG	Isopropyl β -D-thiogalactopyranoside
KCl	Potassium chloride
K_d	Dissociation constant
kV	Kilovolt
mA	milliampere, unit of electric current

mBar	millibar, metric unit of pressure
MR	Molecular replacement
MW	Molecular weight
LB	Luria Bertani
LbpA/B	Lactoferrin binding protein A/B
Lfcn	Lactoferricin
LMNG	Lauryl maltose neopentyl glycol
n	Stoichiometry
NaCl	Sodium chloride
Ngo	<i>Neisseria gonorrhoeae</i>
Ni-NTA	Nickel-nitrilotriacetic acid
nm	nano meter (10^{-9} m)
Nme	<i>Neisseria meningitidis</i>
OD	Optical density
OMP	Outer membrane protein
PBS	Phosphate-buffered saline
PCR	Polymerase chain reaction
PDB	Protein data bank
PISA	Protein Interfaces, Surfaces and Assemblies
PMSF	Phenylmethylsulfonyl fluoride
PVDF	Polyvinylidene difluoride
R _g	Radius of gyration
RMSD	Root-mean-square deviation
Rpm	Revolutions per minutes
SAXS	Small-angle X-ray scattering
SDS-PAGE	Sodium dodecyl sulfate - polyacrylamide gel electrophoresis
SEC	Size-exclusion chromatography
TB	Terrific broth
TbpA/B	Transferrin binding protein A/B
TEV	Tobacco Etch Virus

ABSTRACT

Two species of *Neisseria*, *N. meningitidis* and *N. gonorrhoeae*, are obligate human pathogens that cause meningitis and gonorrhea, respectively. Although generally asymptomatic, *N. meningitidis* can cause invasive meningococcal disease with high mortality rate. Due to emerging antibiotic resistance strains of *N. gonorrhoeae*, the Centers for Disease Control and Prevention (CDC) have designated it as an urgent threat to public health. Therefore, immediate interventions are required for fight against these *Neisseria* pathogens. Iron is an essential nutrient for all bacteria, including *Neisseria*. However, free iron is scarce in human, therefore, *Neisseria* have evolved to acquire iron from host proteins. These iron acquisition systems are immunogenic and important for infection and are promising therapeutic targets.

In the host, lactoferrin sequesters free iron and limits iron availability to pathogens. However, *Neisseria* have evolved machinery to hijack iron directly from lactoferrin itself. Lactoferrin binding proteins, LbpA and LbpB, are outer membrane proteins that together orchestrate the acquisition of iron from lactoferrin. Additionally, LbpB serves an additional role in providing protection against host cationic antimicrobial peptides and innate immune response. Despite studies aimed at deciphering the roles of LbpA and LbpB, the molecular mechanisms underpinning iron acquisition and immune protection remain unknown. Here, we investigated the role of the lactoferrin binding proteins in iron acquisition and protection against cationic antimicrobial peptides. We obtained three-dimensional structures of *Neisseria* LbpA and LbpB in complex with lactoferrin using cryo-electron microscopy and X-ray crystallography. These structures show that both LbpA and LbpB bind to C-lobe of lactoferrin, albeit at distinct sites. Structural analyses show that while lactoferrin maintains its iron-bound closed conformation in the LbpB-lactoferrin complex, it undergoes a large conformational change from an iron-bound closed to an iron-free open conformation upon binding to LbpA. This observation suggest that LbpA alone can trigger the extraction of iron from lactoferrin. Our studies also provide an explanation for LbpB's preference towards holo-lactoferrin over apo-lactoferrin and LbpA's inability to distinguish between holo- and apo-lactoferrin. Furthermore, using mutagenesis and binding studies, we show that anionic loops in the C-lobe of LbpB contribute to binding the cationic antimicrobial peptide lactoferricin. Solution scattering studies of the LbpB-lactoferricin complex showed that LbpB undergoes a small conformational change upon peptide binding.

Together, our studies provide structural insights into the role of the lactoferrin binding proteins in iron acquisition and evasion of the host immune defenses. Moreover, this work lays the foundation for structure-based design of therapeutics against *Neisseria* targeting the lactoferrin binding proteins.

CHAPTER 1. INTRODUCTION

1.1 *Neisseria*

Neisseria are Gram-negative β -proteobacterium that primarily colonize humans. While many *Neisseria* species colonize humans, only two, *N. meningitidis* (Nme) and *N. gonorrhoeae* (Ngo), are pathogenic¹. Nme is a diplococcus, obligate human pathogen that causes meningitis and septicemia. Based on the differences in the capsule polysaccharides, Nme are categorized into 13 serogroups². Six of these serogroups, A, B, C, W, X, and Y, are responsible for the majority of infections³. Nme spreads through either aerosol-borne transmission or physical interactions. In the host, Nme colonizes the nasopharynx in the upper respiratory tract and is present in around 10% of world population asymptotically⁴⁻⁶. During transmission, the bacterium adheres to the epithelium of the nasopharynx and forms microcolony clusters for growth⁷. In asymptomatic colonization, these colonies are cleared by a strong and healthy immune system⁸. Thus, infants, adolescents, and immunocompromised adults are especially susceptible to infection^{9,10}.

In severe infection cases, Nme can cross the epithelium and enter the bloodstream, leading to septicemia¹¹. Nme can also penetrate the blood-brain barrier and cause meningitis¹¹. These infections can be fatal and have a high mortality rate if left untreated (World Health Organization (WHO)). The survivors of meningitis may show long-term neurological defects such as seizures, deafness, blindness, and speech impairment (WHO). Therefore, preventive measures must be taken in the fight against this pathogen. To combat Nme infections, vaccines that target essential virulence factors among the various serotypes have been developed, such as polysaccharide-based vaccines¹². For instance, a quadrivalent vaccine containing polysaccharides from serogroups A, C, W, and Y has been developed and is immunogenic^{13,14}. However, due to poor immunogenicity of its capsule, protein-based vaccines against serogroup B have been developed¹⁵, and there is currently no vaccine against serogroup X. Moreover, although vaccines are available against certain Nme serogroups, the pathogen is still a major public health concern¹⁶⁻¹⁸. Therefore, there is need for effective therapeutics that target Nme.

Ngo is also a diplococcus obligate human pathogen that causes gonorrhea, a sexually transmitted disease. Ngo primarily colonizes the mucosal membranes of the male urethra and female endocervix¹⁹. The gonorrhea infections are manifested differently in male and females. In

males, the infection causes painful discharge and urethritis; a persistent infection can cause sterility¹⁹. In women, the infection remains asymptomatic in ~50% cases. However, an untreated gonorrhea infection in women can result in pelvic inflammatory disease along with chronic pelvic pain, fallopian tube damage, ectopic pregnancy, and infertility¹⁹. In addition to genitals, Ngo can enter the bloodstream and colonize mucosal membranes in other part of the human body, such as eyes, the pharynx, joints, and the brain, as well as cause disseminated gonococcal infections (DGI)²⁰. Subsequently, these colonizations can lead to long-term consequences, including keratoconjunctivitis, pharyngitis, arthritis, and meningitis²⁰. In the past, antibiotics have been used to treat gonorrhea infections. However, Ngo has been able to adapt and develop resistance towards these antibiotics²¹. According to the Centers for Disease Control and Prevention (CDC), Ngo causes 1.14 million new infections each year in the United States alone, and 550,000 are estimated to be drug-resistant infections²². Strains resistant to almost all known antibiotics have been isolated²³. As such, the CDC has categorized drug-resistant Ngo as an “urgent threat;” immediate and aggressive action must be taken to combat the pathogen²². Thus, due to the high adaptability of Ngo towards antibiotics, vaccine development is a potential strategy to combat the increasing drug resistance cases. However, previous attempts of vaccine development against Ngo have not been successful²⁴. Potential factors for failure to develop vaccines against Ngo are: (i) no long-term protection upon natural infection, (ii) high antigenic variation, and (iii) lack of a suitable animal model²⁴. As mentioned above, Ngo is an obligate human pathogen and does not colonize other hosts. In the past, this has made it extremely difficult to create an animal model for gonorrhea infection. However, recently strong progress has been made towards creating animal models to study gonorrhea infections²⁴. The animal model will aid in future studies of complex immune response induced by Ngo, and in screening and optimizing antigens for vaccine development.

1.2 TonB-ExbB-ExbD inner membrane complex

Gram-negative pathogens contain two membranes: an inner cytoplasmic membrane, and an outer membrane. The outer membrane contains proteins responsible for nutrient acquisition, immune evasion, and antibiotic resistance²⁵⁻²⁷. However, there is no energy source present in the outer membrane. Therefore, several outer membrane transporters utilize the proton motive force (PMF) generated from the inner membrane Ton complex²⁸.

The Ton complex is composed of three polytopic inner membrane proteins: TonB, ExbB, and ExbD. The genes for these proteins have been identified in *Neisseria*, but the Ton complex from *E. coli* have been characterized extensively.^{29,30} Although these proteins assemble in the inner membrane and form a pH-dependent cation channel, the exact stoichiometry of the complex has been enigmatic^{31,32}. Several studies have shown evidence for variable stoichiometry of the Ton complex³¹⁻³⁶. Per cell copy number calculation suggested that seven ExbB molecules associate with two ExbB and one TonB³⁵. However, negative-stain electron microscopy studies of the Ton complex showed a 4:1 or 4:2 stoichiometry of ExbB and ExbD, respectively^{33,34}.

Double electron-electron resonance (DEER) spectroscopy studies of the Ton complex showed that a pentamer of ExbB associates with two ExbD and one TonB³¹. Furthermore, crystal structures of ExbB in complex with ExbD at two different pHs showed different occupancies of the ExbD. At pH 7.0, the structure contained a pentamer of ExbB, but no clear density for ExbD was observed³¹. The ExbB is composed of total seven α -helices with three traversing the membrane. The ExbB also contains a large cytoplasmic domain. The ExbB pentamer forms a transmembrane pore that may allow passage of cations for PMF generation³¹. A second crystal structure at pH 4.5 showed one ExbD situated in the transmembrane pore of ExbB pentamer³¹. The presence of ExbD in a low pH structure suggested that ExbD conformation, and thus channel activity, might be modulated by a change in pH. Indeed, the Ton complex shows decreased conductance at a lower pH^{31,32}. Subsequently, a cryo-electron microscopy (cryo-EM) structure of

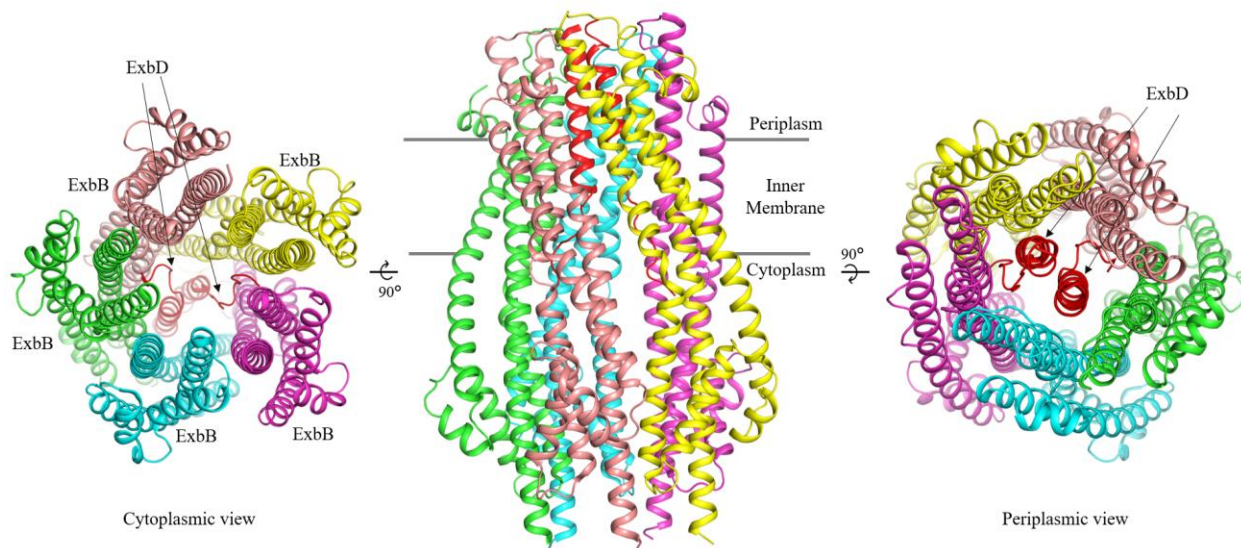


Figure 1.1. The ExbB₅-ExbD₂ cryo-EM structure. Orthogonal views of ExbB₅-ExbD₂ cryo-EM structure (PDB ID: 6TYI³⁷). Two copies of ExbD (red) are positioned within the transmembrane pore of pentameric ExbB.

the ExbB-ExbD complex in a nanodisc showed that two copies of ExbD reside in the transmembrane pore of pentameric ExbB (**Figure 1.1**)³⁷. The observed ExbB₅-ExbD₂ stoichiometry in the cryo-EM structure is consistent with the above-mentioned DEER spectroscopy measurement as well³¹.

Mass-spectroscopy studies of the ExbB-ExbD complex showed the presence of ExbB₅ExbD₁ and ExbB₆ExbD₁ subcomplexes³⁶. Structural characterization of ExbB-ExbD complexes at different pHs demonstrated an equilibrium between pentameric and hexameric ExbB oligomers³². At a lower pH, pentameric ExbB was the more dominant oligomer, whereas at a higher pH hexameric ExbB was present. A cryo-EM reconstruction of the ExbB-ExbD complex at pH 8.0 showed three ExbD inside the transmembrane pore of hexameric ExbB (**Figure 1.2**)³². Therefore, based on structural and functional studies, two models for PMF utilization by the Ton complex have been proposed. First, the ‘electrostatic piston’ model postulates translation motion of the ExbD transmembrane helix inside the channel pore³¹. Second, the ‘rotational model’ suggests the rotation of the ExbD transmembrane helix within the channel pore through structural rearrangement in the ExbB oligomer^{31,32}. Subsequently, the ExbD periplasmic domain interaction with TonB can transduce force to TonB for facilitating transport across the outer membrane³⁸. However, further studies are required to gain insights into the molecular mechanism of the Ton complex function.

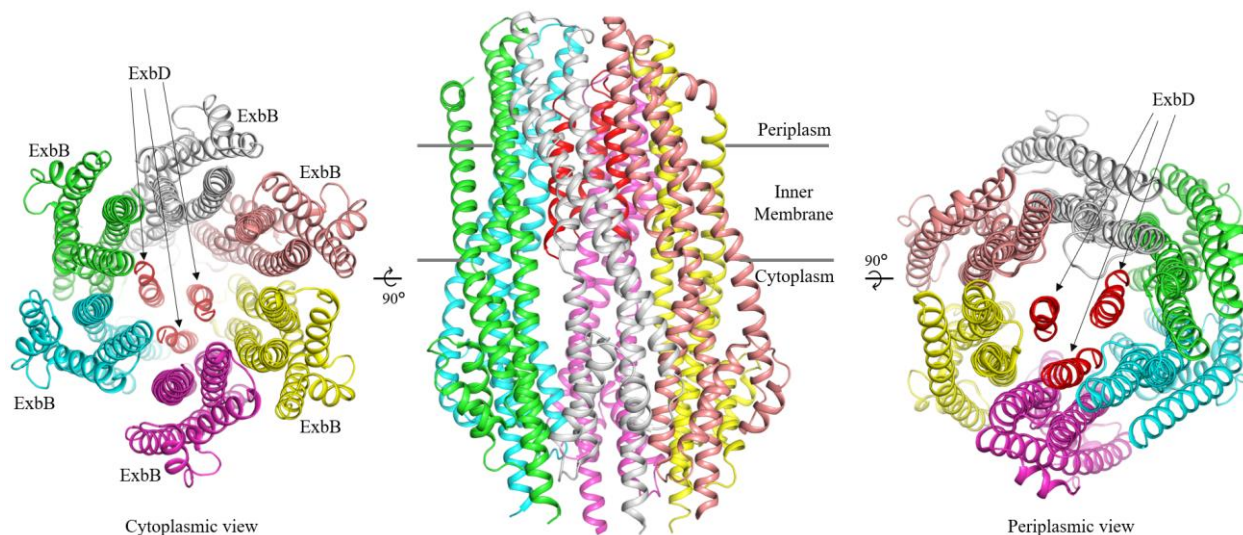


Figure 1.2. The ExbB₆-ExbD₃ cryo-EM structure. Orthogonal views of ExbB₆-ExbD₃ cryo-EM structure (PDB ID: 5ZFU³²). Three copies of ExbD (red) are positioned within the transmembrane pore of hexameric ExbB.

1.3 TonB-dependent transporters

As mentioned above, the outer membranes of Gram-negative bacteria do not have an energy source. Therefore, outer membrane transporters use the PMF generated by the cytoplasmic membrane Ton complex through interaction with TonB²⁸. These transporters are called TonB-dependent transporters, and they mediate transport of various cargo including metal ions, siderophores, vitamin B₁₂, and carbohydrates³⁹. Additionally, these transporters are important virulence factors that mediate pathogenesis and therefore are potential vaccine candidates⁴⁰⁻⁴².

The structures of many TonB-dependent transporters have been determined⁴³⁻⁵¹. They have conserved structural features, including a 22-stranded β -barrel domain with an N-terminal plug domain positioned in the lumen of the barrel (**Figure 1.3A**). The plug domain structure is conserved across all transporters²⁸. Several ligand-bound structures show that the extracellular loops (and extracellular exposed plug domain) form the binding site for ligands²⁸. The substrate binding may induce conformational changes in the transporters^{47,48}. Additionally, the plug-domain contains a TonB-box motif, which is important for TonB binding and subsequent conformational changes for substrate transport^{43,52-54}.

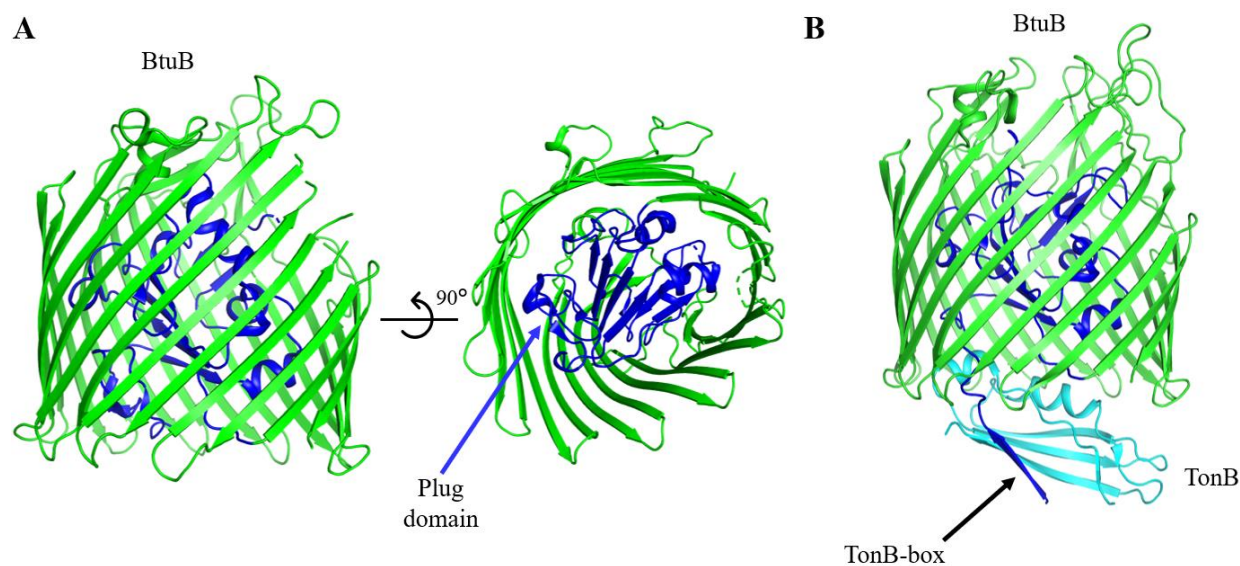


Figure 1.3. The structure of BtuB in complex with TonB. (A) Orthogonal views of BtuB structure (PDB ID: 2GUF⁴⁹). The structure contains a 22-stranded β -barrel (green) occluded with plug domain (blue). (B) Crystal structure of BtuB in complex with TonB (PDB ID: 2GSK⁵⁵) showed that TonB-box interacts with TonB (cyan) through β -strand pairing.

At the periplasmic exposed region of TonB-dependent transporters, the TonB-box motif interacts with TonB through β -strand-pairing (**Figure 1.3B**)⁵⁵. TonB transduces the PMF

generated by the ExbB-ExbD complex and causes conformational changes in the plug domain^{43,53}. The mechanism of PMF transduction from Ton complex to the transporter is still elusive. Two models have been proposed for how TonB induces conformational changes in the plug domain²⁸. First, the ‘pulling hypothesis’ proposes that TonB binding to the TonB-box in the plug-domain leads to partial or complete unfolding of the plug domain, leading to passage of the substrate. Additionally, molecular dynamics simulation studies to simulate the applied force of TonB on the BtuB and TbpA plug domains showed that TonB binding leads to partial unfolding of the plug domain to facilitate substrate transport across the membrane^{43,53}. Single-molecule force microscopy studies of the interaction between BtuB’s TonB-box with TonB showed that the interaction is stable, thereby allowing the plug domain to unfold⁵⁶. Second, the ‘ball and chain model’ of the plug movement suggests that the entire plug domain exits the lumen of the barrel upon interaction with TonB for transport of cargo across the membrane. This model is supported by the observation that the plug domain is highly solvated⁵⁷. Furthermore, observations that the β -barrel of FhuA was able to transport ferrichrome siderophores without the plug domain suggests that the plug domain may exit the barrel during the transport^{58,59}. The FepA plug domain residue labelling experiments during transport also supported the plug domain exit model⁶⁰. Together, these models partially explain how substrates are transported across the outer membrane by TonB-dependent transporters, but further studies are still required to understand the full-range of conformational changes induced during substrate transport by TonB-dependent transporters.

1.4 Iron acquisition

Invading pathogens must acquire essential nutrients, such as iron, from their hosts in order to survive^{61,62}. In the human host, iron is scarce in the extracellular environment^{63,64}. Instead, the majority of iron is stored in the intracellular protein, ferritin. Additionally, iron binding proteins, transferrin and lactoferrin, sequester free iron and thus limit the iron availability for pathogens, a process termed nutritional immunity^{65,66}. In the bloodstream, transferrin chelates and delivers iron to different cellular tissues throughout the body⁶¹. Conversely, lactoferrin is highly abundant in mucosal surfaces, and sequesters iron with higher affinity than transferrin⁶¹. Lactoferrin also retains iron even in a low pH environment and forms part of the host innate immune response^{67,68}.

To circumvent the nutritional immunity and obtain iron, invading pathogens secrete siderophores, which are small molecules that chelate iron. These siderophores bind to available

iron with very high affinity and are subsequently internalized by the pathogens for iron extraction⁶⁹⁻⁷¹. Interestingly, although *Neisseria* can obtain iron from siderophores, they lack the siderophore biosynthesis machinery^{72,73}. During pathogenesis, siderophore-based iron acquisition is insufficient for obtaining an adequate iron supply. Therefore, *Neisseria* have evolved mechanisms to obtain iron from human iron-containing proteins^{74,75}. These iron acquisition systems contribute to *Neisseria* being human-specific.

Neisseria utilize four different iron acquisition systems to obtain iron from human iron-containing protein (**Figure 1.4**). All these systems contain an integral outer membrane protein, whereas only three systems have an additional surface exposed lipoprotein. Transferrin binding proteins, TbpA and TbpB, extract iron from human transferrin, whereas lactoferrin binding proteins, LbpA and LbpB, extract from human lactoferrin^{25,76-80}. Hemoglobin-haptoglobin utilization proteins, HpuA and HpuB, extract heme group from the hemoglobin-haptoglobin

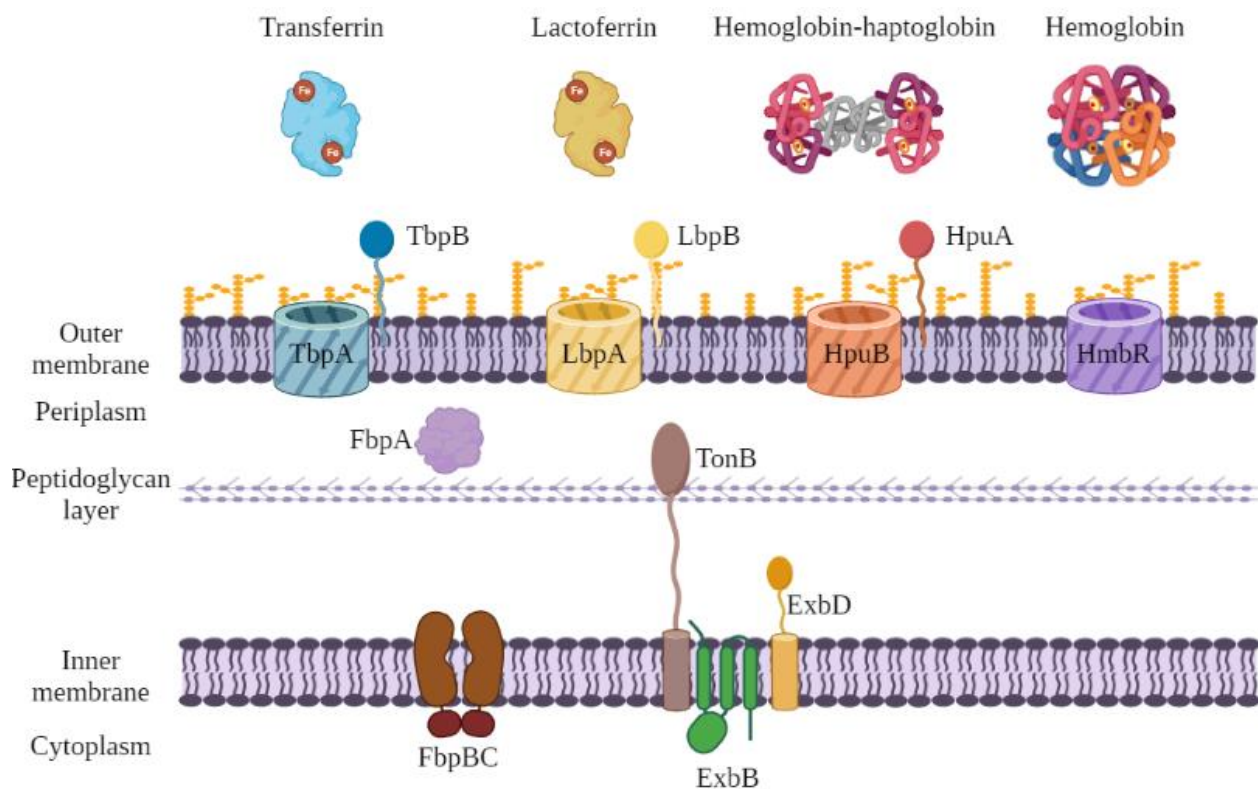


Figure 1.4. *Neisserial* outer membrane systems for iron acquisition from host proteins. TbpA/B, transferrin binding protein A/B; LbpA/B, lactoferrin binding protein A/B; HpuA/B, hemoglobin-haptoglobin utilization protein A/B; HmbR, hemoglobin receptor; FbpA/B/C, ferric binding protein A/B/C. The outer membrane proteins bind to host proteins, extract iron/heme and transport across the membrane using proton motive force from TonB-ExbB-ExbD. For Tbp/Lbp systems, iron is transported across the periplasm by FbpA, and across the inner membrane by FbpBC transporter. Figure was created using BioRender.

complex^{81,82}. Lastly, the hemoglobin receptor (HmbR) binds to hemoglobin and obtains heme group without the need for a lipoprotein⁸³. These iron acquisition systems are TonB-dependent transporters, and they utilize the PMF that is generated by the inner membrane Ton complex for the transport of iron/heme groups across the outer membrane^{28,53}. Subsequently, TbpA/LbpA transfer the iron to ferric binding protein A (FbpA) which further shuttles iron across the periplasm to the inner membrane⁸⁴. The iron is then transported across the inner membrane to the cytoplasm by the FbpBC membrane transporter⁸⁴. Therefore, since iron acquisition systems are essential for Neisserial infections, they are also potential vaccine targets^{42,85,86}. The research discussed in this thesis focuses on elucidating the molecular mechanism of the lactoferrin binding proteins LbpA and LbpB in mediating Neisserial pathogenesis.

1.4.1 Transferrin binding proteins

Transferrin is a serum iron-binding glycoprotein that plays important role in iron metabolism⁸⁷. Transferrin binds to free iron in serum and transports it to different cellular tissues for iron delivery. Although transferrin binds to iron with high affinity, it can release iron at acidic pH 5.6 leading to conformational changes in the structure⁸⁸. Additionally, transferrin plays an integral part in innate immune system by sequestering free iron thus limiting available iron for pathogen⁶⁶.

Transferrin has a bi-lobed structure composed of an N-lobe and a C-lobe connected through a short linker (**Figure 1.5**)^{43,89}. Each lobe is composed of two subdomains termed N1 and N2 for N-lobe

and C1 and C2 for C-lobe. Transferrin can bind two irons in total, one in each lobe. A carbonate ion is also present in each lobe to balance electrostatic charges upon iron binding. The iron binding site is formed inside a cleft between two subdomains and composed of residues D63 (D392), Y95 (Y426), Y188 (Y517), and H249 (H585) (C-lobe residues shown in parenthesis), contributed from both subdomains⁴³. Transferrin residues K206 and K296 (di-lysine motif) in the N-lobe and K534,

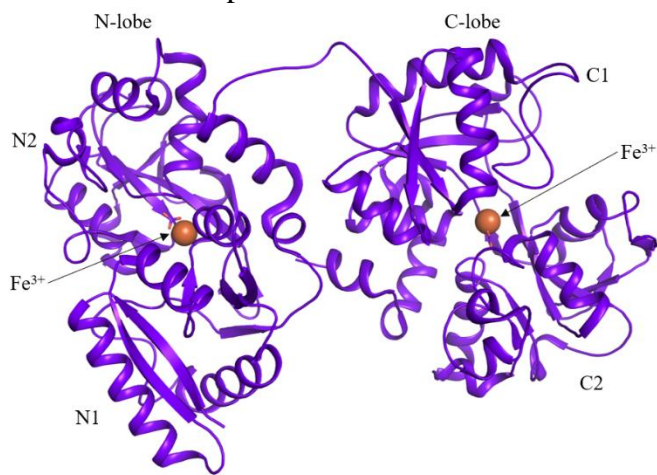


Figure 1.5. The structure of transferrin. Transferrin (PDB ID: 3V83⁴³) is composed of N- and C-lobe. Each lobe contains an iron ion (brown sphere) and a carbonate ion (stick).

R632 and D634 in the C-lobe are important for pH-dependent iron release^{90,91}. Additionally, H349 is important for receptor-mediated iron release in response to pH change⁹².

All Nme and Ngo strains can utilize transferrin as an iron source for growth⁹³. *Neisseria* encodes for surface-exposed receptors to acquire iron from transferrin that are specific to human transferrin^{80,94-96}. Transferrin binding proteins are important virulence factors that are required for gonococcal infections^{97,98}. Additionally, transferrin binding proteins are immunogenic and are promising vaccine candidates^{42,97,99-102}. The transferrin binding protein system is composed of two proteins: TbpA and TbpB^{103,104}.

Transferrin binding protein A

Transferrin binding protein A (TbpA) is a TonB-dependent transporter involved in iron acquisition from human transferrin¹⁰⁵. TbpA is essential for *Neisserial* infection in humans; it is highly conserved across different strains with minimum phase variation^{98,106}. A TbpA deficient Nme strain M982 was avirulent in a mice model¹⁰⁷. TbpA does not distinguish between apo- or holo-transferrin^{108,109}. Although TbpA alone can bind to transferrin and extract iron, the iron uptake is increased in the presence of TbpB^{103,107,110}. Therefore, both TbpA and TbpB are required for efficient iron acquisition^{111,112}. In a male urethra gonococcal infection model, the patient sera contained antibodies against TbpA⁹⁷.

Additionally, an engineered TbpB with TbpA epitopes insertions produced bactericidal antibodies that targeted TbpA and inhibited Ngo colonization in the lower genital tract of female mice⁴².

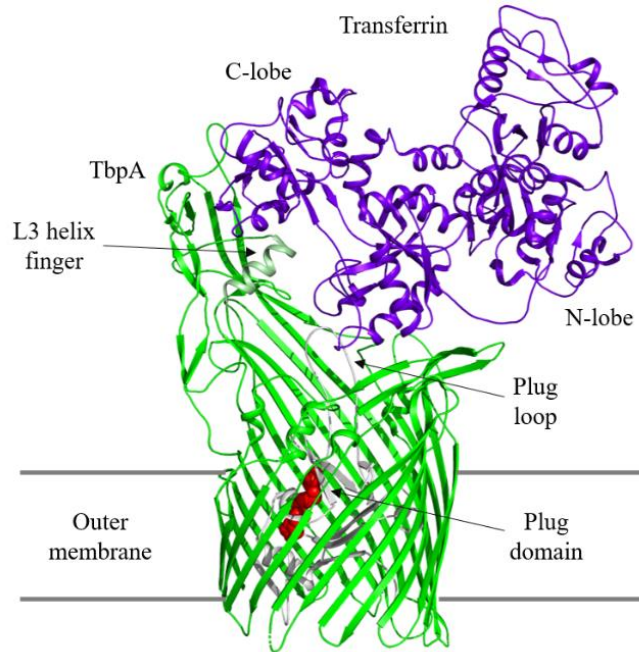


Figure 1.6. The structure of the TbpA-transferrin complex. The C-lobe of transferrin (purple blue) interacts with TbpA (PDB ID: 3V8X⁴³). The TbpA structure contains a β -barrel (green) domain occluded with plug domain (grey). TbpA plug domain also contains an iron coordination motif EIEYE (red sphere). The extracellular loop 3 helix finger (pale green) positions inside a cleft in transferrin C-lobe.

The TbpA structure contains a 22-stranded transmembrane β -barrel occluded with an N-terminal plug domain (**Figure 1.6**)⁴³. The amino-terminus of the TbpA plug domain is exposed to the periplasmic space for TonB binding at the TonB-box motif that is essential for iron transport^{43,113}. On the extracellular side, transmembrane β -strands of TbpA are connected through long extracellular loops, which form the binding site for human transferrin⁴³. The extracellular loop 3 helix is important for iron extraction from transferrin^{43,85}. This loop 3 helix displays sequence variation among different strains and can tolerate mutations without significant effects on TbpA function, whereas deletion of the entire loop 3 helix abolishes transferrin binding and iron extraction^{43,85,114}. The plug domain contains an EIEYE motif that coordinates iron during transport across the outer membrane¹¹⁵. While no structures of TbpA in complex with holo-transferrin have been reported, the TbpA crystal structure in complex with apo-transferrin showed that the C-lobe of transferrin binds to TbpA (**Figure 1.6**)⁴³. In the absence of iron, the transferrin adopts an intermediate open conformation. Based on X-ray structures and molecular dynamic simulations, it was hypothesized that TbpA causes a conformational change in the C-lobe of transferrin for extracting iron. Iron is then transported across the membrane through a pore created by TonB induced conformational changes in the plug domain⁴³.

Transferrin binding protein B

Transferrin binding protein B (TbpB) is a lipoprotein present at the surface of *Neisseria* that is involved in iron piracy from human transferrin⁸⁰. Although TbpB is not essential for iron acquisition from transferrin, the presence of TbpB increases iron uptake efficiency^{85,107,110,111}. As mentioned above, TbpA can bind to both apo- and holo-transferrin, whereas TbpB shows preference for holo-transferrin^{108,109,116}. TbpB is highly immunogenic and can produce cross-reactive bactericidal antibodies^{99,100,102}. For example, a mutant form of TbpB from *Haemophilus parasuis* was immunogenic in a pig model and displayed 80% survival against the highly virulent *H. parasuis*

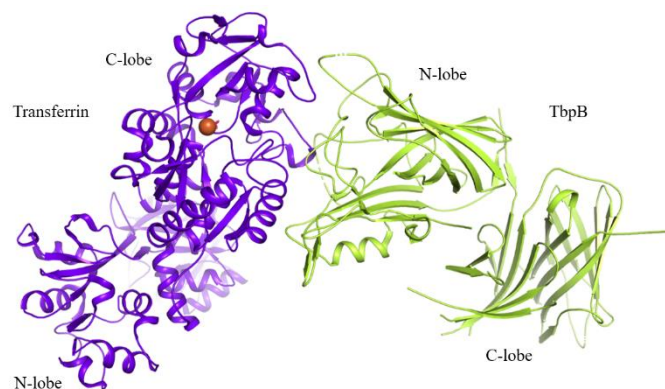


Figure 1.7. The structure of the TbpB-transferrin complex. The C-lobe of transferrin (purple blue) interacts with N-lobe of TbpB (PDB ID: 3VE1¹²¹). The iron (brown) and carbonate ions are shown as sphere and stick, respectively.

strain 174¹¹⁷. Similarly, engineered TbpB showed protection against Nme invasive infection and Ngo colonization in mice models⁴².

TbpB is composed of two structurally similar lobes: the N-lobe and the C-lobe (**Figure 1.7**)^{43,118}. The N-lobe contains an N-terminus handle domain packed against an eight-stranded β -barrel domain⁴³. The β -barrel and handle domains contain large surface exposed loops that may participate in transferrin binding. The C-lobe also consists of a similar domain arrangement. As such, the N-lobe and the C-lobe are connected through a linker, and both lobes interact with each other with high affinity (K_D value of 47 nM)¹¹⁹.

TbpB is surface exposed and can bind to transferrin in the absence of TbpA^{111,120}. The crystal structure of TbpB in complex with transferrin provided valuable insights into TbpB binding to transferrin and its role in iron import (**Figure 1.7**)¹²¹. In the TbpB-transferrin complex structure, the N-lobe of TbpB selectively binds to an iron-loaded C-lobe of human transferrin¹²¹. This observation is consistent with prior biophysical studies of TbpB. Isothermal titration calorimetry studies of the individual domains of TbpB showed that the N-lobe of TbpB binds to transferrin¹¹⁹. The surface-exposed loops of the TbpB N-lobe form an extensive binding interface with both the C1 and C2 subdomains of transferrin with $\sim 1450 \text{ \AA}^2$ buried surface area (**Figure 1.7**)¹²¹. Structural alignment of TbpB and transferrin from the complex with unbound structures also showed an almost identical conformation¹²¹. Therefore, the authors proposed that the complex formation stabilizes the iron-bound conformation of transferrin by modulating the pK_a of transferrin H349¹²¹. Although both TbpA and TbpB bind to the C-lobe of transferrin, the binding sites are non-overlapping and distinct^{43,108,121}. For iron acquisition, the TbpB selectively binds to holo-transferrin and stabilizes transferrin in an iron-bound conformation for subsequent processing by TbpA^{119,121}.

1.4.2 Lactoferrin binding proteins

Lactoferrin is a multifunctional protein that displays antibacterial, antifungal, antiviral, antioxidant, and immune modulation activities^{68,122}. Lactoferrin is present in milk, saliva, mucosal surfaces, and neutrophil extracellular trap (NET)⁶¹. Lactoferrin chelates free iron with very high affinity ($K_D \sim 10^{-22} \text{ M}$) and can withhold iron even at low pH, thereby greatly limiting the free iron that is available for invading pathogens⁶⁷. Therefore, lactoferrin forms an important part of the innate immune system¹²².

Lactoferrin is a member of the transferrin family and plays an integral role in host nutritional immunity. Lactoferrin is composed of two structurally similar lobes, the N-lobe and the C-lobe. Furthermore, each lobe is composed of two subdomains, N1 and N2 for the N-lobe, and C1 and C2 for the C-lobe. One iron ion binds in each lobe of lactoferrin. Iron binding to lactoferrin is dependent on the binding of a carbonate (CO_3^{2-}) ion¹²³. The three-dimensional structure of lactoferrin showed that two lobes are connected through an α -helix¹²⁴⁻¹²⁶ (**Figure 1.8**). In the holo-lactoferrin structure, two irons, one in each lobe, are present and are coordinated by residues D61

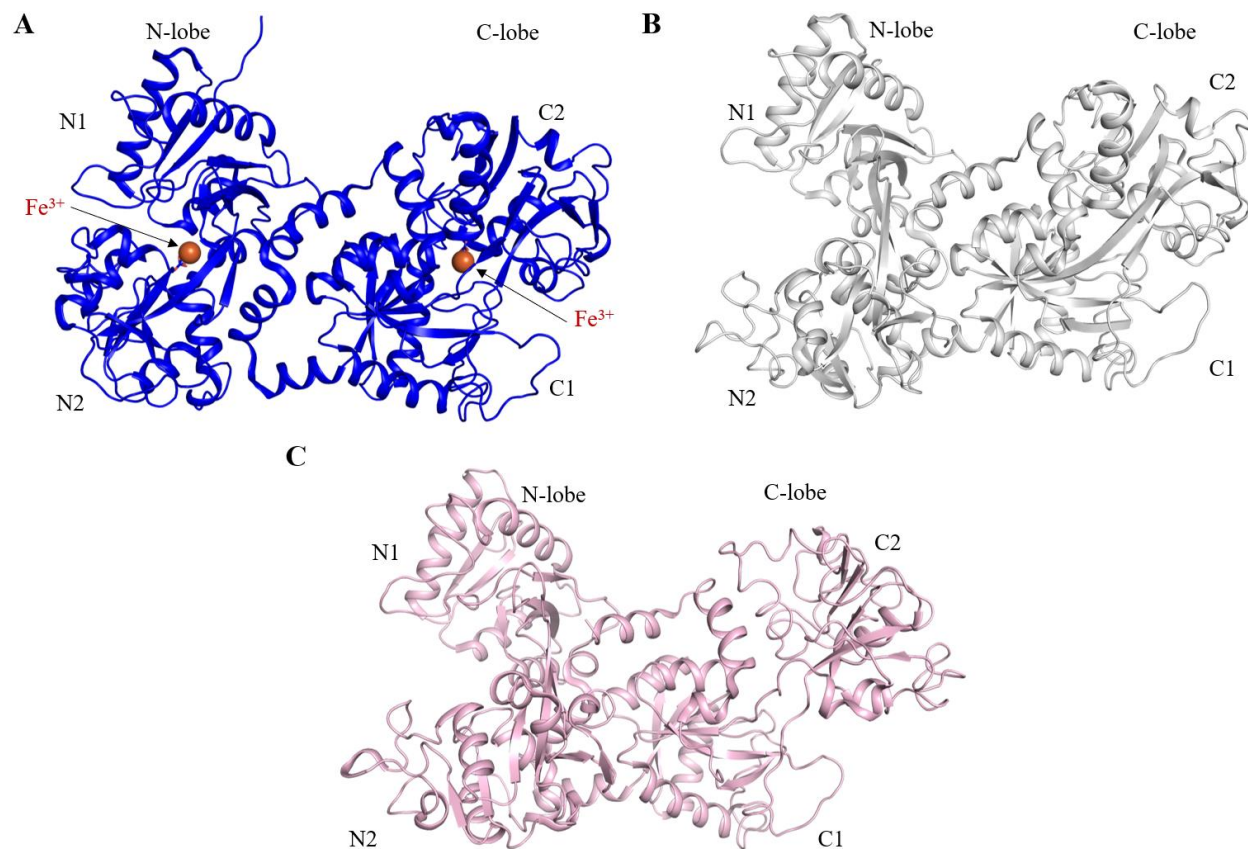


Figure 1.8. The structures of lactoferrin. (A) Crystal structure of holo-lactoferrin (PDB ID 2BJJ¹²⁴). Lactoferrin is composed of two lobe N-lobe and C-lobe and binds to one iron ion in each lobe. In iron-bound state, lactoferrin attains closed conformation. (B) Crystal structures of apo-lactoferrin (PDB ID: 1LFH¹²⁵) with N-lobe in open and C-lobe in closed conformation. (C) Crystal structure of apo-lactoferrin (PDB ID: 1DTZ¹²⁶) with both lobes in open conformation.

(N1), Y93 (N2), Y193 (N2), and H254 (N1) in the N-lobe, and D396 (C1), Y436 (C2), Y529 (C2), and H598 (C1) in the C-lobe, as well as an additional carbonate ion. The residue number is based on the recombinant human lactoferrin structure (PDB ID 2BJJ¹²⁴). Additionally, the iron-bound holo-lactoferrin conformation is defined as a closed conformation (**Figure 1.8A**).

Upon release of iron, lactoferrin undergoes large conformational changes. The crystal structure of apo-lactoferrin showed that the N2 subdomain undergoes a 54° rigid-body rotation with respect to the N1 subdomain, leading to an open conformation¹²⁵ (**Figure 1.8B**). In this structure, the C-lobe maintained a closed conformation, even in the absence of bound iron. Subsequently, various structures of apo-lactoferrin were obtained, which demonstrated that both lobes can have a diverse range of either open or closed conformations^{126,127} (**Figure 1.8C**). Thus, these structures provided important insights into the dynamics of the lactoferrin structure, as they suggested that apo-lactoferrin can adapt to multiple conformations.

Proteolytic cleavage of lactoferrin by pepsin in acidic conditions releases a peptide fragment that exhibits a wide range of biological activities¹²⁸. For example, peptide derived from bovine lactoferrin (LfcnB) shows potent antibacterial, antiviral, antifungal, and anticancer activities¹²⁹. Human lactoferrin derived peptide LfcnH also showed antibacterial activity¹²⁹. These peptides damage or kill the invading pathogens by disrupting the membrane arrangement through an unknown mechanism. A peptide containing 11 N-terminus residues (GRRRRSVQWCA) of human lactoferrin (lactoferricin, Lfcn or hLf(1-11)) showed antibacterial activity against *Staphylococcus aureus*¹³⁰, *Acinetobacter baumannii*¹³¹, and Nme¹³². The multifunctional roles of lactoferrin in iron-chelation and lactoferricin peptide release also supports lactoferrin's important role in the innate immune system.

As mentioned above, *Neisseria* must obtain iron from human iron-containing proteins. All Nme and ~50% of Ngo can utilize lactoferrin as an iron source to sustain growth, thereby circumventing host nutritional immunity¹³³. Additionally, characterization of Ngo FA19 strains that were deficient in iron acquisition from lactoferrin revealed that Ngo produce a specific receptor for lactoferrin⁹⁶. Subsequently, two lactoferrin-binding proteins were identified on the surface of *Neisseria* termed LpbA⁷⁹ and LpbB¹³⁴.

Lactoferrin binding protein A

Lactoferrin binding protein A (LbpA) is a TonB-dependent transporter that is localized in the outer membrane of *Neisseria*. LbpA shows strong specificity towards human lactoferrin over bovine lactoferrin, human transferrin, or human hemoglobin⁷⁹. However, LbpA does not differentiate between iron-free apo or iron-loaded holo-lactoferrin⁷⁹. Solid-phase binding assays of LbpA with bovine transferrin/human lactoferrin chimeric proteins showed that both the C1 and

C2 subdomains of the human lactoferrin C-lobe bind to LbpA¹³⁵. LbpA is present in all Nme strains, as well as in ~50% of Ngo clinical isolates^{40,133}. While LbpA is required and sufficient for iron acquisition from lactoferrin, iron uptake is reduced in the absence of LbpB^{78,136}.

Human challenge experiments for gonococcal infections were conducted to demonstrate the role of lactoferrin binding proteins in *Neisseria* pathogenesis⁴⁰. Ngo mutants that can utilize either transferrin (Lf⁻Tf⁺), lactoferrin (Lf⁺Tf⁻), both (Lf⁺Tf⁺), or neither (Lf⁻Tf⁻) as iron sources were used to inoculate the urethra of male volunteers. As expected, the Lf⁻Tf⁻ strain was not able to cause an infection. The gonococcal Lf⁺Tf⁻ mutant was able to grow by using lactoferrin as the sole iron source; it infected six of the eight volunteers. Interestingly, the Lf⁺Tf⁻ or Lf⁻Tf⁺ mutants had similar rates of infection. Additionally, co-infection with Lf⁻Tf⁺ and Lf⁺Tf⁺ gonococcal strains resulted in infection in five out of twelve volunteers. However, all the infected patients were Lf⁺Tf⁺ positive, which suggested that the ability to obtain iron from both lactoferrin and transferrin, rather than just transferrin, provided a selective advantage during pathogenesis.

Based on the sequence similarity of LbpA to other closely related structures at that time, an early topology model for LbpA was previously proposed⁸⁶. Like other TonB-dependent transporters, the model of LbpA contains an N-terminal plug domain that is situated in the lumen of the C-terminal 22 stranded β -barrel with 11 surface-exposed loops. Later, a homology model of LbpA based on the reported structure of TbpA predicted a similar domain and structural arrangement¹³⁷. LbpA is highly conserved among Nme strains, apart from the predicted surface exposed loop positions 200-340 and 550-590¹³⁸. Additionally, while mice immunized with outer membrane vesicles (OMVs) from Nme strain H44/76 produced LbpA-specific antibodies, these antibodies showed poor cross-reactivity with different Nme strains⁸⁶. Moreover, human convalescent sera do not contain any LbpA-specific antibodies⁸⁶.

Lactoferrin binding protein B

Lactoferrin binding protein B (LbpB) is a surface-exposed lipoprotein that is tethered to the outer membrane by a lipid anchor. Like LbpA, LbpB also displays species specificity¹³⁹. LbpB selectively binds to human lactoferrin over bovine lactoferrin. Also, unlike LbpA, LbpB shows preferential binding to holo-lactoferrin over apo-lactoferrin¹¹⁶. Although LbpB increases the uptake of iron from lactoferrin, it is not essential, as LbpA alone is sufficient for iron acquisition^{78,136,140}.

Prior to the work presented in this thesis, no full-length structure of LbpB was reported. However, based on its sequence homology with TbpB, LbpB is predicted to be composed of two lobes, the N-lobe and the C-lobe¹³⁷. Crystal structures of the N-lobe of LbpB from *Moraxella bovis* and Nme showed that the N-lobe is composed of a N-terminal handle domain packed against an eight-stranded β -barrel^{141,142} (**Figure 1.9**). These two structures have an almost identical arrangement of the handle and β -barrel domains, and they showed a significant similarity with the TbpB N-lobe¹²¹. While no structure was available during this time, the C-lobe was predicted to have a handle domain and β -barrel domains, similar to the N-lobe¹³⁷. The LbpB C-lobe also contains two large stretches of negatively charged residues⁷⁸. These charged residues have been previously postulated to be involved in lactoferrin binding^{78,143}.

There is conflicting information about how LbpB and lactoferrin interact. For instance, computational docking studies of Nme LbpB with human lactoferrin predicted that the N-lobe of lactoferrin binds to the LbpB N-lobe¹⁴². However, homology

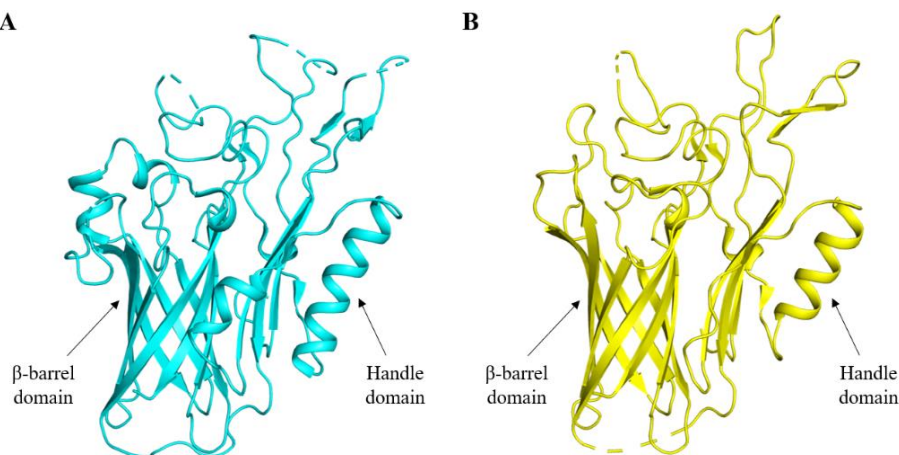


Figure 1.9. The structures of the N-lobe of LbpB. Crystal structure LbpB N-lobe from Nme (PDB ID 4U9C¹⁴²) (A) and *M. bovis* (PDB ID 3UAQ¹⁴¹) (B). N-lobe is composed of a N-terminal handle domain and an eight-stranded β -barrel domain.

modelling studies of LbpB predicted that the C-lobe of lactoferrin binds to the N-lobe of LbpB¹³⁷. On the other hand, a recent study reported that both lobes of LbpB can bind to lactoferrin¹¹⁶. Still, crosslinking mass-spectroscopy and site-directed mutagenesis studies suggested that the N-lobe of LbpB binds to the C-lobe of lactoferrin¹¹⁶. In addition to a 1:1 complex between LbpB and lactoferrin, a higher order complex was also identified¹¹⁶. Therefore, due to the conflicting results for LbpB's interaction with lactoferrin, an experimental structure of the LbpB-lactoferrin complex is essential in order to understand the role of LbpB in iron import.

Almost 60% of the total LbpB produced by Nme was released from the bacterial surface by the proteolytic activity of a membrane bound autotransporter, NalP¹⁴⁴. The release of LbpB

protects Nme against the LbpB-specific bactericidal antiserum. This observation suggested that LbpB may play a role in evading the human immune response. Indeed, LbpB provides protection against the human lactoferrin-derived cationic antimicrobial peptide lactoferricin (Lfcn), which is mediated by negatively charged residues in the C-lobe^{132,145}. Furthermore, LbpB was able to extend protection against other natural and synthetic cationic antimicrobial peptides as well¹⁴⁶. These observations suggested that LbpB might have dual functions during pathogenesis in (1) iron import and (2) evading the host immune response (**Figure 1.10**).

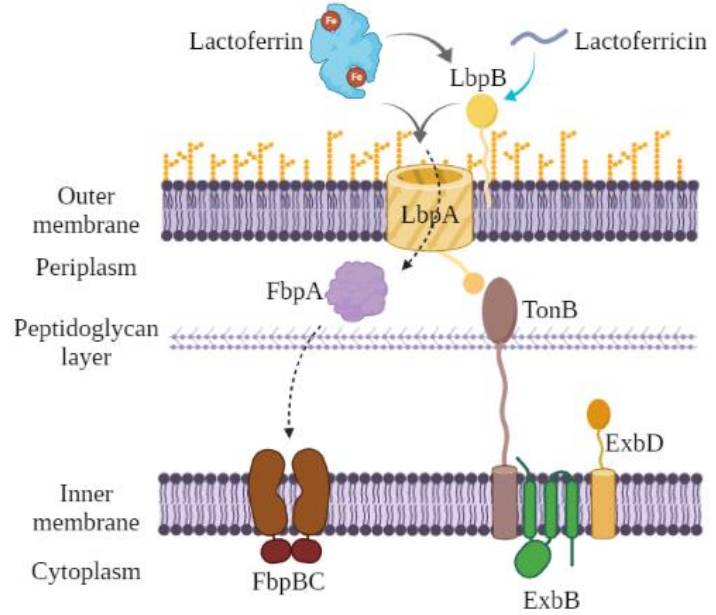


Figure 1.10. The dual functions of LbpB. LbpA and LbpB acquire iron from lactoferrin and transport across the membrane using TonB-ExbB-ExbD system generated proton motive force. Subsequently, iron is transported across the periplasm and inner membrane by FbpA and FbpBC proteins, respectively. In addition, LbpB binds to host cationic antimicrobial peptide lactoferricin and protects the pathogen from its antimicrobial activity. Figure was created using BioRender.

Polyclonal rabbit antiserum against recombinant LbpB was bactericidal and cross-reactive⁸⁶. Furthermore, evaluation of human convalescent sera showed that Nme LbpB is highly immunogenic in humans⁸⁶. Transcriptome analysis of a Nme blood infection showed that genes encoding LbpA and LbpB were upregulated¹⁴⁷. Thus, these results, coupled with the Lbp system being present in all Nme strains, further suggest that lactoferrin binding proteins are important virulence factors in mediating Nme pathogenesis. Understanding the molecular mechanism of the Lbp system will therefore contribute to the development of therapeutic drugs/vaccines against Neisserial pathogens.

1.4.3 Hemoglobin-haptoglobin utilization proteins

In the human body, more than two third of iron is present in red blood cells⁸⁷. Hemoglobin (Hb) is the primary constituent of the red blood cells and responsible for transporting oxygen to different tissues in the body. Hb is an $\alpha_2\beta_2$ tetramer that contains total four heme groups with one

heme molecule bound in hydrophobic pocket of each chain (**Figure 1.11A**)^{148,149}. The heme group is composed of a porphyrin moiety with a ferrous ion. The oxygen binds to iron in the heme group of Hb in an unstable reversible manner¹⁵⁰. In the serum, Hb levels are almost non-existent. However, in the event of hemolysis, Hb is released in the plasma and dissociates into $\alpha\beta$ dimer¹⁵¹. In the plasma, Hb dimer associates with haptoglobin (Hp) and cleared by macrophages^{152,153}. Hp is an acute-phase protein composed serine protease and complement control protein (CCP) domains^{154,155}. The structures of porcine and human hemoglobin-haptoglobin (Hb-Hp) complexes show that serine protease domain of Hp binds to Hb dimer (**Figure 1.11B**)¹⁵⁴⁻¹⁵⁶. The CCP domains of Hp interact through β -strand pairing and disulfide bridge creating a barbell-shape architecture of the Hb-Hp complex¹⁵⁴⁻¹⁵⁶. In the complex, one Hb dimer is bound to each distal end of Hp dimer¹⁵⁴⁻¹⁵⁶.

Neisseria can utilize the Hb-Hp complex as an iron source¹⁵⁷. *Neisseria* encodes for a bipartite receptor, HpuAB, to acquire heme from the host Hb-Hp complex^{81-83,158,159}. In addition to human Hb-Hp, HpuAB can bind to human and non-human Hb for heme acquisition^{160,161}. HpuAB is present in a range of *Neisseria* species. HpuAB is under immune selection and shows high

phase variation among pathogenic *Neisseria*¹⁶²⁻¹⁶⁴. Almost 60% of Nme and 100% of Ngo express HpuAB¹⁶⁴. Along with pathogenic *Neisseria*, commensal *N. polysaccharea*, *N. lactamica*, *N. cinerea*, *N. subflava*, and *N. mucosa* also encode for HpuAB¹⁶⁴. HpuAB is composed of two outer membrane proteins, HpuA and HpuB, and it can bind to Hb, Hb-Hp, and apo-Hp^{81-83,159}. Additionally, HpuA and HpuB are co-transcribed and required for heme acquisition^{82,158,159,165}.

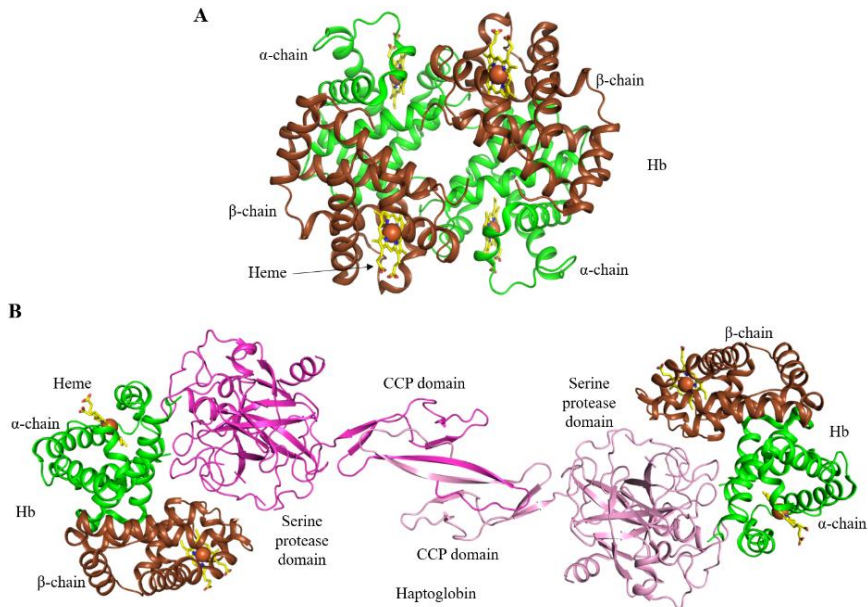


Figure 1.11. The heme binding proteins. (A) Hb is an $\alpha_2\beta_2$ tetramer and contains four heme groups (PDB ID: 5N11¹⁴⁹). (B) Hb-Hp structure shows that serine protease domain of Hp interacts with $\alpha\beta$ dimer of hemoglobin (PDB ID: 4WJG¹⁵⁵). CCP, complement control protein; Hb, hemoglobin.

Hemoglobin-haptoglobin utilization protein A

Hemoglobin-haptoglobin utilization protein A (HpuA) is a lipoprotein anchored to the extracellular leaflet of the outer membrane^{82,159}. HpuA interacts with HpuB and is required for heme extraction from Hb and Hb-Hp^{159,161,162,165}. HpuA is ~35-42 kDa in size, which is around half the size of LbpB and TbpB lipoproteins^{82,159}.

A crystal structure of full-length HpuA from *Kingella denitrificans* (*Kd*HpuA) showed that HpuA is composed of an N-terminal β -sandwich and C-terminal β -barrel with long surface-exposed loops (**Figure 1.12A**)¹⁶⁶. Interestingly, these loops harbor hydrophobic residues at their distal ends. Additionally, a crystal structure of the HpuA C-terminal β -barrel from *Nme* showed high structural similarity to *Kd*HpuA (**Figure 1.12B**)¹⁶⁶. In these structures, the HpuA core is highly conserved, whereas the surface exposed long loops show high degrees of sequence and

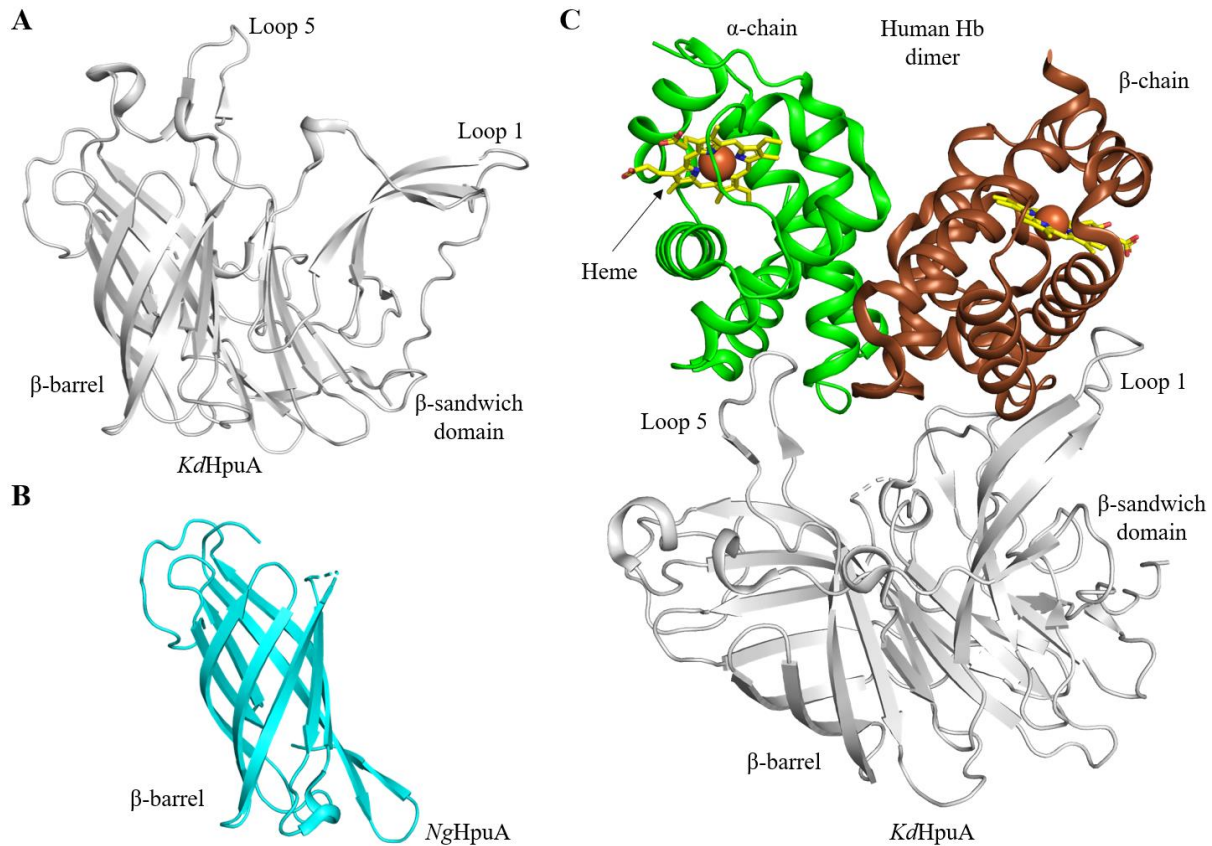


Figure 1.12. The HpuA-Hb crystal structure. (A) *Kd*HpuA structure (PDB ID: 5EC6¹⁶⁶) is composed of an N-terminal β -sandwich and a C-terminal β -barrel domain. These domains contain long surface exposed loops that mediate Hb binding. (B) C-terminal β -barrel domain structure of *Ng*HpuA (PDB ID: 5EE2¹⁶⁶). (C) Structure of *Kd*HpuA in complex with human Hb $\alpha\beta$ dimer (PDB ID: 5EE4¹⁶⁶). Surface-exposed loops of HpuA interact with both chains of Hb. Hb, hemoglobin.

structural variation^{164,166}. The HpuA structure also shows similarities to other lipoproteins present in *Neisseria*, such as TbpB⁴³.

The HpuA protein can bind to Hb and Hb-Hp in the absence of HpuB¹⁶⁶. The crystal structure of *Kd*HpuA in complex with Hb showed that one HpuA molecule interacts with a Hb dimer (**Figure 1.12C**)¹⁶⁶. In the complex structure, surface-exposed loops of HpuA interact with both α - and β -chains of Hb¹⁶⁶. The β -chain of Hb exclusively binds to surface exposed loop-1 of the N-terminus β -sandwich domain of HpuA, whereas the α -chain of Hb forms hydrogen bonds with the C-terminal β -barrel domain of HpuA. Additionally, the above-mentioned hydrophobic residues also participate in the complex formation. The complex formation does not induce any significant conformational change in the Hb structure, whereas the surface-exposed loops of HpuA show movement to accommodate Hb binding. Even though there is no structure of *Ng*HpuA in complex with Hb available, the binding studies of *Ng*HpuA mutants with Hb suggest a similar binding interface¹⁶⁶. In Hb, the HpuA binding site is distinct from the Hp binding site¹⁵⁶. This will allow HpuA to bind to Hb-Hp with the same interface. Interestingly, the heme groups in Hb are located ~20 Å away from the HpuA binding interface and do not participate in binding. Given the essential role of HpuA in heme acquisition, it was hypothesized that HpuA may orient Hb for high affinity binding to HpuB, as well as participate in heme extraction through an unknown mechanism¹⁶⁶.

Hemoglobin-haptoglobin utilization protein B

Hemoglobin-haptoglobin utilization protein B (HpuB) is an outer membrane protein that binds to Hb, apo-Hp, and the Hb-Hp complex^{81,83,165}. Even though HpuAB can bind to both Hb and Hb-Hp, it extracts heme from Hb-Hp more efficiently¹⁶⁵. Flow cytometry studies of *Nme* strains showed that HpuB alone can bind to Hb-Hp, however, it shows higher affinity in the presence of HpuA, suggesting both HpuA and HpuB are required for a functional Hb-Hp receptor¹⁶⁵. Indeed, both HpuA and HpuB interact with each other and are essential for heme acquisition^{159,161,162}.

HpuB is a TonB-dependent transporter and utilizes the PMF generated by the inner membrane Ton complex⁸². Although there are no experimental structures of HpuB available, based on its similarity with other TonB-dependent transporters, a homology model of HpuB was proposed¹⁶⁴. As expected, the HpuB model showed a two-domain architecture composed of a C-

terminal 22-stranded β -barrel domain occluded with an N-terminal plug domain. The model allowed mapping of sequence variation on the structure. The extracellular loops showed highest variation¹⁶⁴. HpuB contains a TonB-box motif for interaction with TonB. The interaction with TonB and PMF are important for heme transport across the membrane. The HpuB in TonB⁻ cells showed higher susceptibility towards trypsin digestion compared to wild-type cells¹⁶¹. Additionally, TonB binding to the receptor modulates the binding and release kinetics of Hb and Hb-Hp ligands¹⁶⁵. Similar observations were made in the presence of the PMF inhibitor carbonylcyanide-*m*-chlorophenylhydrazone (CCCP) in wild-type cells^{161,165}. Based on these studies, it has been postulated that TonB-binding to the receptor causes conformational changes in the receptor structure to allow binding and subsequent release of the ligands^{161,165}. However, further studies are required to probe the conformational dynamics of HpuAB upon TonB and ligand binding.

1.4.4 Hemoglobin receptor

Hb is a tetrameric $\alpha_2\beta_2$ protein that contains four heme groups. Along with HpuAB, *Neisseria* produce another hemoglobin receptor, HmbR, that can acquire heme from Hb¹⁶⁷. In an infant rat model for meningitidis infection, a Nme *hmbR* mutant was attenuated, suggesting an important role of HmbR in mediating Nme virulence¹⁶⁷. However, a Nme MC58 *hmbR* deletion mutant showed similar growth as the wild-type in human whole blood, implying it is not required for disease onset¹⁶⁸. Moreover, the anti-HmbR antibodies were not bactericidal, thereby indicating a non-protective immune response¹⁶⁸.

HmbR

Hemoglobin receptor (HmbR) is a TonB-dependent transporter that binds to Hb and acquires heme¹⁶⁷. Unlike the other iron-import systems described above, HmbR is a single component receptor and does not contain an accessory lipoprotein. HmbR extracts and uptakes heme from Hb, but it cannot utilize heme alone¹⁶⁰. Surprisingly, HmbR expression is regulated by iron levels rather than heme groups¹⁶⁰. Additionally, HmbR is primarily present in Nme and Ngo^{164,169,170}. Almost 88% of Nme isolates contain HmbR, whereas all Ngo strains contain the HmbR pseudogene, which encodes for a non-functional protein¹⁶⁴. In Nme, ~64% of strains

contain both HmbR and HpuAB^{164,171}. Both Hb receptors, HmbR and HpuAB, show a high degree of phase variation through slip-strand mispairing in the poly(G) tracts^{162,171}. Investigations of *hmbR* distribution in Nme disease and carriage isolates showed that 95% isolates were *hmbR*-positive¹⁶⁹. Additionally, 90% of Nme isolates with highest disease to carriage clonal complexes encoded for both HmbR and HpuAB¹⁶³. In 91% of Nme disease isolates, either one or both HmbR and HpuAB were in an ON state of phase-variation¹⁶³.

In the absence of an experimental structure, a topology model of HmbR was created based on its homology with other TonB-dependent transporters¹⁷². *In vitro* binding and growth assays of deletion constructs of HmbR provided insight into heme acquisition¹⁷². The deletions in the extracellular loops L2 and L3 showed reduced Hb binding, whereas mutations in the conserved heme transporter motif that is present in the extracellular loop L7 showed diminished heme uptake without compromising Hb binding¹⁷². Although this study provided insights about HmbR's function, further studies are required to understand the molecular mechanism of heme extraction and transport.

CHAPTER 2. STRUCTURAL BASIS FOR LBPB'S ROLE IN IRON IMPORT IN *NEISSERIA*

2.1 Abstract

Lactoferrin binding protein B (LbpB), a surface-exposed lipoprotein, plays important roles in nutrient acquisition and immune response modulation during *Neisseria* pathogenesis. LbpB binds to host iron-containing lactoferrin and helps in iron piracy through an unknown mechanism. Studies conflict and are inconclusive about the LbpB–lactoferrin complex's stoichiometry and binding interface, and the exact role of LbpB in the iron acquisition process remains elusive. Here, we determined crystal and cryo-electron microscopy (cryo-EM) structures of LbpB from *Nme* (*NmLbpB*) and *Ngo* (*NgLbpB*), respectively, in complex with human lactoferrin. The structures reveal the interaction with lactoferrin is formed by the N-lobe loops of LbpB. The comparison of solution scattering and crystal structure shows a strong correlation showing that the crystal structure agrees with the solution conformation. Point mutations along the lactoferrin binding interface in LbpB show significant reduction in lactoferrin binding. Lactoferrin displays $\sim 12^\circ$ rigid body rotation with respect to the protein-protein binding interface in the *NgLbpB*-lactoferrin structure when compared to the *NmLbpB*-lactoferrin structure. Structural analysis demonstrated that *Neisseria* LbpBs bind to lactoferrin in a conserved manner and trap lactoferrin in an iron-bound closed conformation. Taken together, these results provide insight into LbpB's role in iron acquisition from lactoferrin and lay the foundation for structure-based design of therapeutics targeting the interaction of lactoferrin with LbpB.

2.2 Introduction

Iron is an essential nutrient for survival and pathogenicity of *Neisseria*^{40,62}. *Neisseria* utilizes outer membrane proteins to obtain iron from their host^{73,75}. Outer membrane lactoferrin binding proteins, LbpA and LbpB, bind to human lactoferrin and sequester iron from it at the surface of the bacteria²⁵. *NmLbpB* shows selectivity towards human holo-lactoferrin over apo-lactoferrin, transferrin and bovine lactoferrin^{116,139}. Gonococcal strains with the ability to utilize lactoferrin, but not transferrin, as an iron source were able to infect male urethra⁴⁰. Additionally, gonococcal strains expressing both lactoferrin/transferrin binding proteins displayed a selective

advantage over strains expressing only transferrin binding proteins⁴⁰. Almost 50% clinical isolates of Ngo can utilize lactoferrin as an iron source^{40,133}. LbpB is highly immunogenic and present in all meningococcal strains suggesting its potentially important role in pathogenesis⁸⁶.

LbpB shows high sequence homology to TbpB and is predicted to have two lobes, N- and C-lobe¹³⁷. A crystal structure of the N-lobe of LbpB showed a similar arrangement as the N-lobe of TbpB with a root-mean square deviation (RMSD) of 1.7 Å¹⁴². The N-lobe is composed of a handle domain packed against an eight-stranded β-barrel¹⁴². Although no structure of the C-lobe of LbpB has been reported, it is also predicted to contain a similar domain organization¹³⁷. Previous computational and biophysical studies of LbpB have reported conflicted modes of interaction with lactoferrin^{116,137,139,142}. Despite the LbpB's role in iron acquisition and being a potential candidate for vaccine development, the structural understanding of LbpB is limited. Additionally, the release of LbpB from the Neisserial surface into the host environment by proteolytic autotransporter NalP, had cast some doubt onto LbpB's involvement in iron import¹⁴⁴.

To resolve questions pertaining to LbpB's role in iron import, we determined the three-dimensional structures of LbpB from Nme and Ngo in complex with human lactoferrin revealing the protein-protein interface. Binding studies showed that mutations along the lactoferrin binding interface in LbpB abolish lactoferrin binding. Additionally, the LbpB-lactoferrin complex architecture is highly similar in both Nme and Ngo, thereby suggesting that the interaction between LbpB and lactoferrin across *Neisseria* is well conserved. Altogether, the current study provided insights into the molecular basis for LbpB's role in iron import.

2.3 Methods

2.3.1 Construct design and cloning

A pUC57 plasmid containing the codon-optimized gene for LbpB from Nme strain MC58 was obtained from Bio Basic. The gene fragment encoding residues 20 to 737 was amplified using polymerase chain reaction (PCR) with primers containing restriction sites for NcoI (forward primer: GATATCCATGGGAATTGGCGGCAACTTCGGCG) and XhoI (reverse primer: GTATCCTCGAGTTACTTTTCCACTTCCTGCATG). The PCR reaction products were separated on a 1% agarose gel. The band of interest was cut from the gel and purified. Restriction digestion was performed in NEB Cutsmart buffer at 37°C overnight. The digested gene fragment

was ligated into digested pHIS-Parallel2 vector at room temperature for 8 hours. The ligation reaction was transformed into DH5 α cells and grown overnight on Luria Broth (LB) agar plates containing carbenicillin (100 μ g/mL). The individual colonies were picked and grown in 2XYT medium supplemented with ampicillin (50 μ g/mL) at 37°C overnight. The cultures were harvested, and plasmids were extracted. The presence of the gene of interest was confirmed by DNA sequencing. The resultant expression construct encoded for full-length *NmLbpB* with an N-terminal hexa-histidine tag (MSYYHHHHHHHDYDIPTT) followed by a Tobacco Etch Virus (TEV) protease cleavage site (ENLYFQG).

The *NmLbpB* N-lobe (20-362) and C-lobe (381-737) constructs were amplified from the full-length *NmLbpB*-pHIS-Parallel2 plasmid using PCR and cloned using the same procedure as described above. The final construct contained the N/C-lobe with an N-terminal 6X-His-tag followed by a TEV protease cleavage site.

For *NgLbpB*, the *lbpB* gene fragment encoding residues 20 to 728 was amplified from Ngo FA19 genomic DNA by PCR. The *NgLbpB*-pHIS-Parallel2 expression construct containing *NgLbpB* with an N-terminal 6X-His-tag followed by TEV protease site was created using the same procedure as described for the full-length *NmLbpB*.

The site-directed mutagenesis was performed by PCR using the full-length wild-type *LbpB* as a template and primers containing the desired mutations. The PCR products were digested using the DpnI enzyme at 37°C overnight. Subsequently, 5 μ L of the digestion reaction was transformed into DH5 α cells. The plasmids were extracted from single colony cultures and confirmed by sequencing for the desired mutations.

2.3.2 Protein expression and purification

For protein expression, BL21(DE3) cells were transformed with the *LbpB* constructs and then plated on LB agar plates containing carbenicillin (100 μ g/mL) and grown at 37°C overnight. Single colonies were picked and grown overnight in 5 mL 2XYT cultures supplemented with ampicillin (50 μ g/mL). The cultures were centrifuged at 4,000 rpm for 10 minutes at 4°C. The cell pellets were resuspended in fresh 2XYT medium containing ampicillin (50 μ g/mL). Glycerol stocks were prepared by mixing equal volume of resuspended culture and stock media (60% glycerol + 40% LB + ampicillin) and frozen at -80°C for storage.

For expression, the glycerol stock was streaked onto an LB agar plate and colonies were obtained. These colonies were used to prepare an inoculate culture that was grown at 37°C overnight. This culture was then transferred to 500 mL Terrific Broth (TB) medium supplemented with ampicillin (50 µg/mL) and grown at 37°C with shaking at 180 rpm until the optical density at 600 nm (OD₆₀₀) reached 0.5-0.6. The temperature was reduced to 24°C before induction with 0.4 mM isopropyl β-D-thiogalactopyranoside (IPTG) for 9-12 hours. Cells were harvested by centrifugation at 6,000 rpm for 10 minutes at 4°C and frozen at -80°C until further use.

For protein purification, frozen cell pellets were resuspended in lysis buffer (20 mM Tris, pH 7.5, 140 mM NaCl, 5 mM β-mercaptoethanol (BME), 25 mM imidazole). The resuspended cells were supplemented with DNaseI (10 µg/mL) and 0.5 mM phenylmethylsulfonyl fluoride (PMSF) prior to lysis. The cells were lysed using Emulsiflex C3 high pressure homogenizer (Avestin) by three passes at 18,000 psi. The cell lysate was centrifuged at 18,000 rpm for 30 minutes at 4°C to remove unlysed cells and cellular debris. The supernatant was pooled together and used for further purification steps. An AKTA Pure 25L protein purification system (Cytiva) was used for protein purification. The supernatant was subjected to affinity purification using 5 mL Hi-Trap column containing Ni-NTA resin (Qiagen) pre-equilibrated with lysis buffer. Upon passing of the entire supernatant, the column was washed with 50 mL of lysis buffer followed by protein elution using elution buffer (20 mM Tris, pH 7.5, 140 mM NaCl, 5 mM BME, 250 mM imidazole). To remove the 6X-His-tag, the elution fractions were pooled and subjected to TEV protease digestion while dialyzing against dialysis buffer (20 mM Tris, pH 7.5, 140 mM NaCl, 5 mM BME) at 4°C for overnight. The TEV protease and cleaved 6X-His-tag were removed by passing the digested protein over a Ni-NTA affinity column. The cleaved protein was further purified using either a Sephacryl S-300 HR or Superdex 200 Increase 10/300 GL column (Cytiva) pre-equilibrated with size-exclusion chromatography (SEC) buffer (20 mM Tris, pH 7.5, 140 mM NaCl). The fractions were visualized on a sodium dodecyl sulfate-polyacrylamide gel electrophoresis (SDS-PAGE) gel to identify protein containing fractions, as well as to examine the purity of the sample. The fractions containing the protein were pooled together and concentrated.

Human holo-lactoferrin protein was obtained from RayBiotech, Inc. Prior to use in experiments, lactoferrin was resuspended in SEC buffer and subjected to SEC purification using a Superdex 200 Increase 10/300 GL column (Cytiva). The fractions were assessed by SDS-PAGE and those containing the purest lactoferrin were pooled and concentrated.

2.3.3 Formation of the LbpB-lactoferrin complex

For complex formation, LbpB was incubated with a 2-fold molar excess of holo-lactoferrin at 4°C for 1 hour. Excess lactoferrin was removed by subjecting the incubation mixture to SEC chromatography with a Superdex 200 Increase 10/300 GL column (Cytiva) using SEC buffer. The elution fractions were run on the gel to confirm the complex formation. Fractions containing the LbpB-lactoferrin complex were pooled together and concentrated for further experiments.

2.3.4 Small-angle X-ray scattering (SAXS) data collection and processing

Solution scattering studies were performed using 1X phosphate buffered saline (PBS) (8 mM Na₂HPO₄, 2 mM KH₂PO₄, 137 mM NaCl, 2.7 mM KCl). SAXS studies of the full-length LbpB, lactoferrin, and LbpB-lactoferrin complex were conducted using static and SEC-coupled SAXS (SEC-SAXS) at DuPont-Northwestern-Dow - Collaborative Access Team (DND-CAT) and Biophysics Collaborative Access Team (BioCAT), respectively, at Advanced Photon Source, Argonne National Laboratory, Lemont, Illinois.

For static-SAXS, dilutions of the *Nm*LbpB and *Nm*LbpB-lactoferrin complex were prepared and centrifuged prior to data collection. The samples were loaded into capillaries and scattering data were collected at beamline 5-ID-D of DND-CAT. The data was analyzed using ATSAS¹⁷³ and BioXTAS RAW¹⁷⁴. Buffer scattering curve was subtracted from the protein scattering curves to obtain the protein-only scattering intensities. Particle dispersity and molecular weight were calculated through Guinier analysis. Pair distance distribution function $P(r)$ was calculated using GNOM¹⁷³ to obtain radius of gyration (R_g) and maximum dimension (D_{max}) values.

For SEC-SAXS, the protein was loaded onto the Superdex 200 Increase 10/300 GL column (Cytiva), and data was collected in continuous mode. Raw data was processed using beamline software with subsequent analysis in BioXTAS RAW¹⁷⁴. The buffer subtracted scattering curve was inspected using log-log plot, and if appropriate, further analysis was performed. Guinier fit was performed by selecting the appropriate $q \cdot R_g$ values for globular proteins ($q_{max} R_g < 1.3$) for analyzing the dispersity of the sample. Furthermore, $P(r)$ function was calculated using GNOM¹⁷³ to obtain R_g and D_{max} values. All the figures were prepared using BioXTAS RAW¹⁷⁴. The

theoretical scattering curve from the crystal structure was calculated and fitted with the experimental scattering curve using CRY SOL¹⁷³.

2.3.5 Crystallization, data collection and data processing

For crystallization, the *NmLbpB*-lactoferrin complex was concentrated to 7.4 mg/mL in 20 mM Tris, pH 7.5, 140 mM NaCl buffer. Crystallization screening was performed using commercial crystallization screens. A Mosquito LCP crystallization robot (SPT Labtech) was used to setup hanging-drop vapor diffusion trays with crystallization drops containing equal-volumes (150 nL) of protein and reservoir solution and trays were incubated at 20°C. Initial hits were identified by ultra-violet (UV) imaging of the drop of interest with a PRS-1000 UV-VIS microscope (Korima, Inc.) and optimized using 24-well VDXm trays. Crystals diffracting to sub 4 Å resolution were obtained in 50 mM Tris, pH 8.5, and 2.3 M (NH₄)₂SO₄. These crystals were further optimized using the Dragonfly crystal screen optimization robot (SPT Labtech) to produce well-ordered crystals in 20 mM Tris, pH 8.5, and 2.0 M (NH₄)₂SO₄. Crystals were harvested directly from the trays and flash frozen in liquid nitrogen until screening and data collection.

Crystals were screened and diffraction data were collected at 12.0 keV at the GM/CA 23ID-D beamline at the Advanced Photon Source, Argonne National Laboratory. The diffraction data were processed using HKL2000¹⁷⁵ in P4₃2₁2 space group with unit cell parameters $a = b = 120.39$, $c = 207.38$, $\alpha = \beta = \gamma = 90.0$. The data quality was checked using Xtriage (Phenix)¹⁷⁶. The resolution cutoff of 2.85 Å was determined based on CC_{1/2} value of 0.4 in the highest resolution bin. The data collection and processing parameters are summarized in **Table 2.1**.

2.3.6 Structure determination

Initial phases were obtained by molecular replacement using the Phaser-MR¹⁷⁷ in PHENIX¹⁷⁶. The *NmLbpB* N-lobe (PDB ID: 4U9C¹⁴²) and human holo-lactoferrin (PDB ID: 2BJJ¹²⁴) structures were used as search models. The *NmLbpB* C-lobe was manually built into the electron density through several iterative cycles of model building and refinement using COOT¹⁷⁸ and phenix.refine¹⁷⁹, respectively. In the final rounds of model building, sulphate, and carbonate ions, along with water molecules, were added and refined. The final R_{work} and R_{free} values for the *NmLbpB*-lactoferrin structure were 0.20 and 0.25, respectively. Refinement parameters are

summarized in **Table 2.1**. The protein-protein interface was analyzed using the QtPISA¹⁸⁰ (Protein Interfaces, Surfaces and Assemblies) available in the CCP4 v7.0 suite¹⁸¹. Structure factors and model coordinates have been deposited into the Protein Data Bank with PDB ID 7JRD. PyMOL (Schrodinger) program was used for the structural analysis and figure preparation.

2.3.7 Solid-phase binding assay

For the binding studies, holo-lactoferrin was conjugated with horse radish peroxidase (HRP) enzyme using EZ-LinkTM Plus Activated Peroxidase Kit (Thermo Fisher Scientific) according to the manufacturer's instructions. Briefly, the lactoferrin protein was reconstituted into 1xPBS buffer and purified over a Superdex 200 Increase 10/300 GL column (Cytiva). Fractions containing lactoferrin were pooled and concentrated. For conjugation, 1 mg of lyophilized EZ-Link Plus Activated Peroxidase was reconstituted into 100 μ L of ultrapure water and mixed with 1 mg of lactoferrin protein, followed by the immediate addition of 10 μ L of sodium cyanoborohydride in a fume hood. This conjugation reaction was incubated at room temperature for one hour. The reaction was stopped by the addition of 20 μ L of quenching buffer at room temperature for 15 minutes. Finally, the quenched reaction was loaded over a Superdex 200 Increase 10/300 GL column (Cytiva) for purifying the conjugate through SEC. Fractions containing the lactoferrin-HRP conjugate were pooled, mixed with an equal volume of glycerol, and stored in 100 μ L aliquots at -80°C until further use.

Table 2.1. Data collection, processing, and refinement parameters for the *NmLbpB*-lactoferrin crystal structure. The final model has been deposited into PDB databases with ID 7JRD.

Data Collection	<i>NmLbpB</i> -Lf
λ (Å)	1.0
Space group	P4 ₃ 2 ₁ 2
a, b, c (Å)	120.39, 120.39, 207.38
α , β , γ (°)	90, 90, 90
Resolution (Å)*	50 – 2.85 (2.95 – 2.85)
Completeness (%)*	99.9 (100)
Redundancy*	8.9 (8.7)
R_{sym} †*	0.263 (2.93)
I / σ (I)*	14 (1.33)
CC _{1/2}	0.985 (0.405)
Refinement	
Resolution (Å)	47.62 – 2.85 (2.95 – 2.85)
No. reflections	36134 (3516)
$R^{\S}/R_{\text{free}}^{\P}$	0.20/0.25
R.M.S. deviations	
Bonds (Å)	0.002
Angles (°)	0.57
No. Protein atoms	9459
No. Ligand atoms	75
No. Waters	13
B-factors (Å²)	
Wilson B	77.46
Protein	87.41
Ligands	133.38
Waters	60.17
Ramachandran Analysis[‡]	
Favored (%)	92.58
Allowed (%)	7.18
Outliers (%)	0.24
PDB ID	7JRD

† $R_{\text{sym}} = \sum_{hkl,j} (|I_{hkl} - \langle I_{hkl} \rangle|) / \sum_{hkl,j} I_{hkl}$, where $\langle I_{hkl} \rangle$ is the average intensity for a set of j symmetry related reflections and I_{hkl} is the value of the intensity for a single reflection within a set of symmetry-related reflections.

§ R factor = $\sum_{hkl} (||F_o| - |F_c||) / \sum_{hkl} |F_o|$ where F_o is the observed structure factor amplitude and F_c is the calculated structure factor amplitude.

¶ $R_{\text{free}} = \sum_{hkl,T} (||F_o| - |F_c||) / \sum_{hkl,T} |F_o|$, where a test set, T (5% of the data), is omitted from the refinement.

‡ Performed using Molprobity within PHENIX.

* Indicates statistics for last resolution shell shown in parenthesis.

To assess lactoferrin binding of the *NmLbpB* variants, we used solid-phase binding assays. The *NmLbpB* wild-type and mutants were diluted to a final concentration of 100 $\mu\text{g/mL}$ in 1xPBS buffer. Polyvinylidene difluoride (PVDF) membrane was prepared by dipping it into 100% methanol solution for 30s, followed by washing in 1xPBS buffer for an additional 30s. For the assay, 10 μL of the wild-type and mutant *NmLbpB* were spotted on the activated PVDF membrane and then air dried at room-temperature. PBS buffer, holo-lactoferrin, and the *E. coli* β -barrel

assembly machine (BAM) protein were spotted on the membrane as blank, antibody control and negative control, respectively. The membrane was blocked with 5% bovine serum albumin (BSA) dissolved in PBS for 15 minutes while rocking. Upon blocking, the BSA solution was removed, and the membrane was washed with PBS + 0.005 % Tween 20 (PBST) three times, with a 5-minute incubation for each wash. To allow lactoferrin binding, the membrane was incubated with 20 µg/mL holo-lactoferrin in 0.5% BSA solution for 15 minutes. Excess lactoferrin was removed by three washes with PBST. The membrane was then probed with 1:100,000-fold dilution of horse radish peroxidase (HRP) enzyme conjugated rabbit anti-human lactoferrin antibody (RayBiotech, Inc.) in 0.5% BSA for 15 minutes. The membrane was washed three times with PBST followed by PBS. Finally, the blot was developed with enhanced chemiluminescence (ECL) substrate and imaged using an ImageQuant LAS 4000 imaging system (GE Healthcare/Cytiva). All the solid-phase binding assays were repeated three times.

For studying the lactoferrin binding potential of the wild-type and mutant *NmLbpB*, we performed solid-phase binding assays with similar procedure as outlined above using holo-lactoferrin-HRP. 1xPBS buffer and *Pisum sativum* Toc75 POTRA domain (*PsToc75*) were used as a blank and negative control. All the solid-phase binding assays were repeated three times.

2.3.8 Enzyme-linked immunosorbent assays

Sandwich enzyme-linked immunosorbent assays (ELISA) were performed to screen *NmLbpB* mutants for quantitative assessment of lactoferrin binding. Flat-bottom ELISA plates (Greiner Bio-one International GmbH) were first coated with 100 µL of the *NmLbpB* variants at 100 µg/mL concentration for overnight at 4°C on a rocker. All subsequent steps were performed at room temperature with shaking at 500 rpm. The unbound protein was removed by aspirating the liquid from the well. The wells were washed three times with 200 µL of PBST by incubating for 5 minute each. The wells were blocked with 100 µL of a 5% BSA solution for 30 minutes. The BSA solution was removed, and wells were washed three times with 200 µL of PBST. Then, 100 µL of 20 µg/mL holo-lactoferrin in 0.5% BSA solution was incubated in the wells for 30 minutes and then washed three times with PBST. The wells were then probed using 100 µL of 1:100,000-fold diluted HRP-conjugated rabbit anti-lactoferrin antibody (RayBiotech, Inc.) in 0.5% BSA for 30 minutes followed by washes with PBST and PBS. The assay was then developed with 100 µL of 1-Step Ultra TMB-ELISA substrate solution (Thermo Scientific). The HRP enzymatic reaction

was stopped using 100 μ L stop solution (0.18 M H_2SO_4). The absorbance at 450 nm was measured using a Spectramax M2e microplate reader (Molecular devices) without mixing. The data were further analyzed using Microsoft Excel, including data averaging, standard error calculations, and data visualization. All the experiments were performed in either duplicate or triplicate and repeated four times.

For NgLbpB wild-type and mutants, we performed lactoferrin binding studies using a direct ELISA. The assay was performed using similar procedure as outlined above using holo-lactoferrin-HRP. 1xPBS buffer and *Pisum sativum* Toc75 POTRA domain (*PsToc75*) were used as a blank and negative control. The ELISA assays were performed in either triplicates or quadruplets for a total of three repeats.

2.3.9 Isothermal titration calorimetry

To obtain the dissociation constant (K_d) of lactoferrin binding to the *NmLbpB* variants, isothermal titration calorimetry (ITC) experiments were performed using MicroCal iTC200 calorimeter (Malvern Panalytical) by Dr. Courtney Daczkowski in collaboration with Prof. Andrew Mesecar's lab at Purdue University. *NmLbpB* variants and lactoferrin proteins were purified in PBS buffer and concentrated to 30 μ M and 300 μ M concentration, respectively. For the titrations, the sample cell contained the *NmLbpB* variants while lactoferrin was injected from the syringe while stirring at 25°C. The heat released during the injections was recorded and analyzed using Origin 7.0 (OriginLab). The K_d , n-value, and other thermodynamic parameters were calculated by fitting the experimental data with single binding site model.

2.3.10 Sample preparation and data collection for cryo-EM

Quantifoil R 3.5/1 Cu 200 grids were glow-discharged at 0.26 mBar pressure and 25 mA current for 1 minute with 10 s hold using PELCO easiGlow™ Glow Discharge Cleaning System (TED PELLA, INC.) prior to use. For vitrification, 2.5 μ L sample at 0.125 mg/mL was applied to the grid and incubated for 30 s at 100% humidity and 4°C. The grid was blotted for 2 s with a blot force of 2 and plunge frozen into liquid ethane using a Vitrobot Mark IV (Thermo Fisher Scientific). Grids were stored in liquid nitrogen until screening and data collection.

Grid screening and cryo-EM data collection were performed on a Titan Krios G1 microscope (Thermo Fisher Scientific) operated at 300 kV equipped with a Gatan Quantum energy filter (energy width 20 eV) and a Gatan K3 direct electron detector. Grids were loaded onto microscope using an autoloader and screened for optimal ice-thickness and particle distribution. Grid displaying the best particle distribution and ice-thickness was used for data collection. The cryo-EM data was collected in super-resolution mode at 81,000X magnification with a defocus range of -1 to -2.5 μm and a pixel size 0.54 Å. Each recorded movie was exposed for 3,120 ms with a total dose of 53.68 $\text{e}^-/\text{\AA}^2$ over 40 frames. A single dataset with 4966 movies in total was collected using Leginon¹⁸². Data quality was assessed in real time using cryoSPARC Live¹⁸³. Data collection parameters are summarized in **Table 2.2**.

2.3.11 Cryo-EM data processing and model building

The raw movie frames were aligned, dose weighted, and motion corrected using MotionCor2¹⁸⁴ implemented in Appion¹⁸⁵ with 2x binning to 1.08 Å per pixel. All the subsequent processing was performed in cryoSPARC v3.0.1¹⁸³. The aligned and motion corrected movies were imported into cryoSPARC, and contrast transfer function (CTF) parameters were estimated using ‘Patch CTF-estimation (multi)’. Initially, particles were picked using ‘Blob picker’ on 150 micrograph sub-dataset, extracted with 256-pixel box size, and subjected to ‘2D Classification’.

Table 2.2. Cryo-EM data collection, processing, refinement, and validation statistics for the NgLbpB-lactoferrin complex. The final map and model have been deposited into EMDB and PDB databases with ID EMD-24233 and 7N88, respectively.

Data Collection and Processing		<i>NgLbpB-hLf</i>
Magnification		81,000
Voltage (kV)		300
Electron exposure (e ⁻ /Å ²)		53.68
Defocus range (μm)		-1 to -2.5
Pixel size (Å)		0.54
Symmetry imposed		C1
Initial particle projections (no.)		3,330,059
Final particle projections (no.)		127,832
Map resolution (Å)		3.65
FSC threshold		0.143
Refinement		
Model Resolution (Å)		3.8
FSC threshold		0.5
Map-model CC		
CC_mask		0.72
CC_box		0.74
CC_peaks		0.67
CC_volume		0.72
Model Composition		
Non-hydrogen atoms		9403
Protein residues		1220
Ligands		4
B factors (Å ²)		
Protein		44.75
Ligand		14.75
R.M.S. deviations		
Bond lengths (Å)		0.008
Bond angles (°)		1.020
Validation		
MolProbity Score		2.70
Clashscore		28.36
Poor rotamer (%)		0.81
Ramachandran Plot		
Favored (%)		78.31
Allowed (%)		21.44
Disallowed (%)		0.25
EMDB ID		EMD-24233
PDB ID		7N88

2D classes showing protein-like features were selected and used as templates for particle picking using ‘Template picker’ over the entire dataset with a particle diameter of 256 Å. A total of 3,330,059 particles were extracted and subjected to three rounds of iterative 2D classification to remove the junk particles. After the third round of 2D classification, the best classes were selected, resulting in 1,125,272 particles. These particles were used for generating 10 ab-initio classes using ‘Ab-initio Reconstruction’ followed by ‘Heterogenous Refinement’ with C1 symmetry. The output volumes from the refinement job were visualized using Chimera¹⁸⁶. From heterogenous

refinement, 2 classes containing 279,601 particles in total were selected and further subjected to a second round of ‘Ab-initio Reconstruction,’ generating 3 classes. These classes underwent ‘Heterogenous Refinement’ for redistributing the particles in the appropriate class. The best class with 127,832 particles was further refined using ‘Non-uniform Refinement’ with C1 symmetry¹⁸⁷. Gold-standard Fourier Shell Correlation (GSFSC) curve with 0.143 threshold as the cut-off criteria was used to estimate the resolution of the final reconstruction to 3.65 Å. ‘Local Resolution Estimation’ in cryoSPARC was used for calculating the local resolution.

The sharpened map from Non-uniform Refinement was used for subsequent model building. The map displayed good secondary structure features and side-chain density for the identification of proteins and domains. The final map contained well resolved density for full-length lactoferrin and the N-lobe of *NgLbpB*, but not for the C-lobe of *NgLbpB*. For model building, a homology model of full-length *NgLbpB* was created based on the *NmLbpB* crystal structure (PDB ID: 7JRD¹⁸⁸) and divided into the N-lobe and the C-lobe as guided by the *NmLbpB* structure. The N-lobe of the *NgLbpB* and lactoferrin crystal structure (PDB id: 2BJJ¹²⁴) were docked into the map using ChimeraX¹⁸⁹. The model was refined in real space using Phenix.real_space_refine¹⁹⁰. Finally, the C-lobe of *NgLbpB* was placed as a rigid body, based on the *NmLbpB* full-length structure. Additional model refinement and validation parameters are listed in **Table 2.2**.

QtPISA¹⁸⁰ (Protein Interfaces, Surfaces and Assemblies) was used for analyzing the *NgLbpB* and lactoferrin protein-protein interface. Structural analysis and comparisons were performed using PyMOL. ChimeraX¹⁸⁹ and PyMOL were used for figure preparation. The cryo-EM map and model coordinates have been deposited in the Electron Microscopy Data Bank (EMDB) and Protein Data Bank (PDB) with IDs EMD-24233 and 7N88, respectively.

2.4 Results

2.4.1 Protein production

Lactoferrin binding proteins, LbpA and LbpB, are Neisserial outer membrane proteins that are important for sequestering iron from human lactoferrin. To investigate the role of LbpB in iron acquisition, we recombinantly expressed and purified lipid-anchor truncated *NmLbpB* (20-737) and *NgLbpB* (20-728) (**Figure 2.1A, B and C**). The recombinant LbpBs bind to lactoferrin as assessed by solid-phase binding assay (**Figure 2.1D**). The purified proteins were used for further structural and functional studies.

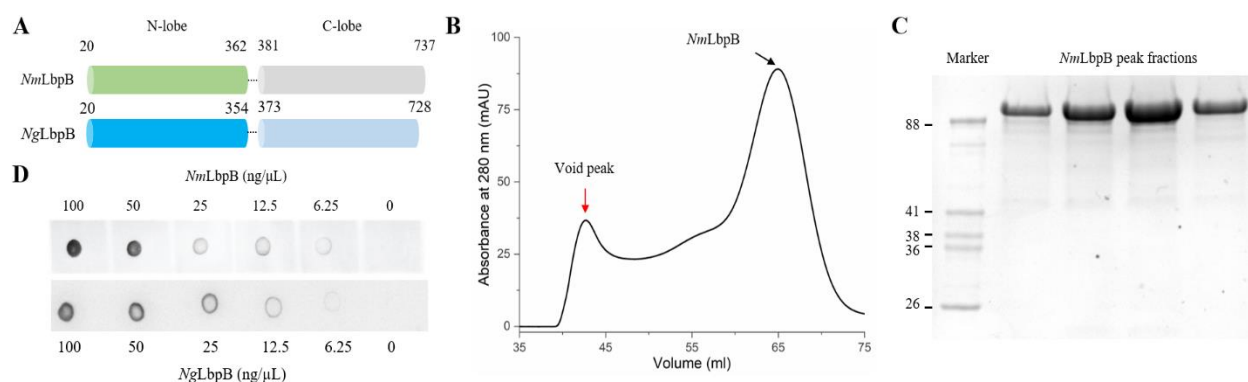


Figure 2.1. Recombinant LbpBs from Nme and Ngo bind to lactoferrin. (A) *NmLbpB* and *NgLbpB* construct used in the current study. (B) Purification of recombinant *NmLbpB* using size-exclusion chromatography. The red and black arrows represent void and *NmLbpB* elution peaks, respectively. (C) Sodium dodecyl sulphate-polyacrylamide gel electrophoresis (SDS-PAGE) analysis of *NmLbpB* elution peak. The *NgLbpB* was purified using similar procedure. (D) Solid-phase binding assays of holo-lactoferrin binding to recombinantly purified LbpB.

2.4.2 SEC-SAXS characterization of *NmLbpB*

We studied the solution structure of *NmLbpB* using static SAXS. The *NmLbpB* dilution series, 3.41 mg/mL, 1.7 mg/mL, and 0.85 mg/mL were created, and the scattering data were collected at DND-CAT. The log-log scattering plot of *NmLbpB* depicted the non-perpendicular intersection of scattering curve with y-axis, which suggested a potential instability of the sample (**Figure 2.2A**). This observation was further supported by Guinier analysis which showed an upward curvature, suggesting polydispersity of *NmLbpB* solution (**Figure 2.2A inset**).

Furthermore, we performed SEC-SAXS studies of *NmLbpB*. The scattering data was analyzed by calculating Guinier plot and $P(r)$ to obtain R_g , molecular weight, and D_{max} information. Unlike static-SAXS, SEC-SAXS Guinier plot showed straight line at low q , suggesting a

monodisperse solution (**Figure 2.2B**). The molecular weight estimations were consistent with

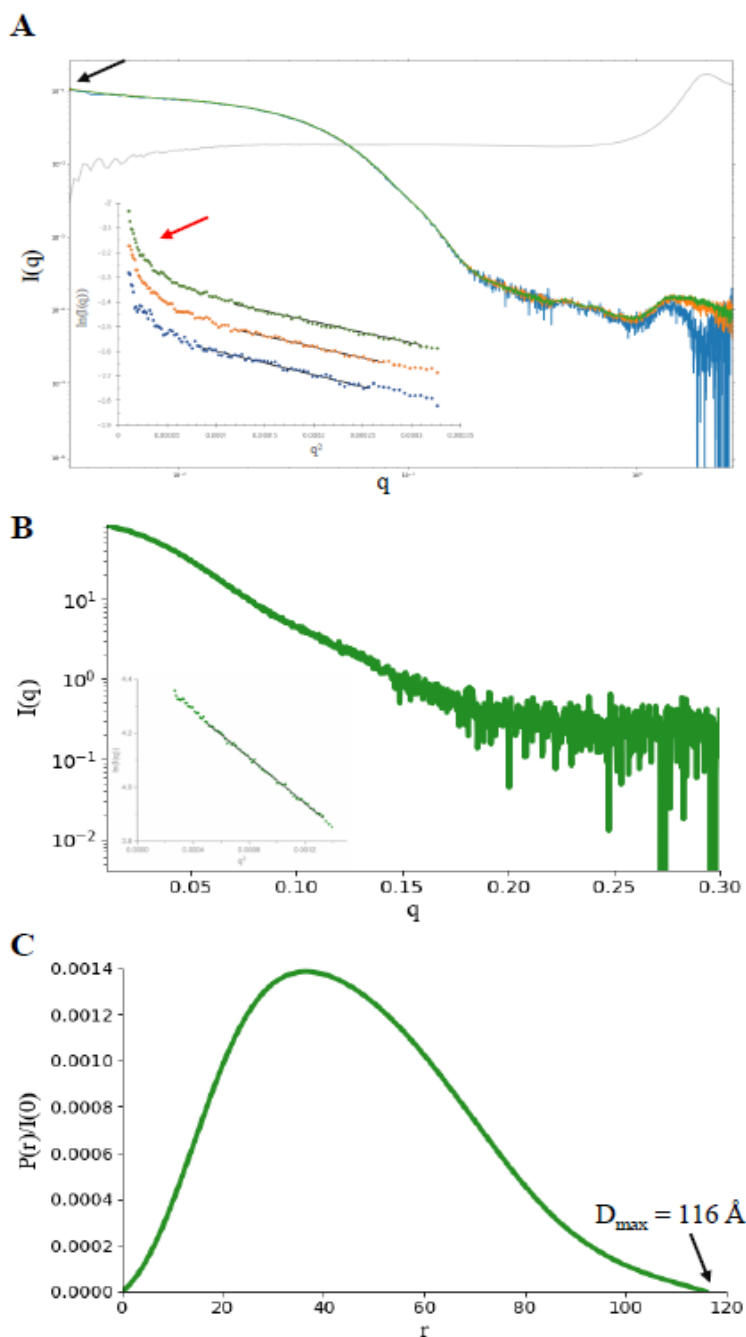


Figure 2.2. SAXS characterization of *NmLbpB*. (A) Static-SAXS plots (log-log) of *NmLbpB* at three different concentrations, 3.41 mg/mL [green], 1.7 mg/mL [orange] and 0.85 mg/mL [blue]. The blank is shown in grey. The black arrow points to non-perpendicular intersection of the curve with y-axis suggesting unstable sample. The inset shows Guinier plots for the SAXS curves. The plots have been offset for clarity. The red arrow points to upward curve at low q suggesting aggregation. SEC-SAXS scattering profile of *NmLbpB* (B) and associated Guinier plot (inset), and $P(r)$ function (C).

NmLbpB being a monomer in solution (**Table 2.3**). For *NmLbpB*, the R_g and D_{\max} values were

$35.9 \pm 0.1 \text{ \AA}$ and 116 \AA , respectively (**Figure 2.2C**). Collectively, the SAXS studies indicated that *NmLbpB* is a monomer in solution.

Table 2.3 Summary of SEC-SAXS parameters. Lactoferrin has a calculated molecular weight (MW) of 76.3 kDa and *NmLbpB* 79.5 kDa.

	Lactoferrin	<i>NmLbpB</i>	<i>NmLbpB</i> -lactoferrin
$R_g \text{ (\AA)}$	33.2 ± 0.3	35.9 ± 0.1	44.6 ± 0.2
$V_c \text{ MW (kDa)}$	75.8	88.9	155.3
$V_p \text{ MW (kDa)}$	88.1	104.6	178.8
Bayes MW (kDa)	80.8	94.2	157.1
Shape/Size MW (kDa)	81.4	98.3	150.0
$D_{max} \text{ (\AA)}$	110	116	134

2.4.3 *NmLbpB* forms a stable complex with lactoferrin

To form the *NmLbpB*-lactoferrin complex, we incubated *NmLbpB* with a 2-molar excess of lactoferrin at 4°C and ran the sample on SEC. Comparison of the incubated sample's SEC chromatogram with *NmLbpB* and lactoferrin alone showed a left-shift of the peak, indicating

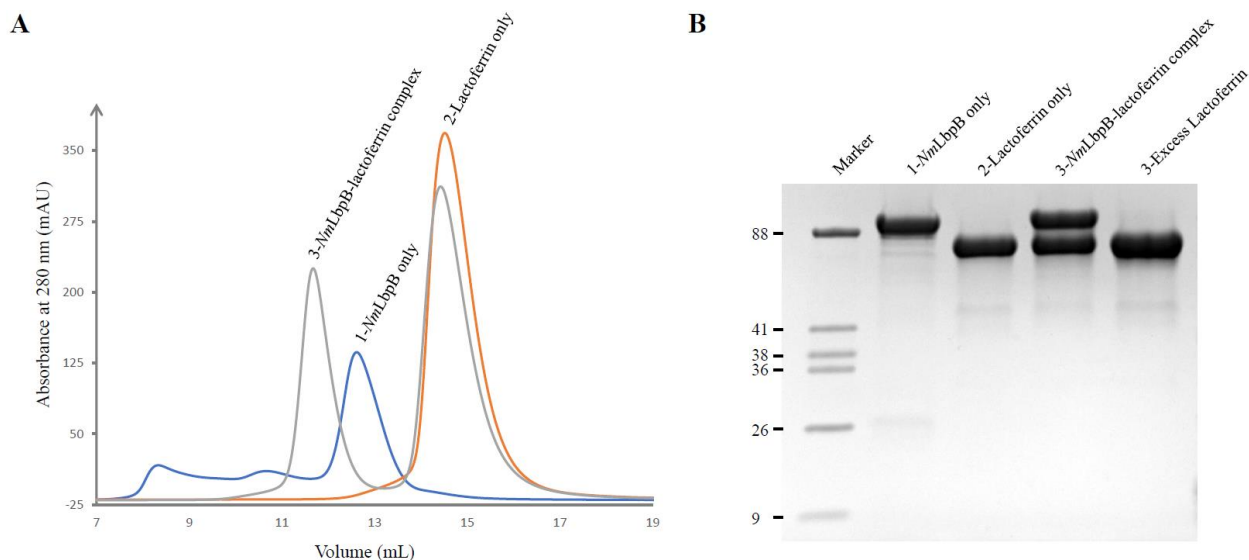


Figure 2.3. Formation of the *NmLbpB*-lactoferrin complex. (A) Size-exclusion chromatography (SEC) chromatographs of *NmLbpB* only, lactoferrin only and *NmLbpB*-lactoferrin complex. A left shift of the complex peak compared to individual components indicates complex formation. (B) Sodium dodecyl sulphate-polyacrylamide gel electrophoresis (SDS-PAGE) analysis of elution peaks from A depicts complex formation associated with peak 3 (lane 4).

complex formation (**Figure 2.3A**). An excess peak corresponding to lactoferrin was also observed.

The SDS-PAGE analysis of the peak fractions confirmed the presence of both *NmLbpB* and lactoferrin proteins in the left-shifted peak fractions (**Figure 2.3B**).

Like *NmLbpB*, we studied the solution structure of *NmLbpB*-lactoferrin complex using static-SAXS. The scattering data was collected with the concentrations 0.59 mg/mL, 1.19 mg/mL, and 2.38 mg/mL at DND-CAT. The log-log scattering plots of *NmLbpB*-lactoferrin complex showed that the plot intersects with the y-axis perpendicularly, thereby suggesting a stable sample (**Figure 2.4A**). The Guinier plot analysis shows a linear curve at low q , consistent with a monodisperse sample (**Figure 2.4A inset**). For the *NmLbpB*-lactoferrin, the calculated molecular weight 157.89 ± 15.79 kDa. These estimates are consistent with a 1:1 stoichiometric complex (calculated molecular weight 155.8 kDa) between *NmLbpB* and lactoferrin with an R_g value of 46.5 Å.

Additionally, the *NmLbpB*-lactoferrin complex was studied

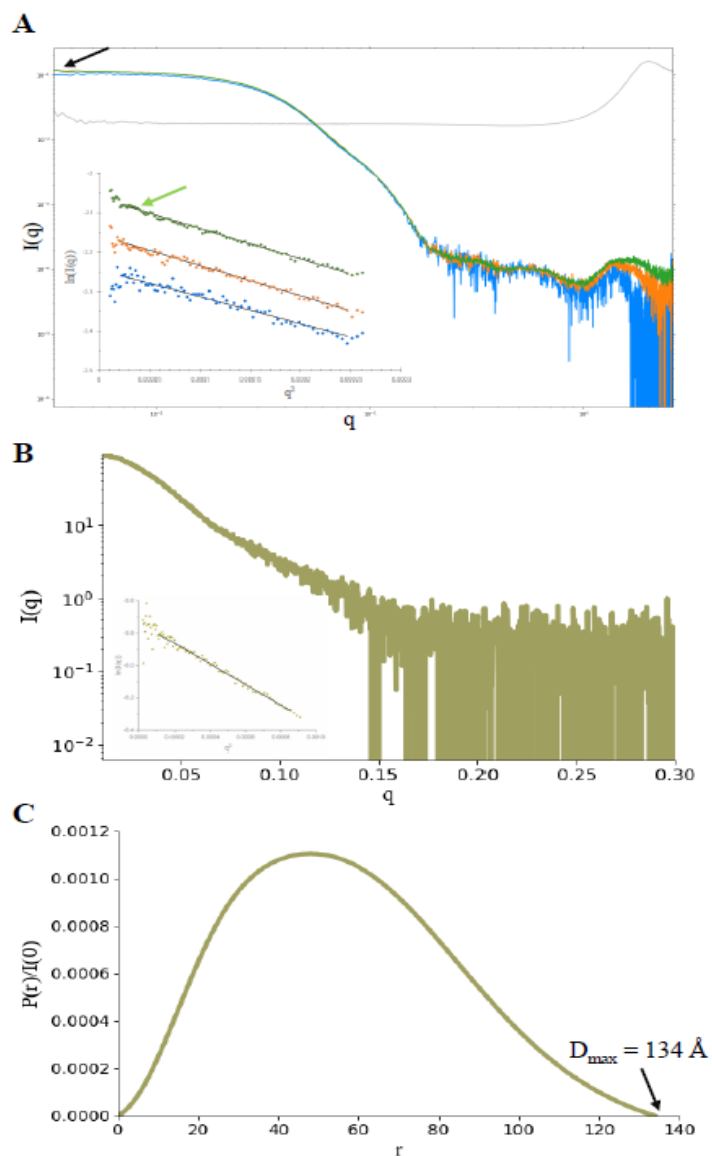


Figure 2.4. SAXS characterization of the *NmLbpB*-lactoferrin complex. (A) Static-SAXS plots (log-log) of *NmLbpB*-lactoferrin complex at three different concentrations, 0.59 mg/mL [blue], 1.19 mg/mL [orange], and 2.38 mg/mL [green]. The blank is shown in grey. The black arrow points to perpendicular intersection of the curve with y-axis suggesting a stable sample. The inset shows Guinier plots for the SAXS curves. The plots have been offset for clarity. The green arrow points to linear plot at low q suggesting stable monodisperse sample. SEC-SAXS scattering profile of *NmLbpB*-lactoferrin complex (B) and associated Guinier plot (inset), and $P(r)$ function (C). Both Static and SEC-SAXS data show similar results suggesting that *NmLbpB* forms a stable complex with lactoferrin.

using SEC-SAXS, which showed similar results as static SAXS (**Figure 2.4B**). The molecular weight values are summarized in the **Table 2.3** and are consistent with a 1:1 stoichiometric *NmLbpB*-lactoferrin complex. The R_g and D_{max} values for the *NmLbpB*-lactoferrin complex were 44.6 ± 0.2 Å and 134 Å, respectively (**Figure 2.4C**). Overall, both static and SEC-SAXS studies indicate that *NmLbpB*-lactoferrin is a stable monodisperse complex in solution with a 1:1 stoichiometry.

2.4.4 SEC-SAXS characterization of *NgLbpB* and *NgLbpB*-lactoferrin complex

The *NgLbpB*-lactoferrin complex was purified using SEC and evaluated for complex formation by SDS-PAGE analysis which revealed presence of both *NgLbpB* and lactoferrin at ~1:1 ratio (**Figure 2.5**). For solution characterization of *NgLbpB* and the *NgLbpB*-lactoferrin complex, we performed SEC-SAXS studies (**Figure 2.6**). The *NgLbpB* scattering analysis through

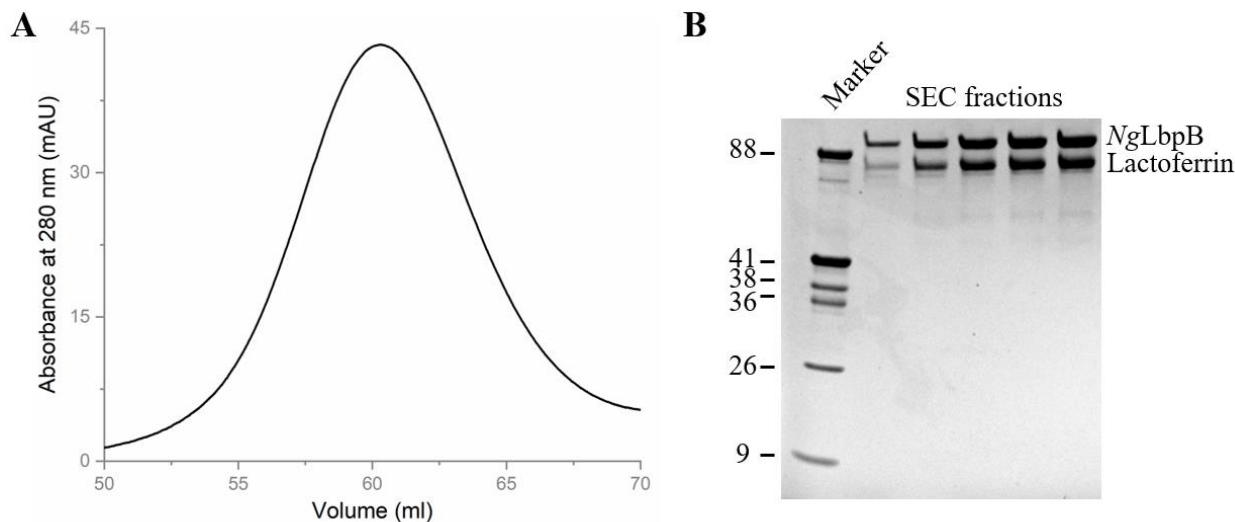


Figure 2.5. Formation of the *NgLbpB*-lactoferrin complex. (A) Purification of *NgLbpB*-lactoferrin complex using SEC. (C) SDS-PAGE analysis of *NmLbpB*-lactoferrin elution peak from panel C shows complex formation.

a Guinier plot suggested that it is a globular protein with a volume of correlation (V_c) molecular weight of 88.8 kDa, and therefore represents a monomer (calculated molecular weight 78.4 kDa) in solution. Pair-distance distribution function $P(r)$ through GNOM¹⁷³ revealed a radius of gyration (R_g) of 37.8 ± 0.1 Å with a maximum dimension D_{max} of 114 Å (**Figure 2.6A**). The *NgLbpB*-lactoferrin complex scattering analysis suggested a 1:1 complex formation through a V_c molecular weight of 168 kDa (calculated molecular weight $78.4 + 76.3 = 154.7$ kDa). The complex R_g and

D_{\max} values of 45.9 ± 0.1 Å and 139 Å, respectively, are also consistent with a 1:1 stoichiometry (Figure 2.6B).

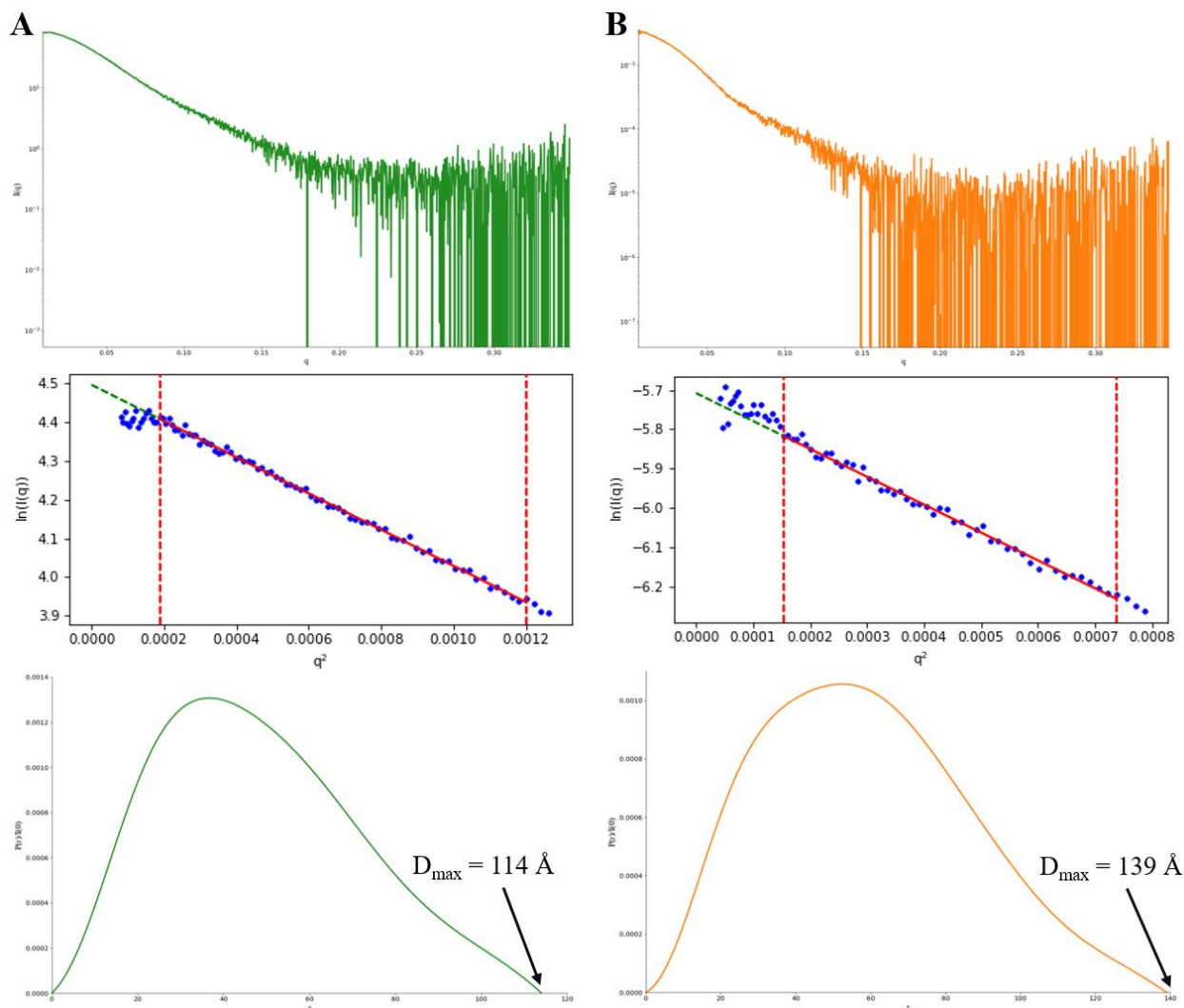


Figure 2.6. SEC-SAXS characterization of *NgLbpB* alone and in complex with lactoferrin. SEC-SAXS scattering profile (top panel) and associated Guinier plot (middle panel) and pair-distance distribution function $P(r)$ (bottom panel) of *NgLbpB* alone (A) and in complex with lactoferrin (B). The black arrow points to D_{\max} in the $P(r)$ function. The SEC-SAXS showed that *NgLbpB* is a monomer in solution and forms 1:1 complex with lactoferrin.

2.4.5 The N-lobe of *NmLbpB* binds to lactoferrin

LbpB is composed of two lobes, termed the N-lobe and the C-lobe. Previously, the LbpB N-lobe crystal structure has been reported, however, no structure of LbpB with lactoferrin has been determined. In absence of a structure, various modes of LbpB and lactoferrin interactions have

been proposed without a consensus. To identify the lobe responsible for lactoferrin binding, we cloned, expressed, and purified individual lobes of *NmLbpB* and assessed their lactoferrin binding potential using a solid-phase binding assay. **Figure 2.7** shows a representative result of the assay, showing that full-length, as well as the N-lobe of *NmLbpB*, bind to

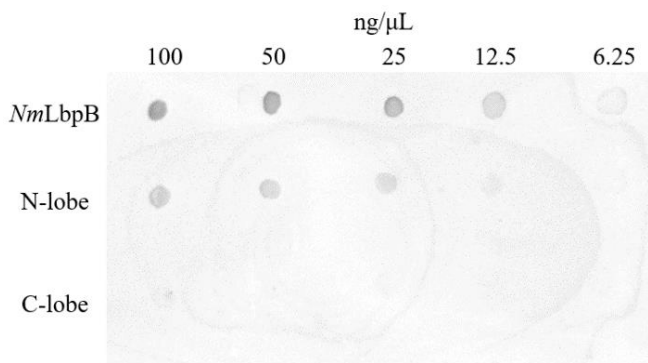


Figure 2.7. Solid-phase binding assay to assess lactoferrin binding to *NmLbpB* constructs. The lactoferrin binds to full-length and N-lobe *NmLbpB*, but not C-lobe only.

lactoferrin, whereas no binding was observed for the C-lobe of *NmLbpB*. This observation suggests that the N-lobe of *NmLbpB* recognizes lactoferrin at the outer membrane during iron acquisition.

2.4.6 The X-ray crystal structure of the *NmLbpB*-lactoferrin complex

Our SAXS studies suggested that the apo *NmLbpB* was prone to aggregation, whereas the *NmLbpB*-lactoferrin complex was stable and monodisperse in solution. Based on this observation, we focused our crystallization efforts to obtain diffraction quality crystals of the *NmLbpB*-lactoferrin complex. Using hanging-drop vapor diffusion, we obtained crystals of the *NmLbpB*-lactoferrin complex, which diffracted to 2.85 Å resolution. The solvent content and Matthew's coefficient calculation suggested the presence of one complex molecule in the asymmetric unit. The initial phases were obtained using molecular replacement in P4₃2₁2 space group. The model was built and refined iteratively to final $R_{\text{work}}/R_{\text{free}}$ values of 0.20/0.25. Ramachandran analysis using MolProbity showed that 92.58% and 7.18% residues were in favored and allowed regions, respectively, whereas only 0.24% were outliers. The data collection, processing, and refinement statistics are listed in **Table 2.1**. In our crystal structure, we observed a 1:1 arrangement of *NmLbpB* and lactoferrin in the asymmetric unit (**Figure 2.8A**). In our crystal structure, the residues 1-4 of lactoferrin and residues 1-33, 344-351, 372-378, 451-528, 628-631, and 679-697 of *NmLbpB* were not modelled in the final model due to absence of clear electron density. The final structure contains 1252 residues, including 564 from *NmLbpB* and 688 from lactoferrin.

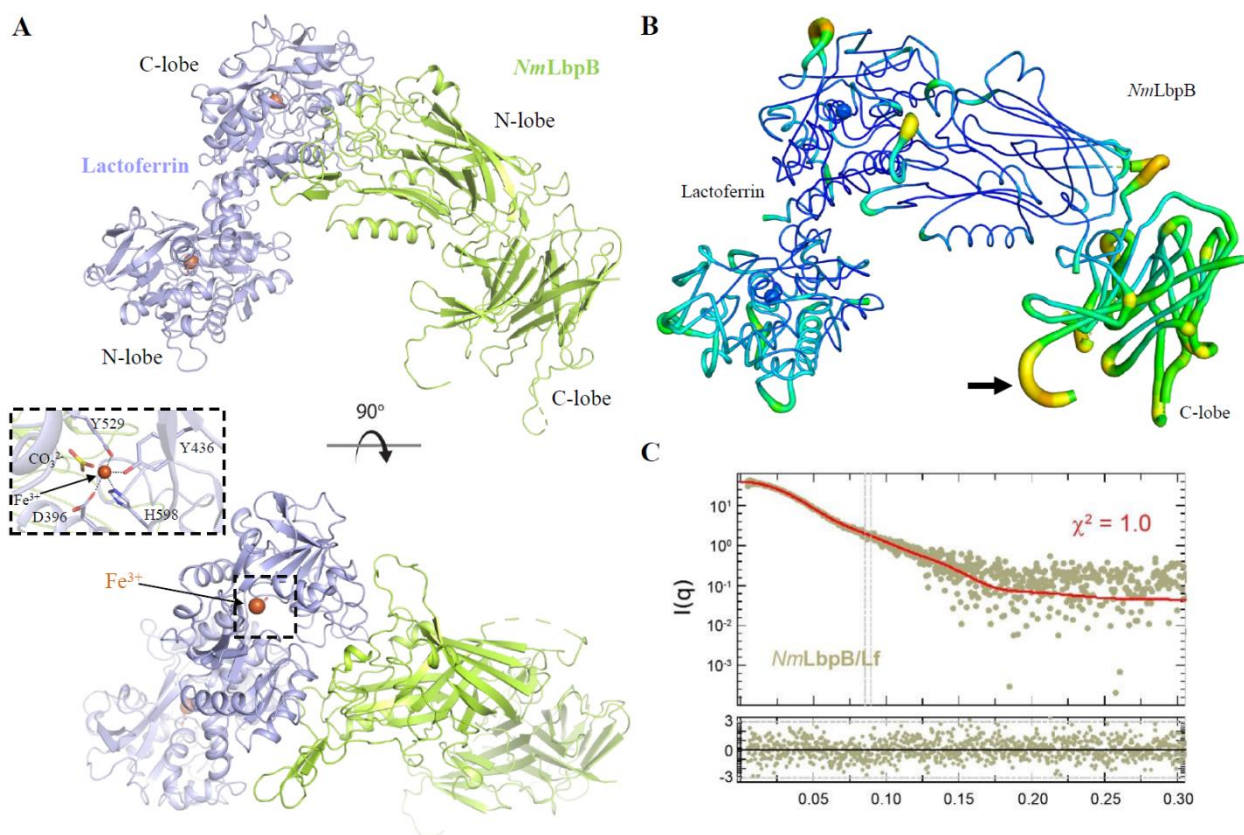


Figure 2.8. The crystal structure of NmLbpB-lactoferrin complex. (A) Orthogonal views of NmLbpB-lactoferrin complex crystal structure with NmLbpB in green, lactoferrin in light blue, iron as brown sphere, and carbonate as yellow stick. The inset shows iron coordination in C-lobe of lactoferrin near the LbpB binding interface. (B) NmLbpB-lactoferrin crystal structure colored based on B-factor. Yellow color represents high whereas blue represents low B-factor. The C-lobe of NmLbpB has higher B-factor suggesting higher flexibility relative to rest of the molecule. The black arrow indicates the disordered anionic loops. (C) Comparison of calculated scattering curve of NmLbpB-lactoferrin structure (red line) with the experimental scattering profile (olive). The top panel display the fit of the data and bottom panel shows the residual. The comparison suggests that crystal structure is in-agreement with ‘in-solution’ structure.

2.4.7 The cryo-EM structure of the NgLbpB-lactoferrin complex

Our initial efforts to obtain the NgLbpB-lactoferrin complex structure were focused on using X-ray crystallography, however, well-ordered crystals could not be obtained. Subsequently, we used cryo-EM for structure determination of the complex. A dataset containing 4,966 movies was collected and image processing performed using cryoSPARC¹⁸³ (Figure 2.9). The 2D classification showed several classes with defined asymmetric protein-like features. These classes contained blurred regions at the end of the molecule, which suggested an intrinsic flexibility of the molecule (Figure 2.9, red arrow). Given the asymmetric nature of the complex, C1 symmetry was used for subsequent reconstruction and refinement steps. After 3 rounds of 2D classification

and 2 rounds of *ab-initio* reconstruction that was followed by heterogeneous refinement, a single class was selected and refined to obtain the final cryo-EM map for the NgLbpB-lactoferrin complex at 3.65 Å resolution (**Figure 2.10**). Similar to the NmLbpB-lactoferrin complex, the NgLbpB-lactoferrin complex also shows a 1:1 stoichiometry between NgLbpB and lactoferrin. In the current structure, we modelled residues 42-338 of NgLbpB in the cryo-EM map. In absence of clear

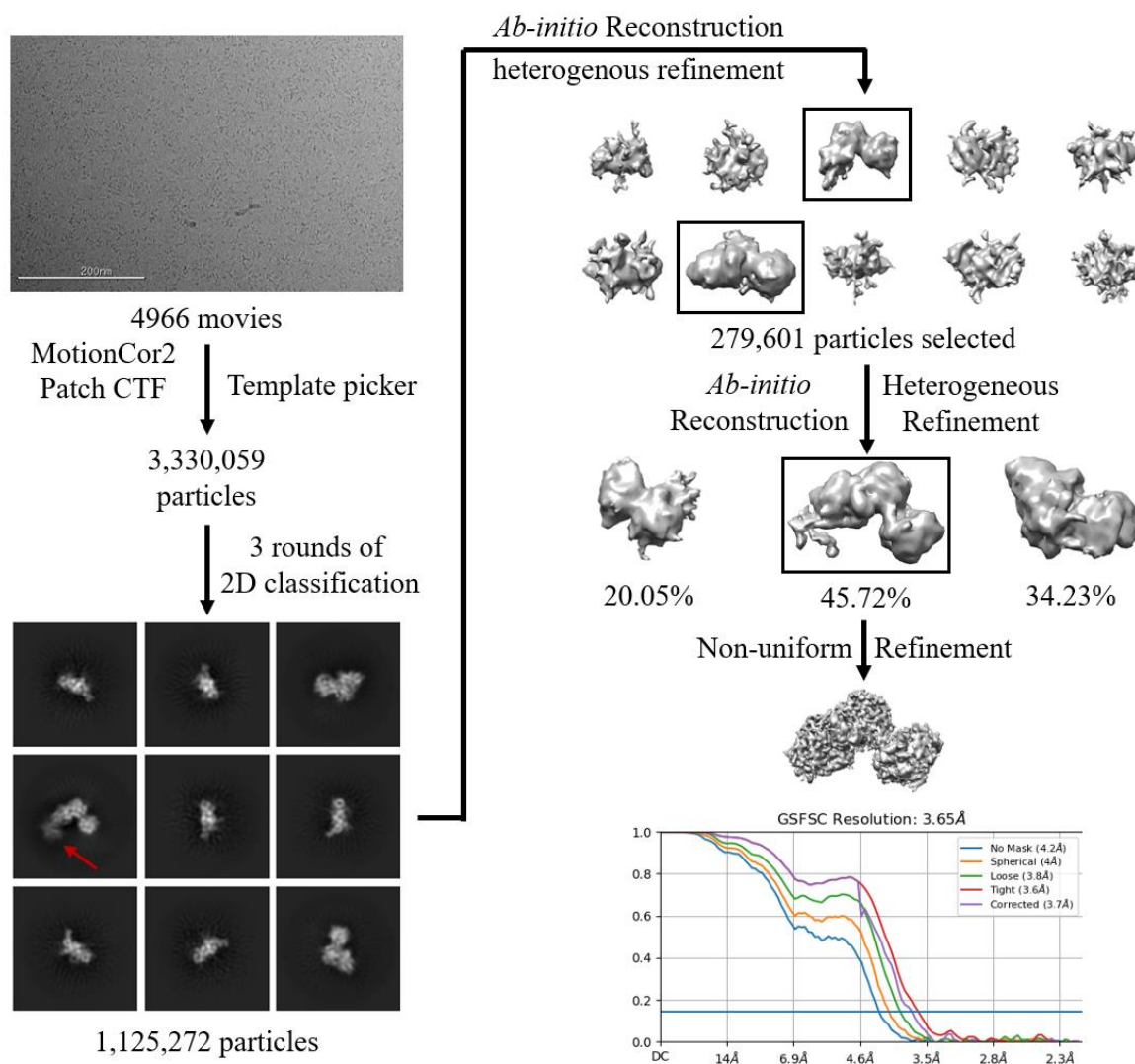


Figure 2.9. Cryo-EM data processing workflow for NgLbpB-lactoferrin complex. Representative cryo-EM micrograph from 4966 movies. Beam induced motion was corrected and contrast transfer function (CTF) parameters were calculated. Particle were picked, extracted, and classified into 2D classes. Representative 2D class averages show different orientations of the particles. The red arrow indicates the blurred region. The selected particles were filtered through two rounds of *ab-initio* reconstructions followed by heterogeneous refinement. Boxed classes were selected for further processing. Finally, a class containing 127,832 particles was subjected to non-uniform refinement to obtain final 3D reconstruction map at 3.65 Å. Gold-standard Fourier shell correlation (GSFSC) curve of NgLbpB-lactoferrin map with the horizontal blue line indicating 0.143 cutoff for resolution estimation.

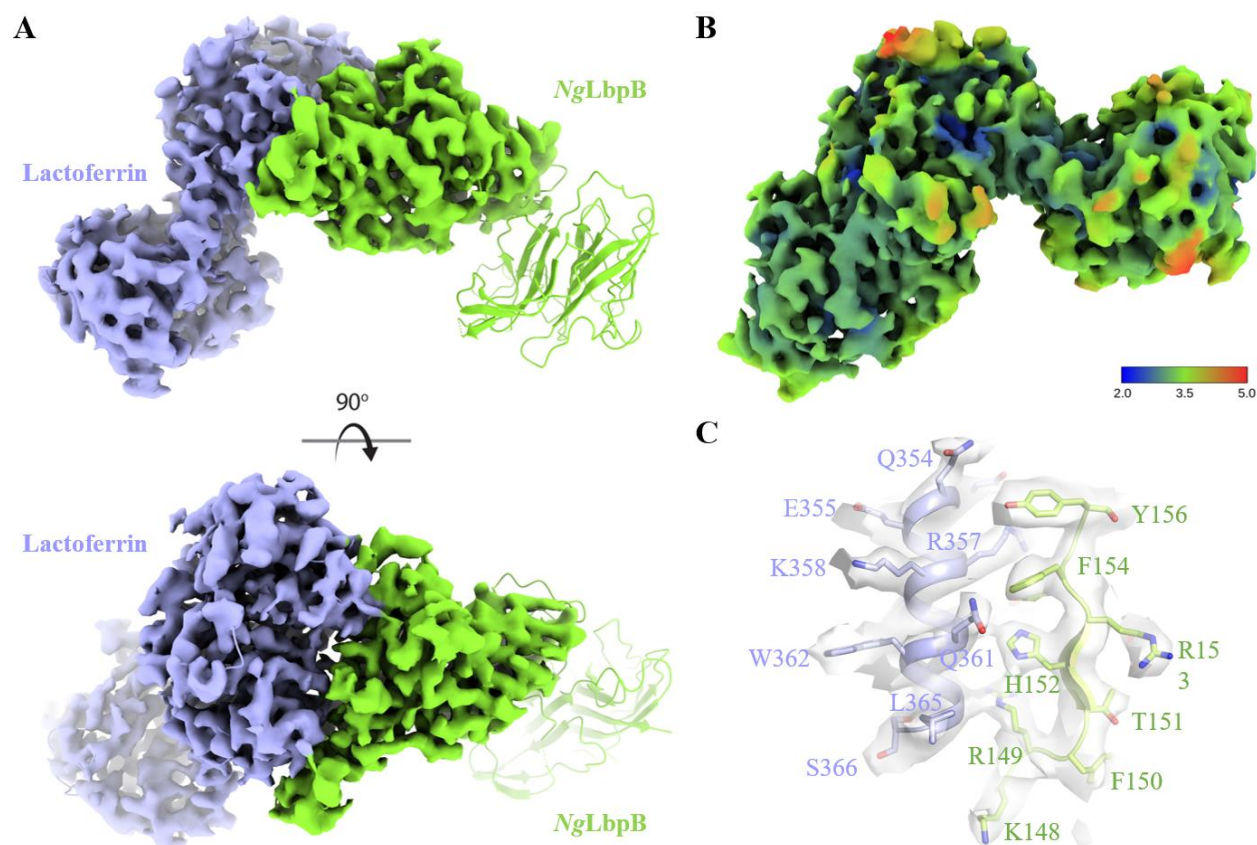


Figure 2.10. The 3.65 Å cryo-EM reconstruction of the NgLbpB-lactoferrin complex. (A) Orthogonal views of the NgLbpB-lactoferrin complex cryo-EM map with NgLbpB (green) and lactoferrin (violet) models docked in it. (B) NgLbpB-lactoferrin cryo-EM map surface colored based on local resolution. (C) Visualization of final cryo-EM map quality with map shown in grey transparent surface, secondary structure elements in cartoon and residues shown in sticks. NgLbpB and lactoferrin are colored green and violet, respectively.

density, the residues 338-704 were rigid body placed based on the crystal structure of the *NmLbpB*-lactoferrin complex. Geometric validation of the model showed that 78.31% and 21.44% residues were in favored and allowed regions, respectively, in the Ramachandran Plot, whereas only 0.25% residues were outliers. Data collection, processing, model refinement, and validation parameters are summarized in **Table 2.2**. Given the higher resolution and completeness, we will focus on *NmLbpB*-lactoferrin complex crystal structure here onwards unless mentioned otherwise.

2.4.8 Comparison of the *NmLbpB*-lactoferrin crystal structure with the SAXS structure

We compared our *NmLbpB*-lactoferrin crystal structure with the SEC-SAXS solution scattering data. Theoretical scattering curve for the *NmLbpB*-lactoferrin crystal structure was calculated using CRY SOL¹⁷³ with maximum q (or s) value of 0.30 and other parameters at default

values. This calculated scattering curve was fitted with the experimental curve, and the correlation between the curves was measured in terms of the χ^2 value. The fitting of calculated and experimental scattering curves showed highly similar data with a χ^2 value of 1.0, thus suggesting that the *NmLbpB*-lactoferrin complex exists in a similar arrangement in solution as observed in the crystal structure (**Figure 2.8C**).

2.4.9 Structural features of *NmLbpB* in complex with lactoferrin

NmLbpB has a similar architecture as *NmTbpB* (PDB id: 3V8U¹²¹); RMSD 1.8 Å) (**Figure 2.11A**). The N-lobe, composed of residues 1-342, contains two domains, an N-terminal handle

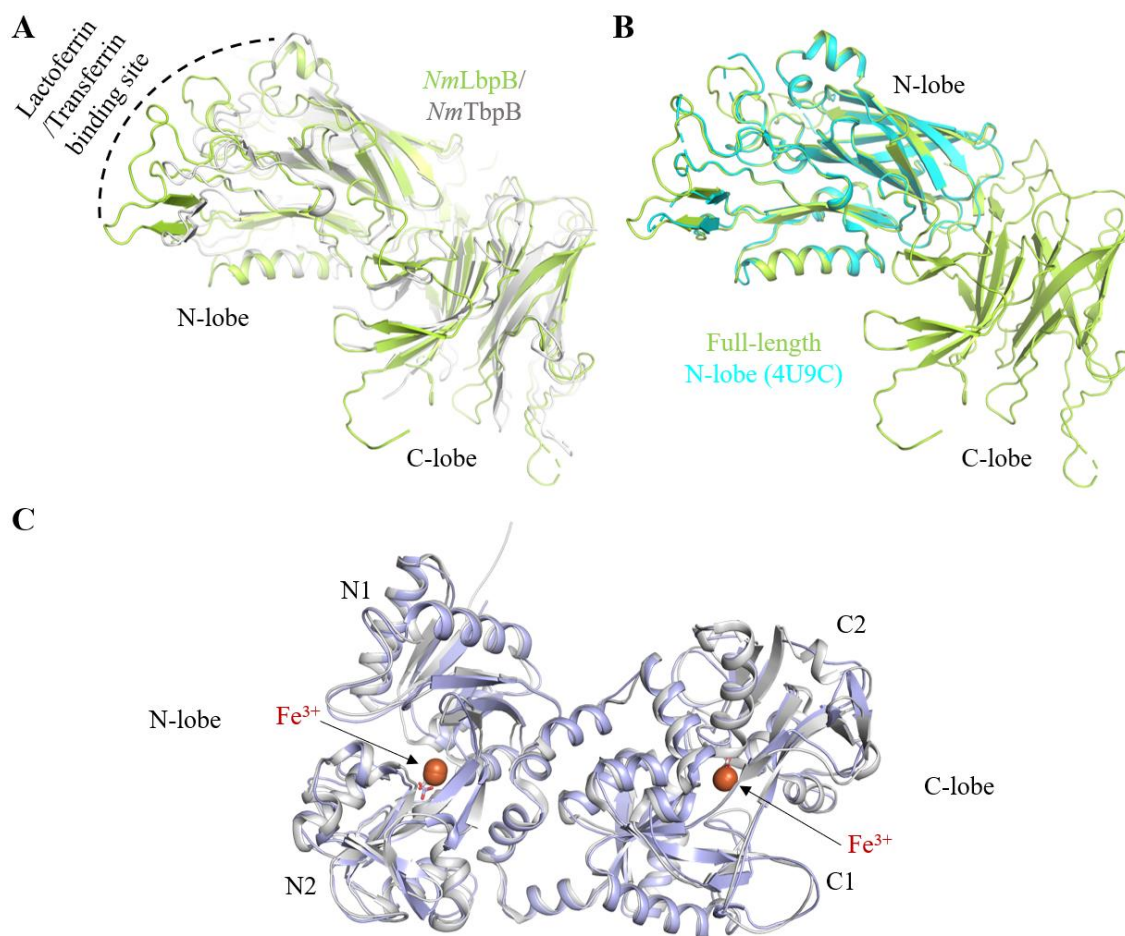


Figure 2.11. Structural comparisons of *NmLbpB* and lactoferrin with uncomplexed structures. Structural alignment of *NmLbpB* (green) with *NmTbpB* (grey) (PDB ID 3V8U⁴³) (A) and *NmLbpB* N-lobe (cyan) (PDB ID 4U9C¹⁴²) (B). (C) Superposition of lactoferrin from the complex (light blue) with holo-lactoferrin (grey) (PDB ID 2BJJ¹²⁴) suggests lactoferrin adopts iron-bound closed conformation.

domain (N_h) (residues 45-173), and an eight-stranded β -barrel domain (N_β) (residues 174-342). The handle domain contains four anti-parallel β -strands and a surface exposed α -helix between β -strand 1 and 2. The handle domain β -sheets pack against the β -barrel domain. The β -strands in the barrel are connected through surface exposed loops, which form a ‘cap region’ along with surface exposed loops of the handle domain. The *NmLbpB* N-lobe structure in the complex matches closely to the previously reported crystal structure (PDB ID: 4U9C¹⁴², chain B) with RMSD of 0.345 Å (for 260 C α atoms) (**Figure 2.11B**).

The *NmLbpB* C-lobe (residues 359-718) displays elevated disorder as observed in the B-factor plot compared to the remaining structure (**Figure 2.8B**). Several loop regions in the C-lobe are completely disordered and therefore could not be modelled. Like the N-lobe, the C-lobe also contains a handle domain (residues 359-540) and an eight stranded β -barrel domain (residues 541-718), along with long anionic loops. The C-lobe β -barrel domain is similar to the N-lobe β -barrel domain (RMSD 2.28 Å over 467 atoms), with differences arising from the loop regions. Unlike the N-lobe, the C-lobe handle domain is composed of six-stranded β -sheets packed against the C-lobe β -barrel domain and is flanked by two antiparallel β strands. The *NmLbpB* C-lobe interfaces with the N-lobe primarily through their handle domains. The base of the N-lobe handle and β -barrel domains (opposite to cap region) form hydrophobic and electrostatic interactions with the C-lobe handle domain and covers a surface area of 937.8 Å². The residues at the N/C inter-lobe interface are highly conserved among *NmLbpBs*²⁵.

In the *NmLbpB*-lactoferrin crystal structure, sufficient density was present to build nearly all of lactoferrin, except for residues 1-4. Lactoferrin is composed of two lobes, the N-lobe and the C-lobe. These lobes are further subdivided into N1 and N2 for the N-lobe, and C1 and C2 for the C-lobe. The nomenclature and boundaries for the subdomains are based on previous holo-lactoferrin structure¹⁹¹. Two iron ions are present in the structure, one in each lobe. Iron in the N-lobe is coordinated by residues D61 (N1), Y93 (N2), Y193 (N2), and H254 (N1), along with a carbonate ion; the parenthesis represents the domain location of the residues. Likewise, the C-lobe iron is coordinated by residues D396 (C1), Y436 (C2), Y529 (C2), and H598 (C1), along with a carbonate ion (**Figure 2.8A inset**). Comparison with previously reported structures of lactoferrin (PDB ID: 2BJJ¹²⁴; RMSD 1.3 Å) showed that both lobes of lactoferrin are in closed conformation (**Figure 2.11C**). Likewise, in the *NgLbpB*-lactoferrin cryo-EM structure, both lobes of lactoferrin

were modelled. Each lactoferrin lobe contained a pair of iron and carbonate ions. Both lobes of lactoferrin are in closed conformation.

2.4.10 The binding interface between LbpB and lactoferrin

Our binding studies using individual lobe constructs of *NmLbpB* showed that lactoferrin is recognized by the N-lobe of *NmLbpB*. In the *NmLbpB*-lactoferrin crystal structure, the N-lobe of *NmLbpB* interacts with the C-lobe of lactoferrin with extensive hydrogen bonding and salt-bridge networks encompassing $\sim 1760.8 \text{ \AA}^2$ of buried surface area. Residues at the ‘cap region’ in the *NmLbpB* N-lobe interact with both the C1 and C2 subdomains of lactoferrin (**Figure 2.12**).

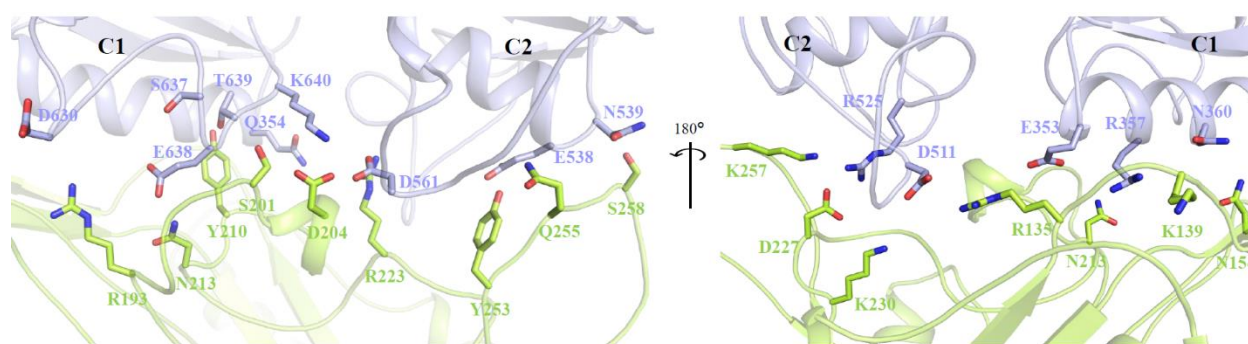


Figure 2.12. The *NmLbpB*-lactoferrin binding interface. *NmLbpB* interacts with both the C1 and C2 subdomains of lactoferrin with 1760.8 \AA^2 buried surface area.

K117 (N_h) from *NmLbpB* interacts with E515 (C2) of lactoferrin, whereas K139 (N_h) forms polar interactions with R357(C1) of lactoferrin. The N_h and N_β represent the handle and β -barrel domain in N-lobe of *NmLbpB*, respectively. R135 (N_h) from *NmLbpB* forms salt bridge contacts with E353 (C1) and D511 (C2) of lactoferrin. The cap region of the *NmLbpB* N-lobe β -barrel domain is involved in binding to both subdomains C1 and C2 of lactoferrin. Positively charged *NmLbpB* residues R193 (N_β), R223 (N_β), and K230 (N_β) interact with residues D630 (C1), D561 (C2), and E512 (C2) of lactoferrin, respectively. The *NmLbpB* residue Y210 (N_β) is located at the center of the interface and interacts with Q354 (C1) and T639 (C1) from lactoferrin, whereas D204 (N_β) interacts with D561 (C2) and K640 (C1). D227 (N_β) and K257 (N_β) of *NmLbpB* form salt bridge interactions with R525 (C2) and E538 (C2) of lactoferrin, respectively. Additional hydrogen bond and salt bridge interactions between *NmLbpB* and lactoferrin are listed in **Table 2.4**.

Table 2.4. Summary of interactions between *NmLbpB* and lactoferrin. The binding interface information was obtained by QtPISA analysis.

<i>NmLbpB</i>	Lactoferrin	Distance
Hydrogen bonds		
R135 [O]	R357 [NH2]	2.8
R135 [NH2]	Q513 [OE1]	2.9
A136 [O]	R357 [NH1]	2.9
K139 [O]	R357 [NH1]	2.6
N141 [OD1]	R357 [NE]	3.5
N154 [ND2]	N360 [O]	3.6
Y158 [OH]	E353 [OE2]	2.2
R193 [NH2]	D630 [O]	2.7
S201 [OG]	S637 [O]	2.9
S201 [OG]	T639 [N]	3.9
T203 [OG1]	K640 [NZ]	3.6
D204 [OD1]	D561 [N]	3.5
Y210 [OH]	Q354 [O]	3.0
Y210 [OH]	T639 [OG1]	3.2
N213 [ND2]	E638 [OE1]	2.8
Y220 [O]	Q513 [NE2]	2.5
K230 [NZ]	E512 [O]	3.5
Y253 [OH]	E538 [OE2]	2.6
Q255 [NE2]	A537 [O]	3.4
K257 [N]	E538 [O]	3.6
S258 [OG]	N539 [O]	3.0
Salt bridges		
K117 [NZ]	E515 [OE1]	3.4
R135 [NE]	E353 [OE1]	3.7
R135 [NH1]	D511 [OD2]	3.6
R135 [NH2]	D511 [OD1]	4.0
R135 [NH2]	D511 [OD2]	3.8
D204 [OD1]	K640 [NZ]	3.0
D204 [OD2]	K640 [NZ]	3.5
R223 [NE]	D561 [OD2]	3.9
R223 [NH2]	D561 [OD2]	3.6
D227 [OD1]	R525 [NH1]	3.5
D227 [OD2]	R525 [NH1]	2.8
D227 [OD2]	R525 [NH2]	3.4
K230 [NZ]	E512 [OE1]	2.9
K257 [NZ]	E538 [OE1]	3.1
K257 [NZ]	E538 [OE2]	3.5

In the *NgLbpB*-lactoferrin complex, the binding interface buries $\sim 1600 \text{ \AA}^2$ of surface area and is stabilized through electrostatic and hydrophobic interactions. The binding interface between *NgLbpB* and lactoferrin consists of 10 hydrogen bonds and 6 salt bridges (**Table 2.5**). The F208 of *NgLbpB* resides in a small hydrophobic pocket in the C1 subdomain of lactoferrin.

G137 of *NgLbpB* forms a hydrogen bond with the guanidino group of R357 in lactoferrin. *NgLbpB* residues T114 and D139 that are located at the N-lobe handle domain interact with lactoferrin residues Q513 and N360, respectively. Side chains of R191 and T207 residues in the *NgLbpB* N-lobe β -barrel domain form polar contacts with the backbone atoms of lactoferrin residues D630 and Q354, respectively. Additionally, *NgLbpB* residues H61, R113, K117, K221, and K228 form salt bridges with lactoferrin residues E367, D511, E512, and E515.

Table 2.5. Summary of interactions between *NgLbpB* and lactoferrin. The binding interface information was obtained by QtPISA analysis.

<i>NgLbpB</i>	Lactoferrin	Distance
Hydrogen bonds		
S71 [OG]	D630 [OD2]	3.3
T114 [O]	Q513 [NE2]	3.7
K117 [NZ]	Q513 [O]	3.0
Y131 [OH]	Q513 [OE1]	3.1
G137 [O]	R357 [NH1]	2.3
D139 [OD2]	N360 [ND2]	2.4
R191 [NH2]	D630 [O]	2.8
S200 [N]	E638 [O]	3.6
T207 [OG1]	Q354 [OE1]	3.5
D212 [OD2]	Q361 [NE2]	3.8
Salt bridges		
H61 [NE2]	E367 [OE2]	3.6
R113 [NH1]	D511 [OD2]	3.2
R113 [NH1]	E515 [OE1]	3.6
K117 [NZ]	E515 [OE2]	2.7
K221 [NZ]	E515 [OE2]	3.7
K228 [NZ]	E512 [OE1]	3.5

2.4.11 Probing the LbpB-lactoferrin interaction interface using mutagenesis

Our structural studies showed that the N-lobe of *NmLbpB* interacts with C-lobe of lactoferrin and provided further insights into the direct residue-residue interactions. To probe the binding interface, we created site-directed mutants of *NmLbpB* and probed their binding properties with lactoferrin using solid-phase binding assay, ELISA, and ITC (**Figure 2.13 and 2.14**). We mutated residues located at the ‘cap region’ of the *NmLbpB* N-lobe, which either form polar interactions or are situated at the interface with lactoferrin

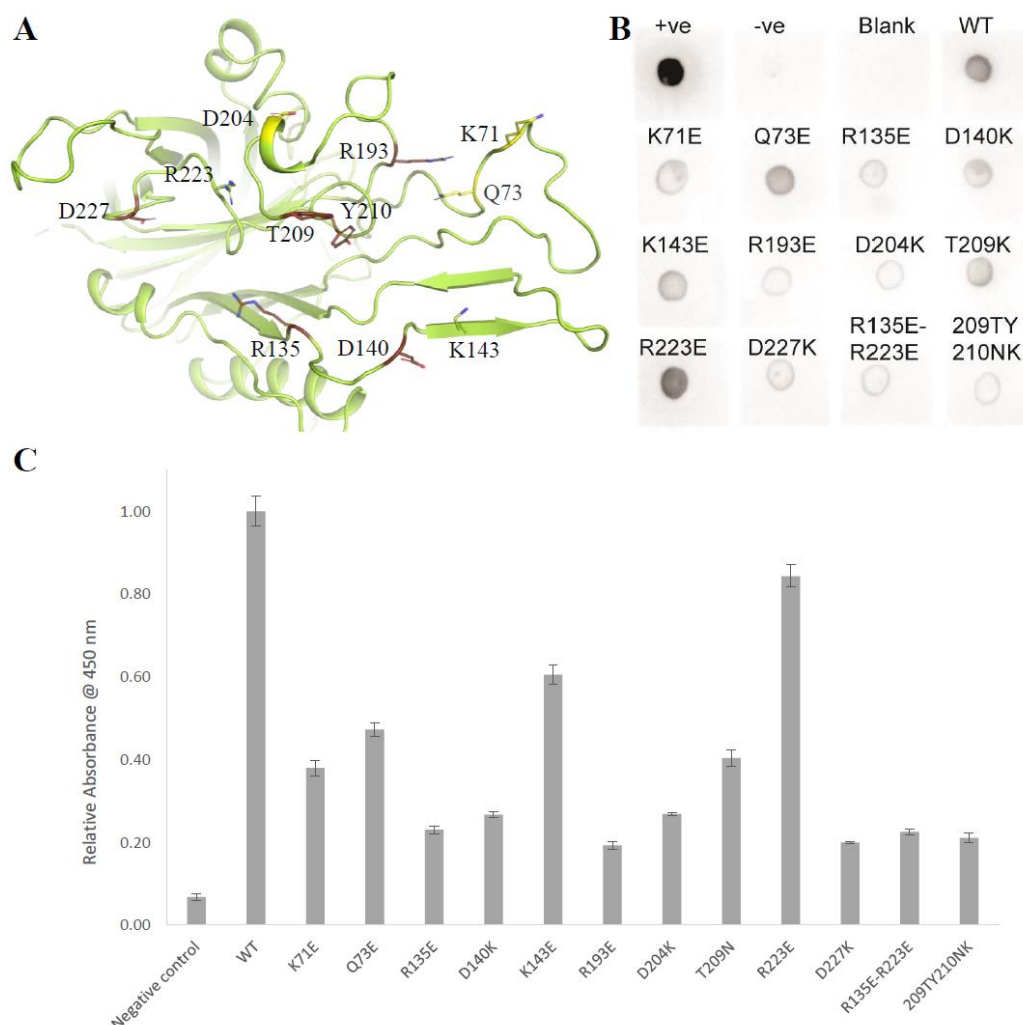


Figure 2.13. Probing the lactoferrin binding interface of *NmLbpB*. (A) The zoomed view of residues along the lactoferrin binding interface in *NmLbpB*. Residues are colored based on the effect of point mutation on lactoferrin binding. Residues with significant (red), moderate (yellow), and no (green) effect on lactoferrin binding upon mutations are shown in sticks. Representative results of solid-phase binding assay (B) and ELISA (C) to test the effects of point-mutations of *NmLbpB* on lactoferrin binding.

(**Figure 2.13A**). The ELISA and solid-phase binding assay showed that the *NmLbpB* charge reversal mutations R135E, D140K, R193E, D204K, and D227K reduce lactoferrin binding by > 70% (**Figure 2.13B and C**). We also created double mutants T209N-Y210K and R135E-R223E that also reduced lactoferrin binding by ~80%. Additionally, point mutations K71E, Q73E, K143E, and T209N slightly effected lactoferrin binding (between 40-60%), whereas R223E had no significant effect. We also measured dissociation constants for the selected *NmLbpB* variants using ITC. The wild-type *NmLbpB* binds tightly to lactoferrin with a K_d of 0.14 μ M (**Figure 2.14A**). The R135E mutant showed reduced lactoferrin binding with a K_d of 11.5 μ M, which is an

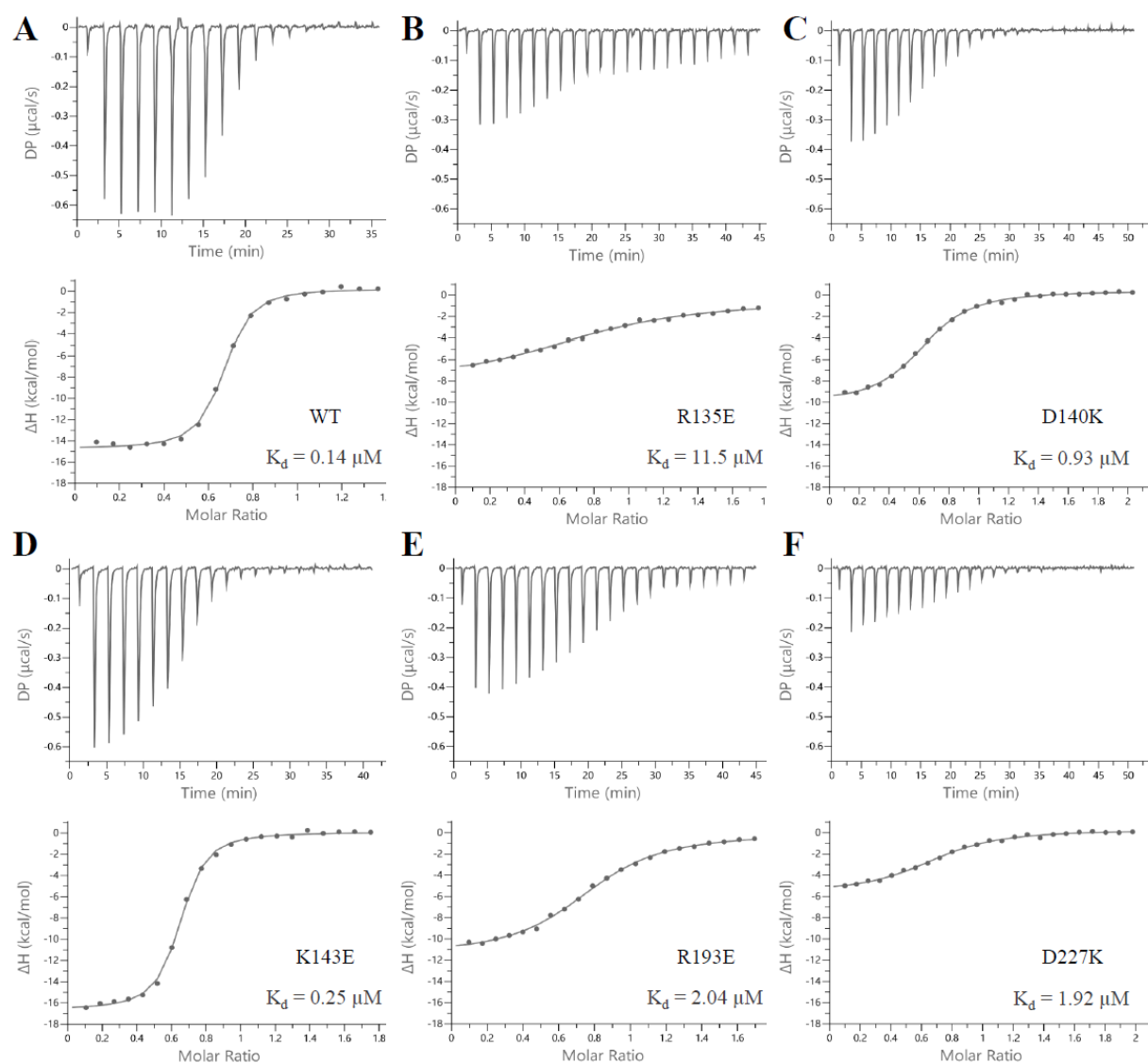


Figure 2.14. ITC analysis of lactoferrin binding to select *NmLbpB* mutants. ITC analysis of lactoferrin binding to *NmLbpB* wild-type (A) and point mutants (B-F). Top panels display the raw ITC data whereas bottom panels show the associated isotherms upon single binding site model fitting

Table 2.6. Summary of ITC data for lactoferrin titrations with *NmLbpB*.

Protein	K_d (μM)	ΔH (kcal/mol)	ΔS (kcal/mol/deg)	n
WT	0.1 ± 0.1	-15.8 ± 2.5	-0.02 ± 0.01	0.8 ± 0.1
R135E	11.5 ± 1.3	-9.7 ± 1.1	-0.02 ± 0.01	0.9 ± 0.1
D140K	0.9 ± 0.01	-9.5 ± 0.1	-0.004 ± 0.0004	0.6 ± 0.01
K143E	0.3 ± 0.2	-16.7 ± 0.2	-0.03 ± 0.01	0.6 ± 0.04
R193E	2.0 ± 0.2	-11.8 ± 0.3	-0.014 ± 0.01	0.75 ± 0.04
D227K	1.9 ± 0.6	-5.4 ± 0.3	0.008 ± 0.002	0.7 ± 0.1

approximately 80-fold weaker binding affinity than wild type *NmLbpB* (**Figure 2.14B**). Also, the D140K, K143E, R193E, and D227K mutants showed ~6.5, ~2, ~14 and ~14-fold weaker binding affinities, respectively, as compared to the wild type (**Figure 2.14C-F and Table 2.6**). The ITC measurements are consistent with the ELISA and solid-phase binding assays.

Likewise, binding studies of *NgLbpB* mutants, K135E and D139K, completely abolished lactoferrin binding whereas D202K showed reduced binding (**Figure 2.15**). These results suggest that the *NmLbpB*-lactoferrin interface observed in the crystal structure represents a physiological complex.

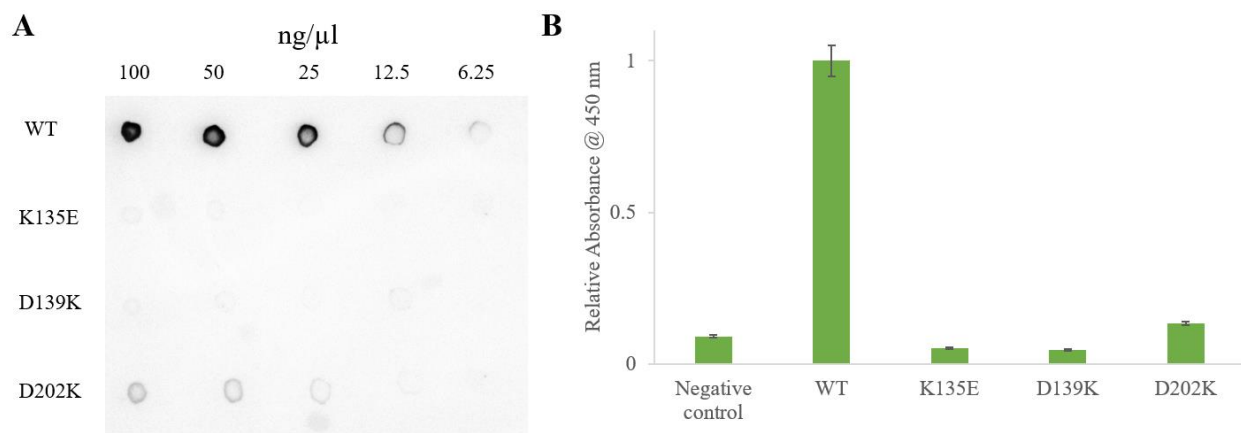


Figure 2.15. Probing the lactoferrin binding interface of *NgLbpB*. Representative results of solid-phase binding assay (A) and ELISA (B) to test the lactoferrin binding show that point mutants K135E and D139K completely abolish lactoferrin binding as compared to wild-type *NgLbpB*. D202K mutant *NgLbpB* also shows significant reduction in lactoferrin binding.

2.5 Discussion and conclusion

Iron acquisition pathways in bacterial pathogens are attractive targets for vaccine and antibacterial drug development. Considering the essential nature of iron in bacterial survival, growth, and pathogenesis, understanding the molecular mechanisms of iron acquisition is critical. *Neisseria* utilize outer membrane proteins to hijack and acquire iron from host iron-containing proteins. Lactoferrin binding proteins LbpA and LbpB recognize lactoferrin and then extract iron from it. Studies reporting the release of LbpB from the bacterial surface by NalP have suggested that either LbpB may not be involved in iron import or it serves multiple functions¹⁴⁴.

In this study, we characterize the role of LbpB in iron import from human lactoferrin. Using solid-phase binding assays to test lactoferrin binding, we showed that the N-lobe of *NmLbpB* binds

to lactoferrin. Previously, crosslinking coupled to mass spectroscopy (XL-MS) studies of the complex formation between *NmLbpB* and lactoferrin suggested the possibility of two lactoferrins binding to *NmLbpB*¹¹⁶. However, in our studies using SEC, static SAXS, and SEC-SAXS, we observe a 1:1 complex between *NmLbpB* and lactoferrin in solution with no observation of a 1:2 complex (**Table 2.3**). Additionally, it has been proposed that both lobes of *NmLbpB* participate in lactoferrin binding¹¹⁶. Our solid-phase binding assays showed that the N-lobe of *NmLbpB* retains its ability to bind to lactoferrin, whereas the C-lobe alone does not bind to lactoferrin (**Figure 2.7**). These observations were further supported by the structures of LbpB-lactoferrin complexes, which showed a 1:1 stoichiometry and provided molecular insights into the binding interface (**Figures 2.8A and 2.10A**). The structures showed that the ‘cap region’ of LbpB binds to the C-lobe of lactoferrin. Moreover, the mutations along the binding interface in the N-lobe of LbpB significantly reduced the lactoferrin binding (**Figures 2.13, 2.14 and 2.15**).

The overall architecture of the *NgLbpB*-lactoferrin complex shows high structural similarity with the *NmLbpB*-lactoferrin crystal structure (**Figure 2.16**). An alignment of the *NmLbpB*-lactoferrin with *NgLbpB*-lactoferrin had an overall RMSD of 3.7 Å. However, alignment just along the protein-protein interaction interface showed improved fitting with 1.4 Å RMSD. Inspection of binding interfaces in the *NmLbpB* and *NgLbpB* complexes with lactoferrin demonstrated a highly similar LbpB-lactoferrin interface (**Figure 2.16, bottom panel**). Besides these similarities, we observed one major differences between the complexes: rigid body rotation of lactoferrin. A difference was observed in the lactoferrin position in the complex. In the *NgLbpB*-lactoferrin structure, the N-lobe of lactoferrin undergoes ~12° rigid body rotation relative to the lactoferrin position in the *NmLbpB*-lactoferrin crystal structure (**Figure 2.16A, top panel**). We hypothesized that this structural difference is an artifact of crystal packing in the *NmLbpB*-lactoferrin crystal. Alternatively, if the conformational change is important for the function of LbpB, the exact nature remains to be determined.

The iron bound lactoferrin attains a closed conformation, in which the subdomains in the lobes are compacted and interact with each other to create iron binding site¹²⁴. In LbpB-lactoferrin complex, both proteins interact without much change in their overall structures (**Figure 2.11B and C**). Together, these observations corroborate LbpB’s preference towards holo-lactoferrin over apo-lactoferrin. In apo-lactoferrin, release of the Fe³⁺ ions induce a conformational transition from a closed state to an open state, and this conformational transition would disrupt the LbpB binding

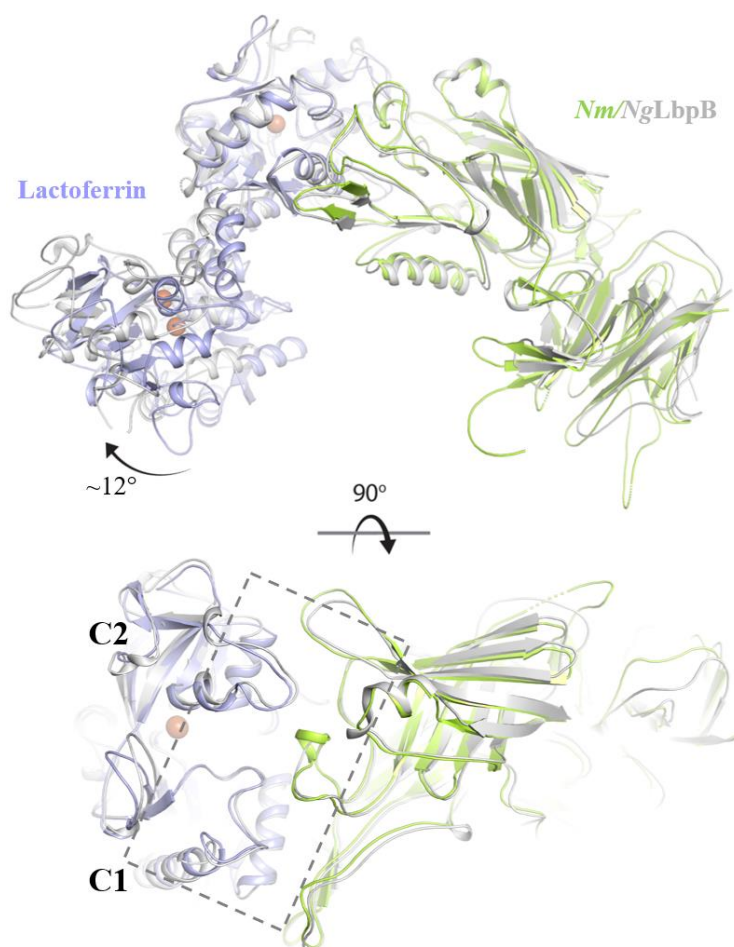


Figure 2.16. Structural comparison of *NgLbpB*-lactoferrin cryo-EM structure with the *NmLbpB*-lactoferrin crystal structure. (A) *NmLbpB*-lactoferrin (green/violet) and *NgLbpB*-lactoferrin (grey) show similar architecture with almost identical binding interface (grey dashed box). Alignment along the LbpB-lactoferrin binding interface showed $\sim 12^\circ$ rigid body rotation of lactoferrin in *NgLbpB*-lactoferrin.

site on lactoferrin, leading to the potential inhibition of LbpB binding. Additionally, the LbpB-lactoferrin structures suggest that upon complex formation both proteins are confined to a specific conformation, particularly lactoferrin, which is in iron-bound closed conformation.

As mentioned earlier, LbpB is homologous to TbpB, which is also involved in iron acquisition through the human transferrin protein. Since *NmLbpB* shares high structural similarity to *NmTbpB* (PDB id: 3V8U⁴³; RMSD 1.8 Å), it is possible that *NmLbpB* and *NmTbpB* might also share similar functions. This idea is further reinforced by the similar architecture of the *NmLbpB*-lactoferrin complex to the *NmTbpB*-transferrin complex (PDB ID: 3VE1¹²¹), where a structural alignment focused on the interacting lobes of these proteins has an overall RMSD of 1.2 Å over

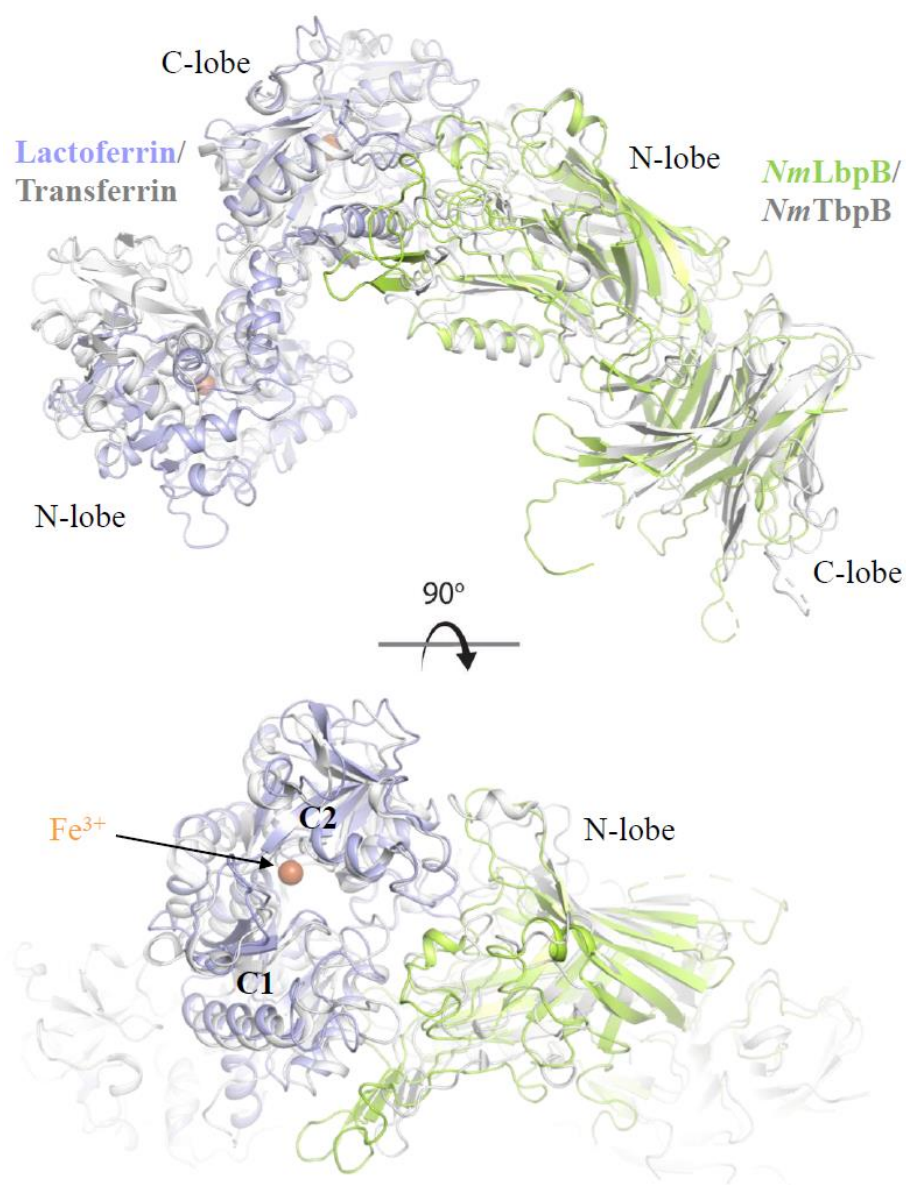


Figure 2.17. Comparison of the *NmLbpB*-lactoferrin and *NmTbpB*-transferrin structures. Both complexes have similar architecture such that C-lobes of lactoferrin (light blue) and transferrin (grey) interact with N-lobe of *NmLbpB* (green) and *NmTbpB* (grey), respectively.

429 C α atoms (**Figure 2.17**). This suggests that, like *NmTbpB*, the role of *NmLbpB* may be to capture and trap lactoferrin in an iron-loaded state for delivery to *NmLbpA*.

By combining our structural and functional data with previous observations, we propose the following model for the role of LbpB in iron acquisition from lactoferrin (**Figure 2.18**). At the surface of *Neisseria*, LbpB recognizes and binds to iron-bound lactoferrin. This interaction is mediated by an extensive protein-protein interface, where LbpB captures and traps the lactoferrin

in an iron-bound conformation. Subsequently, the LbpB-lactoferrin complex is recognized by LbpA, where it induces conformational changes in lactoferrin and extracts iron, which is then transported across the outer membrane through the barrel domain of LbpA in a TonB-dependent manner.

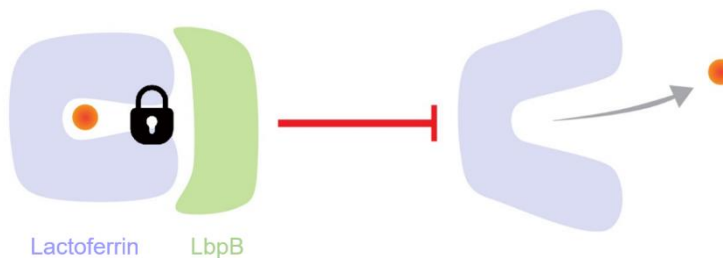


Figure 2.18. The role of LbpB in iron import. We propose that LbpB binds to lactoferrin and locks it in an iron-bound closed conformation for delivery to LbpA for iron import.

In summary, this study provides insights into lactoferrin recognition by *Nm*LbpB and defines the stoichiometry, binding interface, and the functional implications of the interaction during Neisserial pathogenesis. The structures provide a framework for understanding LbpB's selectivity towards holo-lactoferrin over apo-lactoferrin. The anionic loops of *Nm*LbpB are disordered in our structure, which are further implicated to be involved in the protection against cationic antimicrobial peptide during pathogenesis¹⁴⁵. While this study enables us to understand the molecular mechanism behind the initial steps of iron acquisition from lactoferrin, further structural and functional studies are needed to identify the molecular determinants for iron extraction and transport across the outer membrane by LbpA.

Surface-exposed lipoproteins are important virulence factors and have been explored as vaccine candidates. The protein-based vaccines for Nme serogroup B use surface-exposed lipoprotein, Neisserial heparin binding antigen (NHBA) and Factor H binding protein (FHbp), as active ingredients¹⁵. Additionally, engineered TbpB antigens showed promising results for protection against Nme and Ngo⁴². Given, it is immunogenic and is present in all Nme isolates, LbpB is a potential vaccine candidate. Our structural and functional studies will aid in protein engineering and optimization of LbpB as an antigen for vaccines against Nme.

CHAPTER 3. STRUCTURAL INSIGHT INTO LACTOFERRICIN BINDING TO LBPB

3.1 Abstract

Lactoferricin (Lfcn) is a cationic antimicrobial peptide that is released when the lactoferrin protein is cleaved by the pepsin enzyme. Lfcn can rupture the bacterial membranes, thus providing a line of defense against invading pathogens. *Neisseria* employ a surface exposed lipoprotein, lactoferrin binding protein B (LbpB), to protect them against the Lfcn's antimicrobial effects. However, the underlying mechanism of LbpB's protection against Lfcn is poorly understood. In the current study, we probed the putative Lfcn binding site in the *Nm*LbpB. Our data show that the highly flexible anionic loops in the C-lobe of *Nm*LbpB contribute to Lfcn binding. To aid structural studies, we identified several antigen-binding fragments (Fab) against C-lobe of LbpB. We determined several structures of *Nm*LbpB C-lobe in complex with Lfcn and select Fabs. However, no ordered density for the anionic loops or Lfcn was observed.

3.2 Introduction

Initially, LbpB was identified as a surface-exposed lipoprotein involved in iron acquisition from lactoferrin, a host iron-containing glycoprotein. Probing the role of LbpB in iron import showed that, while it is not essential for sequestering iron, it does increase the rate of iron acquisition¹³⁶. Additionally, LbpB is released from the bacterial surface into culture medium by the NalP autotransporter¹⁴⁴. In the same study, it was shown that the release of LbpB from the bacterial surface may represent a novel process to confer protection against bactericidal antibodies¹⁴⁴. Furthermore, LbpB protects the Nme from the antimicrobial activity of the cationic host peptide Lfcn¹³². Nme harboring a LbpB mutant that lacks the charged region in the C-lobe were more susceptible to Lfcn compared to the wild-type¹⁴⁵. Several studies have speculated about the dual functions of LbpB in *Neisseria* pathogenesis^{139,144,146}. However, there are no structures of LbpB bound to Lfcn. Therefore, we used site-directed mutagenesis, isothermal titration calorimetry, and small-angle X-ray scattering (SAXS) to investigate Lfcn binding to *Nm*LbpB. To facilitate structural studies, we identified several Fab fragments against the C-lobe of LbpB and used X-ray crystallography to solve structures of the C-lobe in complex with Lfcn and select Fabs.

3.3 Methods

3.3.1 Construct design and cloning

The *NmLbpB* full-length and C-lobe constructs described in Chapter 2 were used to create mutants for Lfcn binding studies. The loop deletion mutants of *NmLbpB* were created using specific deletion primers to amplify DNA from the wild-type pHIS-Parallel2-*NmLbpB* plasmid by polymerase chain reaction (PCR). The PCR products were digested with DpnI enzyme overnight at 37°C. DH5 α cells were transformed with 5 μ L of the digestion reaction and then plated onto Luria Broth (LB) agar plates supplemented with carbenicillin (100 μ g/mL) for overnight growth at 37°C. Single colonies were picked, grown overnight in 2XYT media, and the plasmids were extracted. The desired deletions were confirmed by DNA sequencing analysis.

For phage-display study, an Avi-tagged C-lobe construct of *NmLbpB*, a gene fragment encoding for the C-lobe with an N-terminus Avi-tag (GLNDIFEAQKIEWHE) was amplified from the wild-type pHIS-Parallel2-C-lobe plasmid by PCR. The PCR product was gel purified from a 1% agarose gel. The gene fragment and pHIS-Parallel2 vector were then digested with NcoI and XhoI restriction enzymes and ligated together. The ligation reaction mixture was transformed into DH5 α cells. Single colonies were grown in 2XYT media for plasmid isolation. The plasmids with the Avi-tag C-lobe were identified by DNA sequencing. The resultant construct encoded an N-terminus 6X-His-tag, followed by a TEV protease cut site, an Avi-tag, and the *NmLbpB* C-lobe.

3.3.2 Protein expression and purification

All the constructs used in the current study were expressed and purified using similar procedures. For expression, plasmids were transformed into BL21(DE3) cells and plated on LB agar plates supplemented with carbenicillin (100 μ g/mL) for overnight growth at 37°C. The obtained colonies were grown in 2XYT medium containing ampicillin (50 μ g/mL) overnight at 37°C. The inoculate cultures were sub-cultured into 500 mL Terrific Broth (TB) medium supplemented with ampicillin (50 μ g/mL) and grown at 37°C while shaking at 180 rpm. The temperature was reduced to 24°C once the optical density at 600 nm (OD₆₀₀) reached 0.5-0.6. Expression was induced by the addition of 0.4 mM of isopropyl β -D-thiogalactopyranoside (IPTG) for 9-12 hours. Subsequently, the cells were harvested by centrifugation at 6,000 rpm for 15 minutes at 4°C. The cell pellets were collected and stored at -80°C until use.

For purification, frozen cell pellets were resuspended in phosphate lysis buffer (1xPBS + 25 mM imidazole) supplemented with 0.4 mM phenylmethylsulfonyl fluoride (PMSF) and DNaseI (10 µg/mL). The cells were lysed using an Emulsiflex C3 (Avestin) with three passages at 15,000-18,000 psi. The cell lysate was centrifuged at 18,000 rpm for 30 minutes at 4°C. The supernatant was collected and passed over a 5 mL Hi-Trap Ni-NTA column (Qiagen) pre-equilibrated with lysis buffer. The column was washed with 60 mL of wash buffer 1 (1xPBS + 35 mM imidazole) followed by a 20 mL wash buffer 2 (1xPBS + 50 mM imidazole). The protein was eluted with 30 mL elution buffer (1xPBS + 250 mM imidazole). The elution fractions were pooled together, and the 6X-His-tag was cleaved using TEV protease while dialyzing against dialysis buffer (1xPBS + 5 mM β-mercaptoethanol). The dialyzed protein mixture was again passed over a Ni-NTA column and the tag-less sample was collected in the flow-through. The protein was diluted to 20 mM NaCl salt concentration and loaded over a HiTrap Q FF anion exchange chromatography column (Cytiva). The column was washed with 25 mL of buffer 1 (20 mM Tris pH 7.5, 20 mM NaCl) followed by 30 mL of buffer 2 (20 mM Tris pH 7.5, 365 mM NaCl). Finally, the protein was eluted with elution buffer (20 mM Tris pH 7.5, 450 mM NaCl). The protein fractions were pooled, concentrated, and subjected to size-exclusion chromatography (SEC) purification using a Superdex 200 Increase 10/300 GL column (Cytiva). The protein fractions were visualized on an SDS-PAGE gel; and those containing the desired protein were pooled and concentrated.

The *NmLbpB*-LfcN complex was formed by incubating *NmLbpB* with 4x molar excess of LfcN at 4°C for 1 hour. Access LfcN was removed using a Superdex 200 Increase 10/300 GL column using 1xPBS buffer. Fractions containing the complex were pooled and concentrated.

3.3.3 Isothermal titration calorimetry

LfcN binding to various *NmLbpB* variants was examined using a Nano ITC instrument (TA instruments). For LfcN binding, the titrations were performed at 10°C with 300 µL of the *NmLbpB* variant at a 30 µM final concentration in the sample cell. LfcN (600 µM) was injected into the sample cell 20 times at 5-minute intervals with stirring at 300 rpm. The ITC data was recorded and analyzed with the NanoAnalyze software (TA instruments). The binding isotherm was obtained by fitting the experimental data with the minimized independent binding model. The binding and thermodynamic parameters were calculated through binding isotherm analysis.

To assess the effect of Lfcn on lactoferrin binding to *NmLbpB*, we obtained the dissociation constant (K_d) value of lactoferrin binding to *NmLbpB* \pm Lfcn using the Nano ITC instrument (TA instruments). The lactoferrin binding titrations were performed at 25°C. For the titrations, 300 μ M of lactoferrin was injected into the sample cell, which contained, 30 μ M of *NmLbpB* \pm Lfcn, for over 20 injections at 300 rpm. The data was collected and analyzed with the NanoAnalyze software (TA instruments) using the minimized independent binding model.

All the ITC experiments were performed at least twice with representative data shown.

3.3.4 SEC-SAXS analysis of the Nme LbpB-Lfcn complex

To characterize the effect of Lfcn binding on the protein structure, the purified proteins were subjected to SEC-SAXS in the absence or presence of Lfcn. The SEC-SAXS data was collected at beamline 18-ID of the Advanced Photon Source (APS) at the Argonne National Laboratory. The data collection and processing were performed using a similar procedure as described in Chapter 2. Briefly, the samples were injected, onto a Superdex 200 Increase 10/300 GL column (Cytiva), the elution sample was exposed to a continuous X-ray beam, and the scattering data was recorded on a Pilatus3 1M detector (Dectris). After initial data processing using the in-house beamline software, the data was imported into the BioXTAS RAW¹⁷⁴. The LC series analysis was performed for buffer subtraction and sample frame range identification. The buffer subtracted frames were averaged and subjected to Guinier extrapolation for identifying the q -range. Finally, GNOM¹⁷³ was used to obtain pair distance distribution function $P(r)$ for calculating the radius of gyration (R_g) and maximum distance D_{max} values.

3.3.5 Biotinylation and streptavidin pull-down

The Avi-tagged C-lobe was purified as described in section 3.3.2. For biotinylation, the reaction mixture contained 40 μ M of Avi-tagged C-lobe protein, 50 mM bicine buffer at pH 8.3, 10 mM ATP, 10 mM MgOAc, 50 μ M D-biotin, and 2.5 μ g of the BirA biotin-protein ligase enzyme for every 10 nmol substrate. The biotinylation reaction was performed overnight at 4°C. Excess biotin was removed by SEC. The SEC fractions containing the sample were pooled and concentrated.

Biotinylation of the sample was evaluated using a streptavidin pull-down assay. A slurry containing streptavidin magnetic beads were aliquoted into a 1.5 mL microcentrifuge tube and washed with 1x PBS buffer. The beads were incubated with ~3 µg of biotinylated protein at room temperature for 25 minutes. The unbound protein was removed, and beads were washed three times, with 40 µL of PBS buffer for each wash. Finally, the beads were resuspended in 40 µL of PBS buffer. Non-biotinylated protein was used as a control for the pull-down, and the samples were analyzed by SDS-PAGE.

3.3.6 Selection of phage display Fabs

The phage display experiments were conducted by Dr. Satchal Erramilli in collaboration with Prof. Anthony Kossiakoff's lab at University of Chicago, Chicago, IL, USA. Biotinylated C-lobe was used for biopanning for Fab selection. Four rounds of phage display selection were performed in the presence of 50 µM Lfcn. In the first round, 200 nM of the C-lobe was immobilized onto streptavidin beads. The phage-library was mixed and incubated. After extensive washing, remaining bound phages were amplified by infecting and growing XL1-Blue cells in 2XYT medium supplemented with ampicillin and M13-K07 helper phage. To increase selection stringency, antigen concentrations were reduced in subsequent rounds, resulting in 20 nM in round 4. The sequences of the phage pool in the final round were analyzed to identify unique binders.

To validate binding, all unique binders were tested using single-point phage enzyme linked immunosorbent assay (ELISA). The 96-well plates were coated with 2 µg/mL of neutravidin. XL1-Blue cultures containing unique binders (one unique binder per culture) were grown overnight for phage amplification and secretion. The supernatant was obtained by centrifugation and then diluted 10-fold. The phages were transferred to ELISA wells containing either buffer, immobilized C-lobe, or immobilized C-lobe with 10 µM of Lfcn. Unbound phages were removed, and the beads were washed. The horseradish peroxidase (HRP)-conjugated anti-M13 mouse monoclonal antibody was added to the wells and incubated. Upon removal of excess antibody, TMB substrate was added for color development. Finally, the reaction was quenched with 1.0 M HCl, and the absorbance at 450 nm was measured. The comparison of absorbance between buffer and C-lobe ± Lfcn was used as the criteria for selecting Fab fragments for the next step.

3.3.7 Fab expression and purification

Following phage selection and the ELISA assay, 5 Fabs were selected for further characterization. These Fab fragments were cloned into the RH2.2 expression vector. These plasmids were transformed into BL21(DE3) cells and plated on LB agar plates supplemented with carbenicillin (100 µg/mL). Single colonies were picked and grown overnight in 2XYT medium supplemented with ampicillin (50 µg/mL). These inoculate cultures were transferred to 500 mL 2XYT cultures and grown at 37°C till the OD₆₀₀ reached 0.6-0.8. Fab expression was induced by adding 0.4 mM IPTG. Cells were grown for an additional 4 hours at 37°C while shaking at 180 rpm. Subsequently, cells were harvested by centrifugation at 6,000 rpm and stored at -80°C until use.

For protein purification, cells were thawed and resuspended in cold 1xPBS buffer supplemented with DNaseI (10 µg/mL) and 0.4 mM PMSF. Cells were lysed using an Emulsiflex C3 (Avestin) by three passes at 15,000-18,000 psi. The lysed cells were heated in a water bath at 65°C for 30 minutes, followed by centrifugation at 18,000 rpm for 30 minutes at 4°C. The supernatant was collected and used for affinity purification using a 5 mL Protein-L column pre-equilibrated with 1xPBS buffer. The column was washed with 40 mL of 1xPBS buffer, followed by additional washing with a 25 mM acetic acid linear gradient. Finally, the Fabs were eluted with 100 mM acetic acid. The eluted protein was pooled together and subjected to dialysis against 1xPBS buffer overnight. Upon dialyzing, Fabs were concentrated to the desired concentration for further studies.

3.3.8 Formation of the C-lobe-Lfcn-Fab complexes

For structural studies, the C-lobe was mixed with a four-molar excess of Lfcn at 4°C for 45 minutes, which was then followed by an addition of 1.5-2 molar excess of Fab. The reaction mixture was incubated for an additional 45 minutes at 4°C and subsequently injected onto a Superdex 200 Increase 10/300 GL column (Cytiva) pre-equilibrated with 1xPBS buffer. The formation of the complex was further confirmed by running the elution fractions on an SDS-PAGE gel. The desired fractions were pooled together and concentrated for crystallization trials.

3.3.9 Crystallization and data collection

For crystallization, the C-lobe-Lfcn-Fab complexes were concentrated to 12-15 mg/mL. Hanging-drop vapor diffusion crystal trays were set up using the Mosquito LCP crystallization robot (SPT Labtech) using commercial screens and incubated at 20°C. Crystal trays were monitored using an automated Rock Imager 1000 Duo system (Formulatrix). Initial hits were optimized in 96-well crystal trays using a Dragonfly screen optimization robot (SPT Labtech). Well-ordered crystals of the C-lobe-Lfcn-MP1 complex were grown in 0.25 M magnesium formate dihydrate, 0.1 M sodium cacodylate, pH 6.5, and 22% w/v PEG3000. Similarly, the C-lobe-Lfcn-MP2 crystals were obtained in reservoir solution 0.1 M Bis-Tris: HCl pH 5.5 and 25% w/v PEG3350. Crystals for the C-lobe-Lfcn-MP4/MP5 complex were also obtained, but only diffracted to 9 Å resolution and could not be improved. Single crystals were harvested at room temperature and then flash frozen in liquid nitrogen for data collection. Crystal screening and subsequent data collection was performed at the GM/CA 23-ID-D beamline at APS, Argonne National Laboratory.

3.3.10 Data processing, structure determination, and refinement

The diffraction data were indexed, integrated, and scaled using HKL2000¹⁷⁵. The data quality was assessed using Xtriage in Phenix¹⁷⁶. The structures were determined by molecular replacement (MR) method using Phaser-MR (Phenix)¹⁷⁶ with the *NmLbpB* C-lobe (PDB Id 7JRD¹⁸⁸, Chapter 2) and sAB-158 (PDB ID 5CWS¹⁹²) as search ensembles. For MR, sAB-158 was split into a constant and variable domain. The models were built iteratively with COOT¹⁷⁸ and subsequently refined with phenix.refine¹⁷⁹. Additional data processing, refinement, and validation parameters are summarized in **Table 3.1**. PyMOL (Schrodinger) was used for model visualization, structural analysis, and figure preparation.

3.4 Results

3.4.1 The C-lobe anionic loops of LbpB contribute to Lfcn binding

Although it has been shown that LbpB can protect *Neisseria* from the antimicrobial peptide Lfcn, there are no experimental structure of LbpB bound to Lfcn. To investigate Lfcn binding to LbpB, *NmLbpB* lacking its N-terminus signal sequence was expressed and purified as described in chapter 2. We employed ITC to study Lfcn binding to *NmLbpB*. The isotherm analysis showed

that Lfcn binds to *NmLbpB* with a K_d value of 3.65 μ M and an enthalpy change (ΔH) of -11.4 kcal/mol (**Figure 3.1A**).

LbpB contains large flexible anionic loops in the C-lobe that have been implicated to be involved in Lfcn binding¹⁴⁵. The loop boundaries were determined based on the *NmLbpB*-lactoferrin crystal structure (**Figure 3.1B**). Further sequence and structure analysis identified loops consisting of residues 372-383, 445-526, and 665-698 as largely anionic (**Figure 3.1C**). To probe the putative Lfcn binding site, we created deletion mutants individually lacking one of the C-lobe surface loops. The deletion mutants were purified using the same procedure as the wild type. We evaluated their ability to bind to Lfcn using ITC; and compared the K_d and ΔH values to the wild

Table 3.1. Data collection, processing, and refinement parameters for the *NmLbpB* C-lobe in complex with Lfcn and MP1/MP2 structures.

Data Collection	C-lobe-Lfcin-MP1	C-lobe-Lfcin-MP2
λ (Å)	1.0	1.0
Space group	P2 ₁ 2 ₁ 2 ₁	I2 ₁ 2 ₁ 2 ₁
a, b, c (Å)	120.83, 145.03, 157.68	94.90, 94.90, 410.26
α , β , γ (°)	90, 90, 90	90, 90, 90
Resolution (Å)*	50 - 3.55 (3.68 - 3.55)	50 - 3.7 (3.83 - 3.70)
Completeness (%)*	100 (100)	98.1 (96.2)
Redundancy*	12.2 (11.9)	8.8 (8.9)
R_{sym} †*	0.99 (2.9)	0.93 (4.05)
I / σ (I)*	4.14 (1.27)	5.67 (1.07)
CC _{1/2}	0.88 (0.35)	0.88 (0.21)
Refinement		
Resolution (Å)	48.82 - 3.55 (3.64 - 3.55)	41.03 - 3.70 (3.79 - 3.70)
No. reflections	33969 (3285)	19903 (1914)
$R^{\S}/R_{\text{free}}^{\P}$	0.23/0.28	0.24/0.33
R.M.S. deviations		
Bonds (Å)	0.005	0.005
Angles (°)	0.901	1.075
No. Protein atoms	15300	9722
No. Ligand atoms	0	0
No. Waters	0	0
B-factors (Å²)		
Wilson B	65.53	109.39
Protein	65.02	106.47
Ligands	0	0
Waters	0	0
Ramachandran Analysis[‡]		
Favored (%)	85.61	82.13
Allowed (%)	11.22	13.84
Outliers (%)	3.17	4.02

† $R_{\text{sym}} = \sum_{hkl,j} (|I_{hkl}| - \langle I_{hkl} \rangle) / \sum_{hkl,j} I_{hkl}$, where $\langle I_{hkl} \rangle$ is the average intensity for a set of j symmetry related reflections and I_{hkl} is the value of the intensity for a single reflection within a set of symmetry-related reflections.

§ R factor = $\sum_{hkl} (|F_o| - |F_c|) / \sum_{hkl} |F_o|$ where F_o is the observed structure factor amplitude and F_c is the calculated structure factor amplitude.

¶ $R_{\text{free}} = \sum_{hkl,T} (|F_o| - |F_c|) / \sum_{hkl,T} |F_o|$, where a test set, T (5% of the data), is omitted from the refinement.

‡ Performed using Molprobity within PHENIX.

* Indicates statistics for last resolution shell shown in parenthesis.

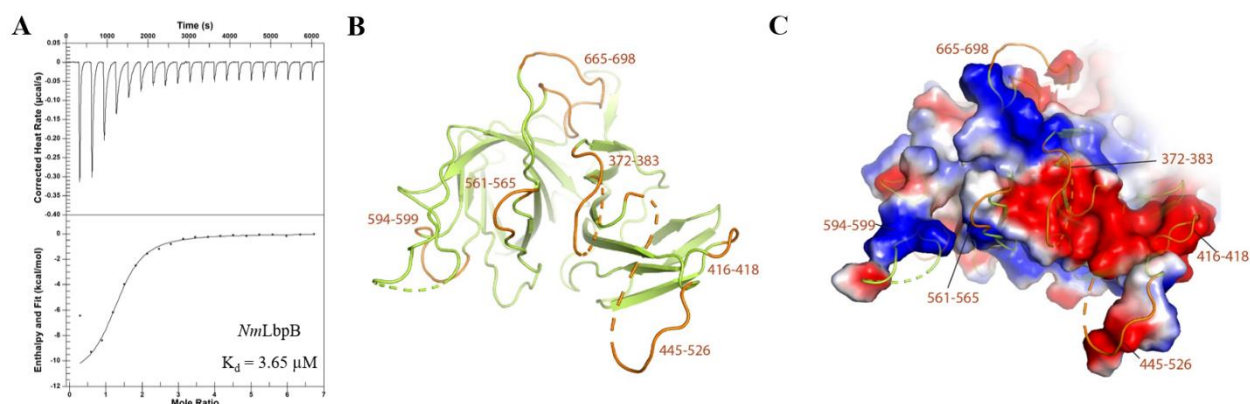


Figure 3.1. Lfcn binding to NmLbpB. (A) ITC raw data (top) and isotherm (bottom) for Lfcn titration with NmLbpB. Putative Lfcn binding site in NmLbpB shown in cartoon (B) and electrostatic potential surface (C). The surface exposed loops are colored orange. As some of these loops are missing from the structure, an accurate electrostatic potential surface couldn't be created. However, the resolved structure clearly shows a large patch of anionic surface that can accommodate Lfcn binding.

type (Figure 3.2 and Table 3.2). Most of the single loop deletions including $\Delta 372-383$, $\Delta 416-418$, $\Delta 561-565$, $\Delta 594-599$, and $\Delta 665-698$ did not have any significant effect on Lfcn binding. However, $\Delta 445-526$ showed ~ 2.5 -fold increase in K_d ($9.1 \mu\text{M}$) but a similar ΔH value (-9.6 kcal/mol) (Figure 3.2C).

Table 3.2. Summary of ITC data showing thermodynamic parameters for Lfcn titrations with wild-type and loop-deletion mutants of NmLbpB. ΔH , enthalpy change; K_d , dissociation constant, and ΔS , entropy change.

Construct	ΔH (kcal/mol)	K_d (μM)	n	ΔS (cal/mol.K)
Wild type	-11.44 ± 0.484	3.65	1.251 ± 0.036	-15.51
$\Delta 372-383$	-9.926 ± 0.979	4.94	1.372 ± 0.105	-10.77
$\Delta 416-418$	-9.082 ± 0.618	5.90	1.591 ± 0.083	-8.15
$\Delta 445-526$	-9.615 ± 2.013	9.07	0.926 ± 0.146	-10.89
$\Delta 561-565$	-10.11 ± 0.535	4.15	1.317 ± 0.042	-11.09
$\Delta 594-599$	-9.713 ± 0.751	4.78	1.584 ± 0.076	-9.96
$\Delta 665-698$	-10.72 ± 0.699	5.56	1.537 ± 0.071	-13.81
$\Delta 445-526_ \Delta 665-698$	Insufficient binding			

As mentioned above, $\Delta 445-526$ and $\Delta 665-698$ contain the largest patches of charged residues and have been shown to be important for NmLbpB's function in the protection against

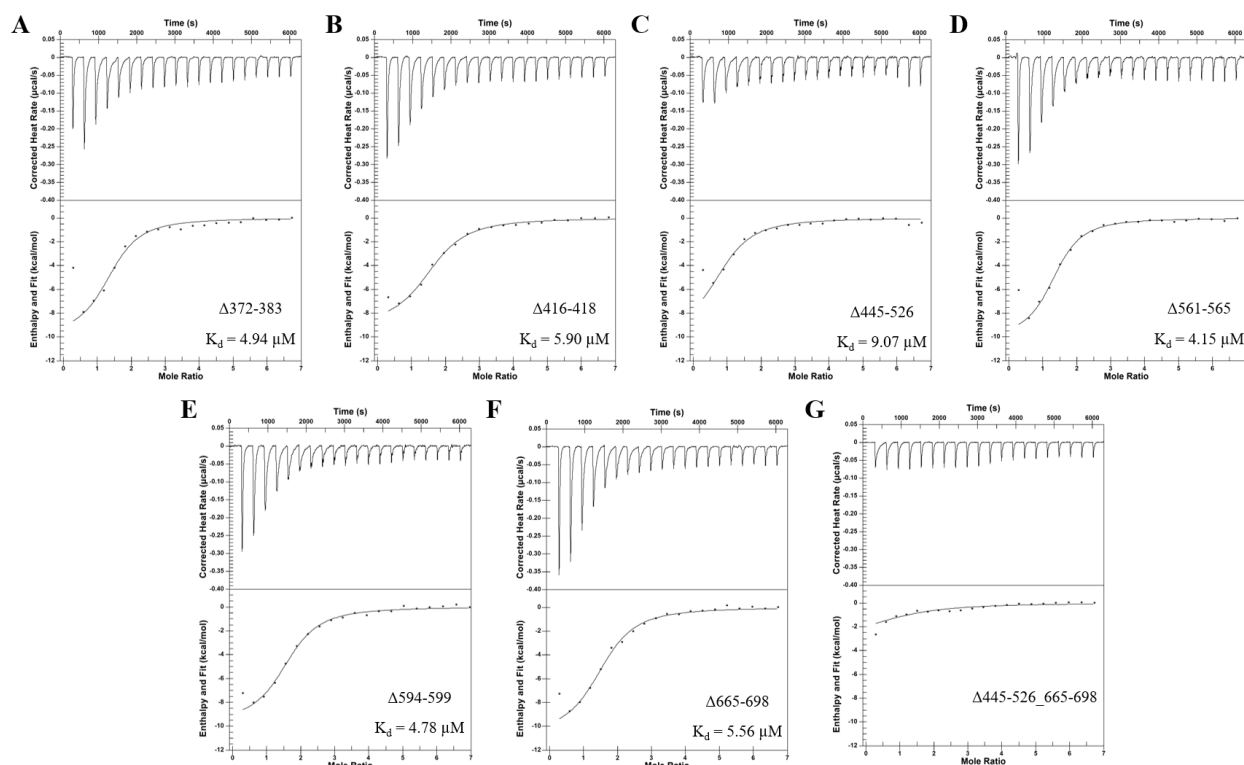


Figure 3.2. Probing the putative Lfcn binding site of *NmLbpB*. ITC raw data (top) and isotherm (bottom) for Lfcn titration with *NmLbpB* mutants. Single loop deletions do not have significant effect on Lfcn binding (A-F), however double loop deletion mutant $\Delta 445-526_665-698$ significantly reduces Lfcn binding (G).

Lfcn¹⁴⁵. Although individual deletions of these loops did not affect Lfcn binding, we hypothesized that the combination of these two loops may contribute to Lfcn's binding to LbpB. Therefore, to test this, we created a double loop-deletion mutant $\Delta 445-526_665-698$ and evaluated its ability to bind to Lfcn. This mutant showed a significant decrease in Lfcn binding, as shown through the ΔH differences between the wild-type and mutant *NmLbpB* (**Figure 3.2G and Table 3.2**). These studies confirm that anionic loops 445-526 and 665-698 contribute significantly to Lfcn binding and likely help form the putative binding site in LbpB.

3.4.2 Lfcn binds to LbpB at a site distinct from lactoferrin

The *NmLbpB*-lactoferrin crystal structure showed that lactoferrin binds to the N-lobe of *NmLbpB* (Chapter 2). As mentioned above, LbpB binds to Lfcn through anionic loops that are located in the C-lobe. These observations suggested that lactoferrin and Lfcn have distinct binding sites on *NmLbpB*. Therefore, we evaluated the effect of Lfcn binding to *NmLbpB* in the presence

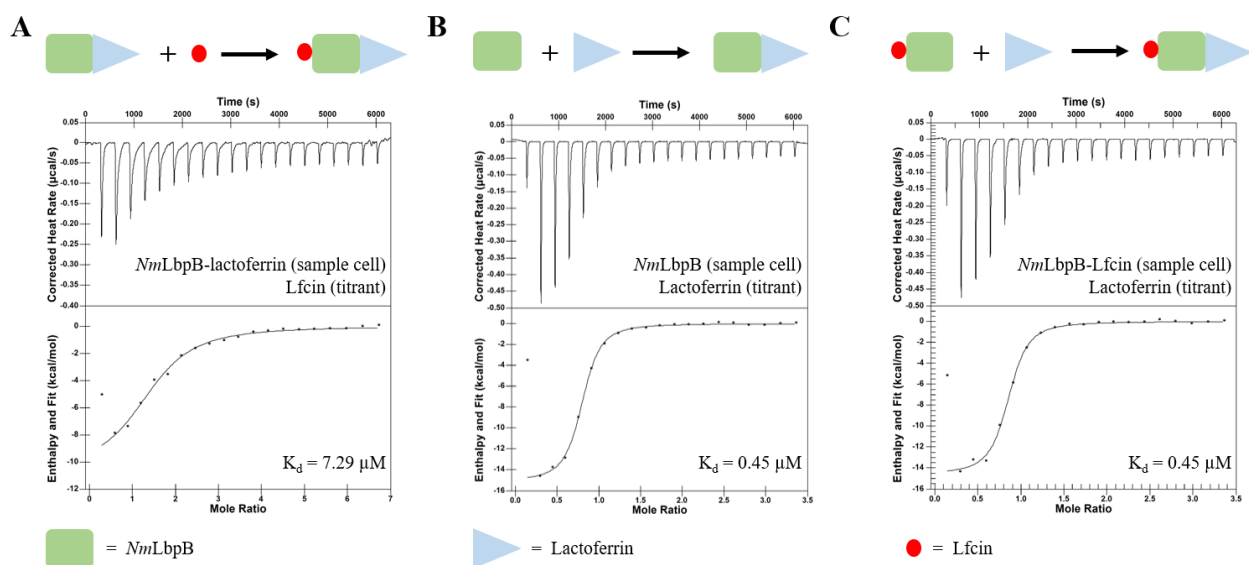


Figure 3.3. *NmLbpB* binds to both lactoferrin and LfcN independently. ITC raw data (top) and isotherm (bottom) for LfcN titration with *NmLbpB*-lactoferrin complex (A) and lactoferrin titration with *NmLbpB* in absence (B) and presence (C) of LfcN. A schematic for the titration experiment is shown on top of each panel. Presence of lactoferrin does not interfere with LfcN binding to *NmLbpB* and vice-versa.

of lactoferrin using ITC. LfcN binds to the *NmLbpB*-lactoferrin complex with K_d and ΔH values of $7.3 \mu\text{M}$ and -10.6 kcal/mol , respectively (**Figure 3.3A**). These values are highly similar to LfcN binding to *NmLbpB* alone, suggesting LfcN binding is not affected by the presence of lactoferrin.

We also examined the lactoferrin binding to *NmLbpB* in the absence and presence of LfcN (**Figure 3.3B and C; and Table 3.3**). Lactoferrin binds to *NmLbpB* with a K_d of $0.451 \mu\text{M}$. To test the lactoferrin binding to *NmLbpB* in presence of LfcN, we formed the *NmLbpB*-LfcN complex and purified it using SEC. An almost identical K_d ($0.454 \mu\text{M}$) was observed for lactoferrin binding to the *NmLbpB*-LfcN complex. Moreover, no change in ΔH values was detected for lactoferrin binding in the absence or presence of LfcN. Taken together, our binding studies indicate that LfcN and lactoferrin bind independently to *NmLbpB* at non-overlapping sites.

Table 3.3. Summary of thermodynamic parameters for lactoferrin and LfcN titrations with *NmLbpB*. These parameters were obtained using a Nano ITC calorimeter (TA Instruments).

Lactoferrin titration				
Constructs	ΔH (kcal/mol)	K_d (μM)	n	ΔS
<i>NmLbpB</i>	-15.11 ± 0.275	0.451	0.739 ± 0.008	-21.65
<i>NmLbpB</i> -LfcN	-14.62 ± 0.425	0.454	0.795 ± 0.014	-20.01
LfcN titration				
<i>NmLbpB</i> -lactoferrin	-10.61 ± 1.262	7.286	1.412 ± 0.110	-13.96

3.4.3 Lfcn binding induces conformational changes in LbpB

In the *NmLbpB*-lactoferrin complex crystal structure, the C-lobe has a higher B-factor compared to the rest of the structure. Whereas the anionic loops are missing altogether, thereby suggesting a high flexibility in these regions (**Chapter 2**). Our binding studies showed that Lfcn

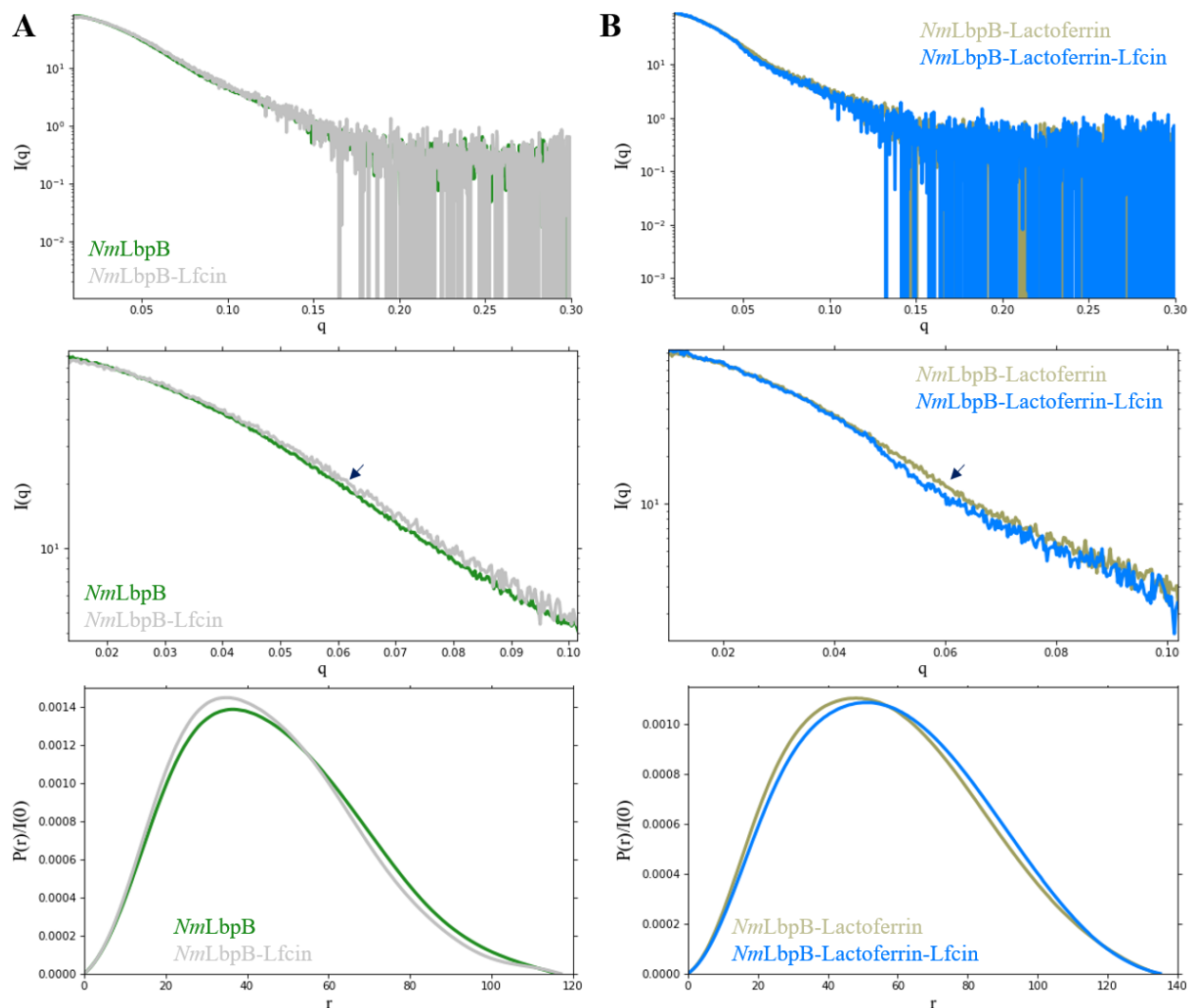


Figure 3.4. SEC-SAXS characterization of *NmLbpB*-Lfcn complex. Comparison of SEC-SAXS scattering profile (top panel) and zoomed view of low q -range (middle panel) and pair-distance distribution function $P(r)$ (bottom panel) of *NmLbpB* alone (green) with *NmLbpB*-Lfcn complex (grey) (A) and *NmLbpB*-lactoferrin alone (olive) and in complex with Lfcn (blue) (B). The black arrow points to the differences in the scattering profile at low q -range (0.05 - 0.08) (middle panel). The SEC-SAXS analysis showed that Lfcn binding induces small conformational change in *NmLbpB*.

binds to the anionic loops of LbpB. Therefore, we hypothesized that Lfcn binding might induce a conformational change in LbpB. We performed SEC-SAXS studies to calculate the solution scattering and pair-distance distribution function $P(r)$ of *NmLbpB* in the absence and presence of

Lfcn (**Figure 3.4A**). Comparison of the scattering profile showed that Lfcn binding produces a small change in the lower q range (**Figure 3.4A, top and middle panel**). This difference was also reflected in the $P(r)$ curve (**Figure 3.4A, bottom panel**). Although the R_g and D_{max} values were almost identical, differences in the curve suggested local conformational changes that were induced by Lfcn binding. Additionally, similar differences in the lower q -range in the scattering profile and $P(r)$ curve were detected for the *NmLbpB*-lactoferrin complex in presence of Lfcn (**Figure 3.4B**). Thus, these data show that lactoferrin and Lfcn can bind to *NmLbpB* simultaneously, albeit at distinct binding sites.

3.4.4 Using Fabs as chaperones to determine the LbpB-Lfcn structure

To understand the structural basis of Lfcn binding to LbpB, we obtained the structure of *NmLbpB*-lactoferrin co-crystallized with Lfcn. However, the C-lobe was still disordered, and thus no density for the bound Lfcn was observed. As described above, Lfcn binds to anionic loops in the C-lobe. Therefore, we focused our efforts on crystallizing the C-lobe with Lfcn. We used Fab fragments to stabilize and aid in the crystallization of the C-lobe-Lfcn complex as described below.

To facilitate phage display library screening, an Avi-tagged *NmLbpB* C-lobe was biotinylated using the BirA ligase enzyme. Biotinylated protein was cleaned up over SEC, pooled

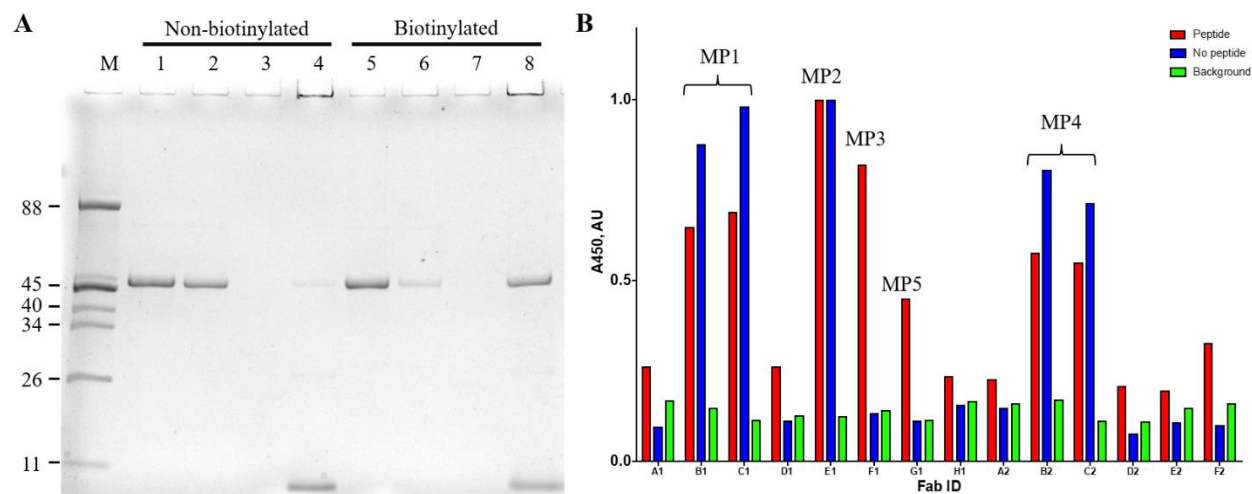


Figure 3.5. Phage-display Fab screening. (A) Streptavidin pull-down to assess the biotinylation efficiency of *NmLbpB* C-lobe biotinylation. M - marker; 1 - non-biotinylated protein; 2 - unbound; 3 - wash; 4 - final (strep beads); 5 - biotinylated protein; 6 - unbound; 7 - wash; and 8 - final (strep beads). (B) Single-point ELISA assay to assess the unique binders against buffer (background, green), biotinylated *NmLbpB* C-lobe in absence (no peptide, blue) and presence (peptide, red) of Lfcn. The unique binders with sufficient signal labelled MP1-5 were selected for further characterization.

Table 3.4. Summary of complementarity-determining regions (CDRs) of Fabs identified through phage-display selection against biotinylated *NmLbpB* C-lobe.

Fab ID	Complementarity-determining regions (CDRs)			
	L3	HC1	HC2	HC3
MP1	SYWSLI	FYSSSI	YISSYSGSTY	EEQRYEQYGYAL
MP2	YKYTLV	VSSSYI	SIYSYYGSTS	MAPYYYTWGAGM
MP3	RVWGKLI	FSYSSI	SISSYYGSTY	NKGYYLYSFYYSYGAM
MP4	SSSSLI	FSSSSI	SISSSSGSTS	SFQWHMSQYYPTFTLWGF
MP5	SSSSLI	VYSSSI	YISPSSGSTY	PNGYPWYYSLVPYQGM

together and concentrated. C-lobe biotinylation was confirmed using streptavidin pull-down. Non-biotinylated Avi-tagged *NmLbpB* C-lobe was used as a control. As shown in **Figure 3.5A**, non-biotinylated C-lobe was present in the flow-through/unbound fraction, and no bound protein was observed in the washed beads, whereas biotinylated Avi-tagged *NmLbpB* C-lobe binds to the streptavidin beads and was present in the washed beads. The biotinylated C-lobe was then used for biopanning for Fab selection.

To stabilize the C-lobe for structural studies, Fabs were screened from a phage-display library to serve as crystallization chaperones. The Fab selection was performed in the presence of Lfcn to select binders that specifically stabilize the Lfcn-bound conformation of the C-lobe. After four rounds of stringent selection, several unique binders were obtained. The unique binders were evaluated using single-point phage ELISA in the absence or presence of Lfcn with biotinylated C-lobe. Several Fab fragments displayed differential binding relative to the presence or absence of Lfcn (**Figure 3.5B**). A total of 5 Fab fragments, labelled MP1-5, were selected for further structural studies. The complementarity determining regions (CDRs) of these Fab fragments are listed in **Table 3.4**.

The C-lobe-Lfcn-Fab complexes were purified and crystallized. The C-lobe-Lfcn crystals were obtained with four different Fabs, MP1, MP2, MP4, and MP5. The crystals with Fab MP1 and MP2 diffracted to sub 4 Å resolution, whereas MP4 and MP5 containing crystals only diffracted to ~9 Å. Despite optimization of several different crystal conditions, no improvement in diffraction for MP4 and MP5 Fab containing crystals was observed. Here, we summarize the structures of the C-lobe-Lfcn in complex with MP1 and MP2.

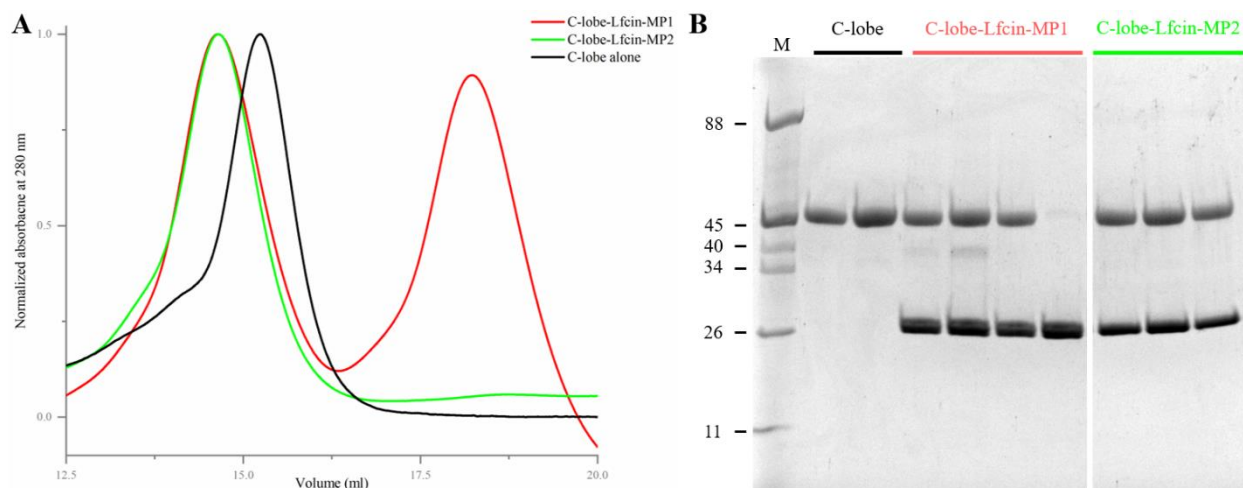


Figure 3.6. Purification of the *NmLbpB* C-lobe in complex with Lfcn and Fab fragments. (A) SEC chromatographs of C-lobe alone (black), C-lobe in complex with Lfcn and MP1 (red), and C-lobe in complex with Lfcn and MP2 (green) purification. The elution peak shows a leftward shift in presence of Fab fragments suggesting complex formation. (D) SDS-PAGE analysis of elution peaks from panel C shows co-elution of Fabs with C-lobe.

The C-lobe-Lfcn-MP1 complex was formed by sequential incubation of the C-lobe with Lfcn and MP1. Excess Lfcn and MP1 were removed by injecting the incubation mixture over SEC. The leftward shift in the peak suggested complex formation (**Figure 3.6A**). SDS-PAGE analysis showed that both C-lobe and MP1 are present in the peak fractions (**Figure 3.6B**). Additionally, a second peak was observed corresponding to excess MP1. The C-lobe-Lfcn-MP1 fractions were pooled, concentrated, and used for crystallization screening. Crystals were harvested, and the diffraction data to 3.55 Å resolution were collected. The structure was solved using molecular replacement in space group $P2_12_12_1$ with three C-lobe-Lfcn-MP1 complexes per asymmetric unit. All three complexes are almost identical with respect to each other (**Figure 3.7A**). Both heavy and light chains of MP1 can be modelled in the electron density. The MP1 interacts with the handle domain of the C-lobe (**Figure 3.7B**). In the structure, no density for the C-lobe anionic loops or Lfcn was observed.

The C-lobe-Lfcn-MP2 complex was formed, purified, and crystallized using the same procedure as the C-lobe-Lfcn-MP1 complex (**Figure 3.6**). The C-lobe-Lfcn-MP2 crystal diffracted at 3.7 Å resolution, and the structure was solved in space group $I2_12_12_1$. There were two complexes per asymmetric unit. Both complexes are almost identical (root mean square deviation (RMSD) of 0.683 Å over 404 C_α atoms) (**Figure 3.8A**). The MP2 primarily interacts with the surface exposed

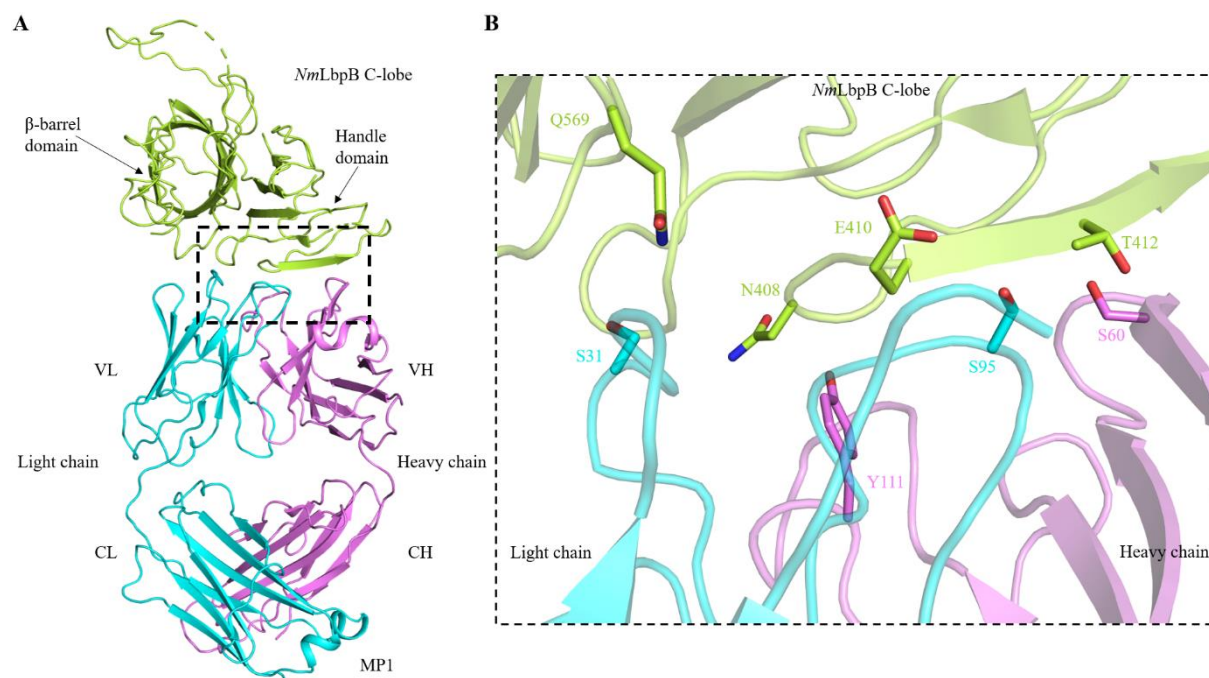


Figure 3.7. The crystal structure of *NmLbpB* C-lobe-Lfcn-MP1 complex. (A) The asymmetric unit contains three C-lobe-Lfcn-MP1 complexes. For clarity, one complex between C-lobe (green) and MP1 (light chain – cyan, heavy chain – magenta) is shown. MP1 primarily binds with handle domain of C-lobe (dashed box). (B) Zoomed view of C-lobe - MP1 binding interface. The interface residues are shown in stick with same color scheme as panel A.

loops of the β -barrel domain (**Figure 3.8B**). Like the C-lobe-Lfcn-MP1 crystal structure, no electron density for anionic loops or Lfcn was observed.

3.5 Discussion and conclusion

LbpB plays dual functions in *Neisseria*: iron import and protection against the host cationic antimicrobial peptide Lfcn. Crystal and cryo-electron microscopy structures of *NmLbpB* and *NgLbpB* in complex with lactoferrin, respectively, showed that the N-lobe of LbpB binds to lactoferrin. In the current study, we show that Lfcn binds to LbpB with a low μM affinity at a binding site formed by flexible anionic loops 445-526 and 665-698. Our SEC-SAXS studies showed that Lfcn binding induces local conformational change in LbpB (**Figure 3.4**). Also, the presence of Lfcn shows similar differences in the scattering profile of *NmLbpB*-lactoferrin at a lower q -range. Our binding studies showed that Lfcn binds to the *NmLbpB*-lactoferrin complex with similar affinity as *NmLbpB* alone and *vice versa*.

To facilitate crystallization, five Fab fragments were identified using phage display screening against the *NmLbpB* C-lobe in the presence of Lfcn. Out of these, four Fab fragments were crystallized with the C-lobe-Lfcn complex. Additionally, we solved the crystal structure of Fabs MP1 and MP2 bound to the C-lobe-Lfcn complex. These Fabs primarily bind at different domains of the C-lobe, with a small overlap at the binding site (**Figure 3.9**). Even though these Fab fragments enabled the crystallization and subsequent structure determination, no electron density was observed for the anionic loops or Lfcn. Therefore, further studies are required to resolve the Lfcn bound anionic loop conformation.

Based on our SEC-SAXS and binding studies, we propose that LbpB performs dual functions in mediating Neisserial pathogenesis (**Figure 3.10**). The LbpB N-lobe binds to holo-

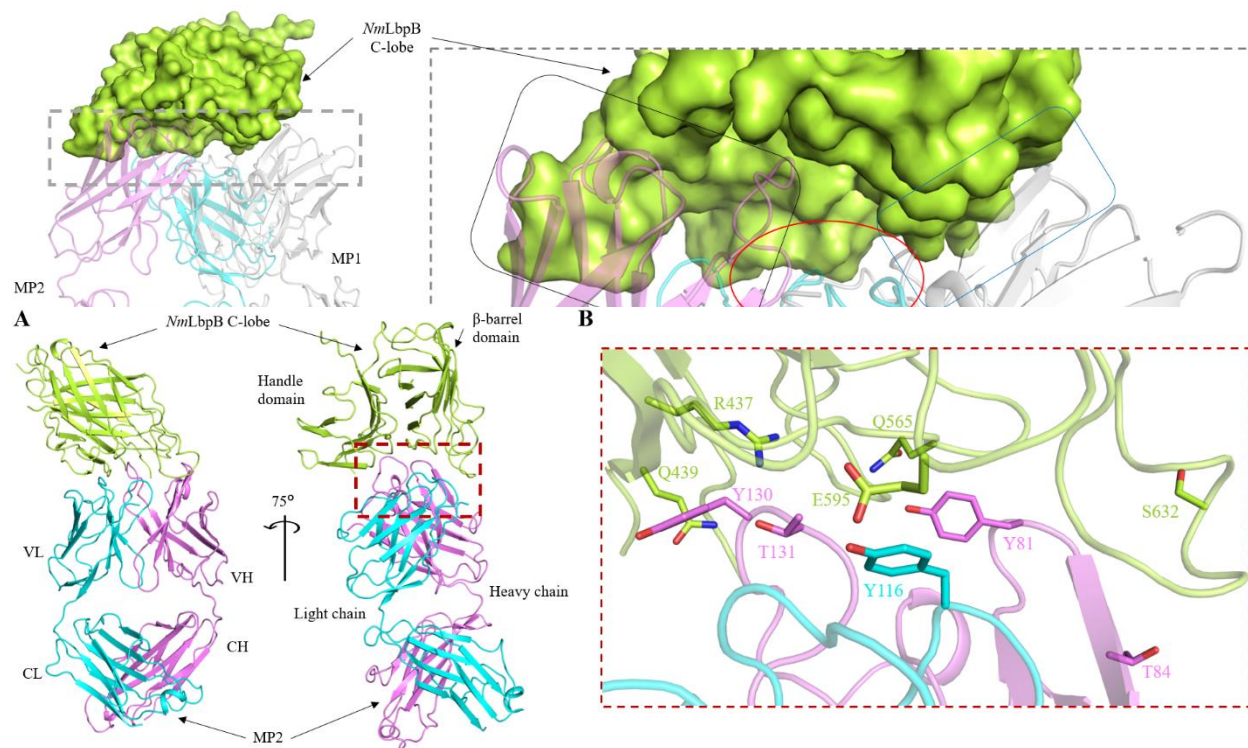


Figure 3.8. The crystal structure of *NmLbpB* C-lobe-Lfcn-MP2 complex. (A) The asymmetric unit contains two C-lobe-Lfcn-MP2 complexes. For clarity, one complex between C-lobe (green) and MP2 (light chain – cyan, heavy chain – magenta) is shown. MP2 primarily binds with β -barrel domain of C-lobe (dashed box). (B) Zoomed view of C-lobe - MP2 binding interface. The interface residues are shown in stick with same color scheme as panel A.

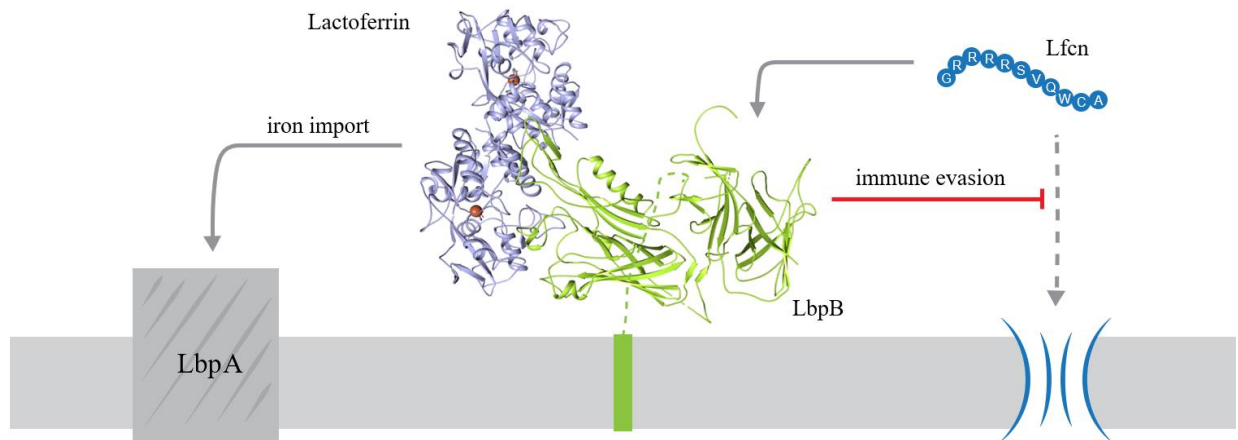


Figure 3.12. A model for the dual functions of LbpB. We propose that LbpB binds to lactoferrin through its N-lobe and shuttles the iron-bound lactoferrin to LbpA for iron extraction. Simultaneously, anionic loops in the C-lobe of LbpB sequester Lfcn peptide and neutralize its antimicrobial effects, thus protecting the bacteria from innate immune defense system.

lactoferrin and traps it in an iron-bound closed conformation for delivery to LbpA for iron import. Simultaneously, at the bacterial surface, the LbpB C-lobe binds to Lfcn to protect the pathogen from Lfcn's antimicrobial effect, which would normally kill the bacteria. Specifically, upon release from the bacterial surface by the NalP autotransporter, LbpB can diffuse in the host environment at the site of infection and sequester Lfcn. Our studies show that LbpB and Lfcn directly interact through the C-lobe anionic loops, however, further studies are still required to determine the structure of Lfcn bound to LbpB.

CHAPTER 4. STRUCTURAL INSIGHT INTO IRON EXTRACTION FROM LACTOFERRIN BY LBPA IN *NEISSERIA*

4.1 Abstract

Neisseria utilize outer membrane proteins (OMPs) to sequester iron from host proteins. These OMPs bind to host proteins and extract iron from them, which is subsequently transported across the membrane. Lactoferrin binding protein A (LbpA) is a TonB-dependent transporter that binds to human lactoferrin. Understanding the molecular mechanism of LbpA's function has been limited by a lack of structural and functional studies. Here, we determined the 4.1 Å cryo-electron microscopy structure of Nme LbpA (*NmLbpA*) in complex with human lactoferrin. Like other known TonB-dependent transporters, *NmLbpA* contains a 22-strand β -barrel occluded by the N-terminus plug domain. *NmLbpA* has long extracellular loops that bind to the C-lobe of lactoferrin. In the *NmLbpA*-lactoferrin, the C-lobe of lactoferrin is in an intermediate open-conformation. We propose that LbpA binding to lactoferrin is sufficient for iron extraction, whereas TonB is required for iron transport across the membrane. These observations provide structural insights into lactoferrin recognition by LbpA, as well as lay a framework for understanding the molecular mechanism of LbpA-mediated iron piracy.

4.2 Introduction

Lactoferrin binding protein A (LbpA) is a TonB-dependent transporter present in the outer membrane of *Neisseria* that extracts iron from human lactoferrin and transports it across the membrane¹³⁷. LbpA is expressed in all meningococcal strains and ~50% of gonococcal strains^{40,133}. LbpA shows selectivity towards human lactoferrin over other human iron carrier proteins such as transferrin and hemoglobin, and over bovine lactoferrin⁷⁹. However, it doesn't distinguish between apo- or holo- forms of human lactoferrin⁷⁹. The LbpA iron import process is enhanced in the presence of lactoferrin binding protein B (LbpB)¹³⁶.

Based on the homology between LbpA and TbpA, similar structural and mechanistic models for LbpA iron acquisition have been proposed¹³⁷. Solid-phase binding assays of LbpA with chimeric lactoferrin showed that both the C1 and C2 subdomains of lactoferrin C-lobe bind to LbpA¹³⁵. However, given the higher affinity of lactoferrin towards iron as compared to transferrin,

and the local differences in the transferrin and lactoferrin residues near TbpA/LbpA binding site, the exact mechanism of iron acquisition from lactoferrin couldn't be deduced. Therefore, to gain structural insight into lactoferrin binding to LbpA, we determined the cryo-EM structure of *NmLbpA* in complex with human lactoferrin at 4.2 Å resolution. *NmLbpA* binds to the C-lobe of lactoferrin at a site distinct from the LbpB binding site. Interestingly, upon *NmLbpA* binding, the lactoferrin C-lobe undergoes a conformational change to release iron, whereas the N-lobe iron remains intact with the domain still in a closed conformation. The structure provides interesting details into iron extraction from lactoferrin by LbpA in the absence of LbpB and TonB.

4.3 Methods

4.3.1 Construct design and cloning

The codon optimized *lbpA* gene from *Nme* MC58 was obtained from Bio Basic. The gene fragment encoding residues 28-943 was amplified using polymerase chain reaction (PCR) using forward (CAATGGATATCGGTGGTGCCACCCCTGATGCAGCAC) and reverse primers (GTATCCTCGAGTTAGAATTTTCATTTCCAGGGCCAG) for membrane expression. The amplified fragments were purified and digested with restriction enzymes, EcoRV-HF and XhoI, followed by ligation into digested pET20bHT¹⁹³ vector. The ligated plasmid was transformed into DH5α cells and grown overnight on Luria Broth (LB) agar plates containing 100 µg/mL carbenicillin antibiotic. Single colonies were picked, grown overnight in 2XYT medium, and plasmids were isolated. The gene insertion into the plasmid was confirmed by sequencing.

4.3.2 Protein expression and purification

For protein expression, the pET20bHT plasmid containing *NmLbpA* was transformed in C43(DE3) cells. A single colony was picked up and grown in 2XYT medium supplemented with 50 µg/mL ampicillin at 37°C for overnight. This inoculate culture was transferred to 500 mL Terrific Broth (TB) medium supplemented with 50 µg/mL ampicillin and grown at 37°C while shaking at 180 rpm till optical density 600 (OD₆₀₀) reached 0.5-0.6. The shaker temperature was reduced to 24°C and protein was induced by addition of 0.4 mM isopropyl β-D-thiogalactopyranoside (IPTG). Cells were harvested 12 hours post induction by centrifugation at 6,000 rpm and cells were stored at -80°C until further use.

For protein purification, cells were resuspended in chilled 1x PBS buffer (8 mM Na₂HPO₄, 2 mM KH₂PO₄, 137 mM NaCl, 2.7 mM KCl) supplemented with 10 µg/mL DNaseI and 0.4 mM phenylmethylsulfonyl fluoride (PMSF). Cells were lysed by three passages through Emulsiflex C3 high pressure homogenizer (Avestin) at 15,000 - 18,000 psi. Large cellular debris were removed by centrifugation at 6,000 x g for 20 minutes at 4°C. Supernatant was collected and incubated with 2% triton X-100 for 30 minutes at room temperature while stirring for solubilizing inner membranes. Subsequently, the outer membranes were pelleted using a Type 45 Ti rotor (Beckman Coulter) in an Optima XPN-90 ultracentrifuge (Beckman Coulter) at 200,000 x g for 90 minutes at 4°C. The pelleted membranes were collected and solubilized by stirring in solubilization buffer (1xPBS, 5 % Elugent, 50 mM imidazole) for 12 hours at 4°C. Subsequently, the non-solubilized membranes were separated by ultracentrifugation at 200,000 x g for 60 minutes at 4°C. The supernatant was collected and used for affinity purification.

Affinity purification was performed using 5 mL Hi-Trap affinity column containing Ni-NTA resin (Qiagen). The column was equilibrated with Buffer A (1xPBS + 50 mM imidazole + 0.05 % n-Dodecyl-β-D-Maltoside (DDM)). The ultracentrifugation supernatant containing the solubilized proteins was passed through the column. The column was washed with 50 mL Buffer A and 20 mL Wash buffer (1xPBS + 100 mM imidazole + 0.05 % DDM). The protein was then eluted in elution buffer (1xPBS + 250 mM imidazole + 0.05 % DDM). Fractions containing *NmLbpA* were pooled and concentrated for further use.

4.3.3 Formation of the *NmLbpA*-lactoferrin complex

Human holo-lactoferrin (obtained from Raybiotech Inc.) was reconstituted in 1xPBS + 0.05% DDM and purified by passage over a Superdex 200 Increase 10/300 GL column (Cytiva). Fractions containing lactoferrin were pooled together and concentrated. For complex formation, *NmLbpA* was incubated with 1.25x molar excess of lactoferrin for 1.5 hours on ice followed by size-exclusion chromatography (SEC) purification using a Superdex 200 Increase 10/300 GL column (Cytiva) for removal of excess lactoferrin. Fractions containing the *NmLbpA*-lactoferrin complex were pooled and concentrated. The complex was then detergent exchanged into 1x PBS + 0.01 % LMNG by SEC. Fractions containing the *NmLbpA*-lactoferrin complex were pooled and concentrated for cryo-EM studies.

4.3.4 Grid preparation and cryo-EM data collection

Quantifoil R 3.5/1 Cu 200 grids were glow discharged using a PELCO easiGLOW™ (TED PELLA, INC.) at 25 mA current and 0.26 mBar pressure for 1 minute with a 10 second hold. For vitrification, 2.5 μ L of *NmLbpA*-lactoferrin complex (2.5 mg/mL) was applied and incubated for 5 seconds at 4°C and 100% humidity. Subsequently, the grid was plunge frozen into liquid ethane using Vitrobot Mark IV (Thermo Fisher Scientific) by blotting for 1.5 second with blot force 2.

Cryo-EM data were collected on a Titan Krios G1 microscope (Thermo Fischer Scientific) equipped with a Gatan Quantum energy filter and a Gatan K3 direct electron detector using Leginon¹⁸². The movies were collected at 81,000x magnification with a 0.539 Å pixel size. Each movie was exposed for 3,120 ms with a total dose of 53.76 e⁻/Å² over 40 frames with a defocus range of -0.7 to -2 μ m. A single cryo-EM dataset of total 2645 movies was collected. The data collection parameters are summarized in **Table 4.1**. The data quality was monitored using cryoSPARC Live¹⁸³ in real time during data collection.

4.3.5 Cryo-EM data processing, model building, and refinement

The cryo-EM movies were dose-weighted, and motion corrected with MotionCor2¹⁸⁴ with a binning factor of 2, resulting in a pixel size of 1.08 Å. The images were then imported into cryoSPARC v3.2.0¹⁸³ for further image processing. The contrast transfer function (CTF) parameters were calculated using ‘Patch CTF estimation (multi)’. A total of 1,975,580 particles were picked, extracted, and subjected to 2D classification. After two rounds of iterative 2D classification, classes containing 490,256 particles were selected. The selected particles were subjected to multiple rounds of ab-initio reconstruction followed by heterogeneous refinement. Multi-class ab-initio reconstruction and heterogeneous refinement allow to filter junk particles from good particles. After each process, resulting maps were visualized in Chimera (**Reference**) to identify good classes for subsequent refinement. After 4 rounds of ab-initio reconstruction, heterogeneous, and non-uniform refinements, a final reconstruction at 4.31 Å was obtained. This map was subjected to local refinement to obtain a map at 4.2 Å. This map was used as template for particle picking and data was re-processed as described above to yield a final reconstruction with improved density in the transmembrane region of *NmLbpA*. The resolution was estimated using Gold-standard Fourier Shell Correlation (GSFSC) curve with 0.143 threshold as cut-off

criteria. The local refinement output map had an overall resolution of 4.1 Å. The data processing parameters are summarized in **Table 4.1**.

The resulting sharpened map from Local Refinement was used for model building and refinement. The map displayed defined secondary structure features, allowing for the identification of the protein boundaries and enabled model building. A homology model of *NmLbpA*¹³⁷ and

Table 4.1. Cryo-EM data collection, processing, refinement, and validation statistics for the *NmLbpA*-lactoferrin complex.

	<i>NmLbpA</i> -Lactoferrin
Data Collection and Processing	
Magnification	81,000
Voltage (kV)	300
Electron exposure (e ⁻ /Å ²)	53.76
Defocus range (μm)	-.07 to -2
Pixel size (Å)	0.54
Symmetry imposed	C1
Initial particle projections (no.)	1,975,580
Final particle projections (no.)	29,929
Map resolution (Å)	4.1
FSC threshold	0.143
Refinement	
Model Resolution (Å)	4.2
FSC threshold	0.5
Map-model CC	
CC_mask	0.86
CC_box	0.76
CC_peaks	0.64
CC_volume	0.86
Model Composition	
Non-hydrogen atoms	12432
Protein residues	1580
Ligands	4
B factors (Å²)	
Protein	122.72
Ligand	171.06
R.M.S. deviations	
Bond lengths (Å)	0.007
Bond angles (°)	0.862
Validation	
MolProbity Score	2.54
Clashscore	23.86
Poor rotamer (%)	0.77
Ramachandran Plot	
Favored (%)	84.45
Allowed (%)	15.23
Disallowed (%)	0.32

crystal structure of human lactoferrin (PDB ID: 2BJJ¹²⁴) were docked in the map using UCSF Chimera¹⁸⁶ and Coot¹⁷⁸ followed by real-space refinement of the model using Phenix¹⁹⁰. The

model was inspected residue-by-residue and adjusted based on the map. Iterative rounds of model building, and refinement were performed until a density consensus model was obtained. Model refinement and validation parameters are summarized in **Table 4.1**.

Protein-protein interfaces were analyzed using QtPISA¹⁸⁰ (Protein Interfaces, Surfaces and Assemblies) accessed through the CCP4 7.0¹⁸¹ software suite. Model visualization, analysis, and figure preparation were performed using PyMOL (Schrodinger LLC), Chimera¹⁸⁶ and ChimeraX¹⁸⁹.

4.4 Results

4.4.1 Purification of the *NmLbpA*-lactoferrin complex

LbpA is a TonB-dependent iron transporter that binds to human lactoferrin, extracts iron, and transports it across the membrane. However, the mechanistic understanding of LbpA's function remains elusive, primarily due to the absence of available structures of the individual components and of complexes. To understand the mechanism used by LbpA for iron piracy, we cloned the *NmLbpA* LbpA (residues 28-943) into the pET20bHT¹⁹³ plasmid for membrane expression. Optimal expression was achieved in C43(DE3) at 24°C for 12 hours. Cells were lysed and membrane fraction was obtained. The outer membranes were solubilized, and the protein was purified using immobilized metal affinity chromatography. Subsequently,

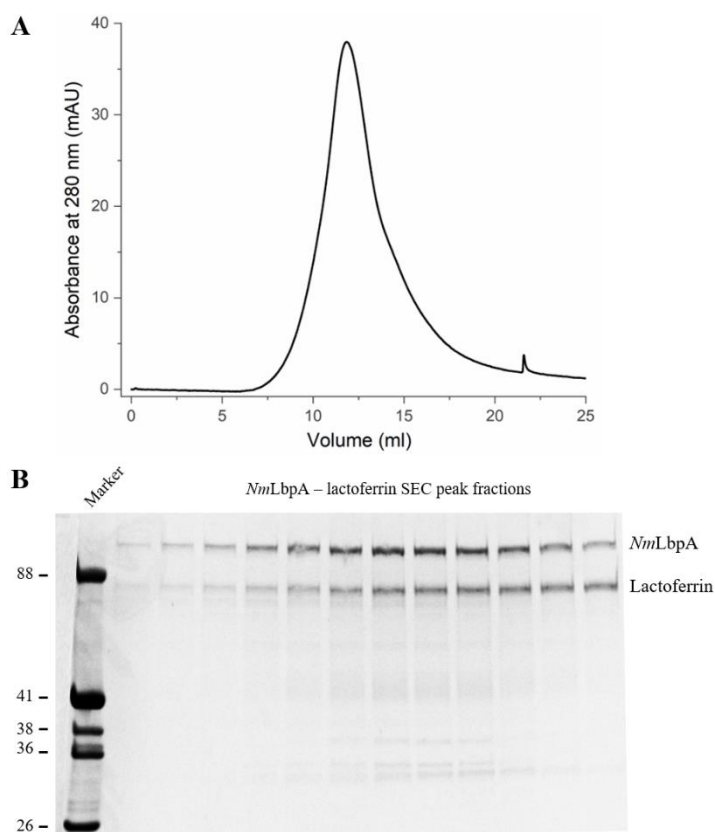


Figure 4.1. Formation of the *NmLbpA*-lactoferrin complex. (A) Size-exclusion chromatography (SEC) purification of *NmLbpA*-lactoferrin complex. (B) SDS-PAGE analysis of elution peak from panel A shows co-elution of *NmLbpA* and lactoferrin suggesting complex formation.

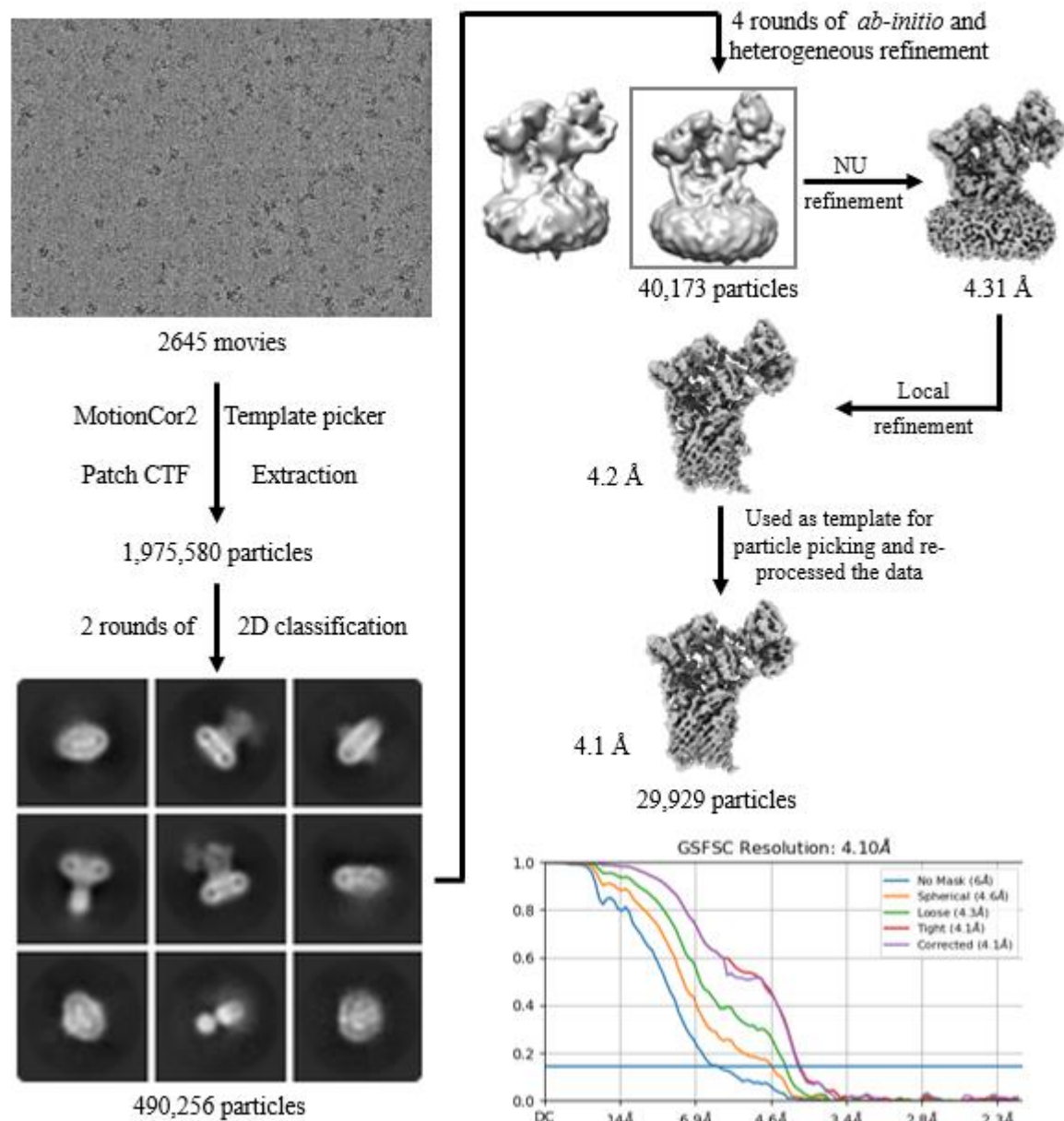


Figure 4.2: The cryo-EM data processing workflow for the *NmLbpA*-lactoferrin complex. Representative cryo-EM micrograph from 2645 movies. Beam induced motion was corrected and contrast transfer function (CTF) parameters were calculated. Particle were picked, extracted, and subjected to 2 rounds of 2D classification. Representative 2D class averages show different orientations of the particles. The selected particles were filtered through four rounds of *ab-initio* reconstructions followed by heterogeneous refinement. Boxed class was selected for further processing. Finally, a class containing 40,173 particles was subjected to non-uniform refinement and local refinement to obtain a map at 4.2 Å. This map was used as template for particle picking. Particles were extracted and processed to yield a final reconstruction at 4.1 Å. GSFSC curve of *NmLbpA*-Lactoferrin map with the horizontal blue line indicating 0.143 cutoff for resolution estimation.

NmLbpA-lactoferrin complex was formed by incubation on ice for 1.5 hours. Excess lactoferrin was removed by SEC runs (**Figure 4.1A**) and the peak fractions contained the complex as

demonstrated by SDS-PAGE (**Figure 4.1B**). The peak fractions were pooled together and used for further characterization.

4.4.2 The cryo-EM reconstruction of the *NmLbpA*-lactoferrin complex

To determine the *NmLbpA*-lactoferrin structure, cryo-EM data were collected using a Titan Krios G1 microscope equipped with a Gatan K3 direct electron detector. Data processing was performed as outlined in **Figure 4.2**. The 2D class averages displayed multiple views of protein

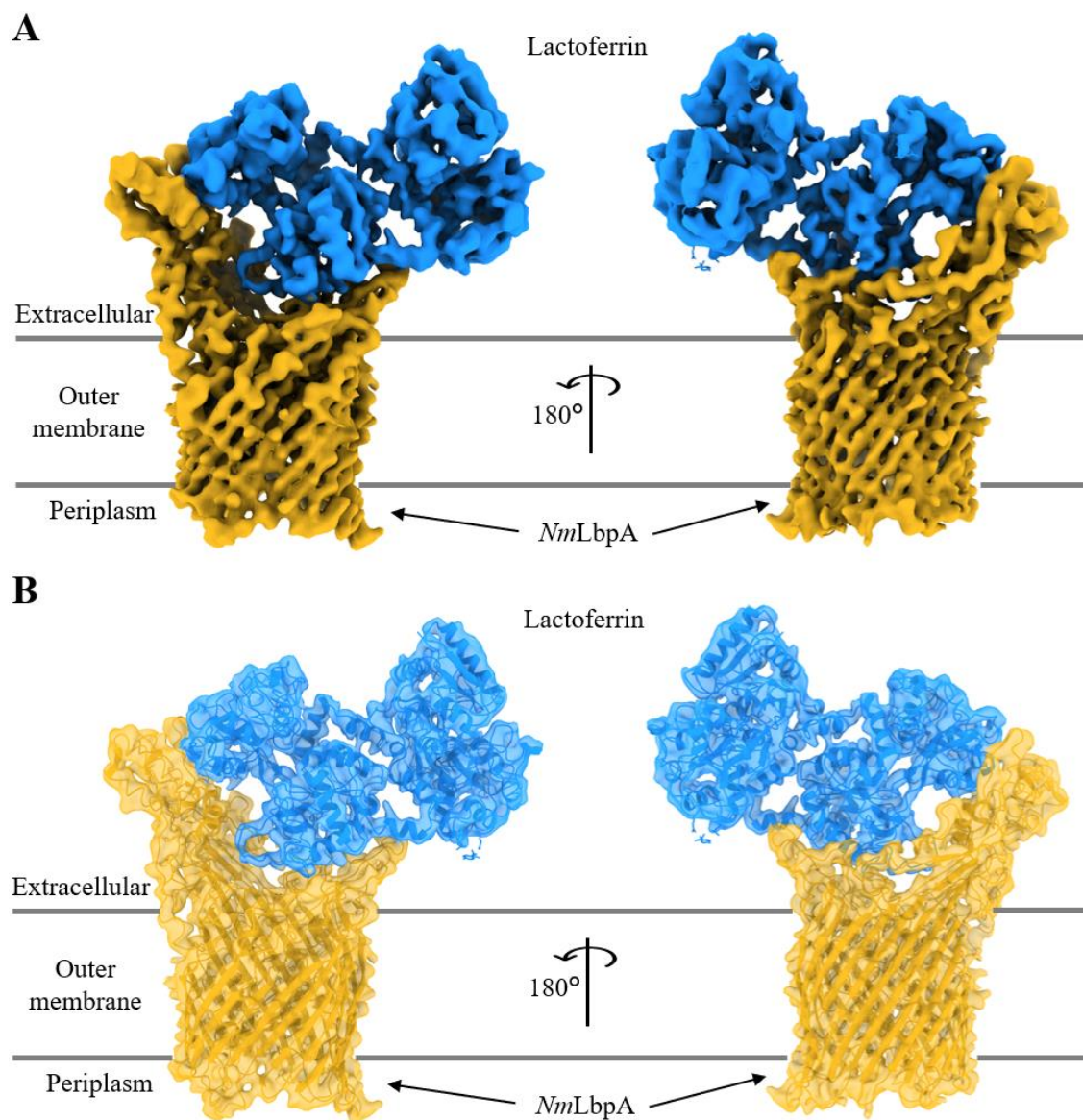


Figure 4.3. The cryo-EM map and model of *NmLbpA*-lactoferrin complex. Two different views of the cryo-EM map (A) and fitted model (B) of *NmLbpA* (orange) bound to lactoferrin (marine blue).

embedded into detergent micelle (**Figure 4.2**). The particles were processed through multiple rounds of *ab-initio* reconstruction, heterogeneous refinement, non-uniform refinement to filter junk particles. A final map was obtained by local refinement at 4.1 Å resolution with improved density in the transmembrane region (**Figure 4.2 and 4.3A**). The density map allowed identification of protein subunits. A model of *NmLbpA*-lactoferrin was created by fitting *NmLbpA* homology¹³⁷ model and holo-lactoferrin crystal structure (PDB ID: 2BJJ¹²⁴) (**Figure 4.3B**).

Subsequently, the entire model was iteratively adjusted in Coot¹⁷⁸ and refined using Phenix¹⁹⁰. The final atomic model contains residues 53-943 of *NmLbpA*, and residues 4-692 of lactoferrin. Validation of the model showed 84.45% and 15.23% of the residues were in favored and allowed regions on the Ramachandran plot, respectively, with 0.32% outliers. Additionally, one iron ion and one carbonate ion were also modelled. Refinement and validation parameters are summarized in **Table 4.1**.

4.4.3 The *NmLbpA*-lactoferrin structure

In the cryo-EM structure of the *NmLbpA*-lactoferrin complex, one *NmLbpA* interacts with one lactoferrin (**Figure 4.4**). The observation is consistent with the previous prediction that *NmLbpA* might bind to lactoferrin at a 1:1 molar ratio, much like what was observed for TbpA

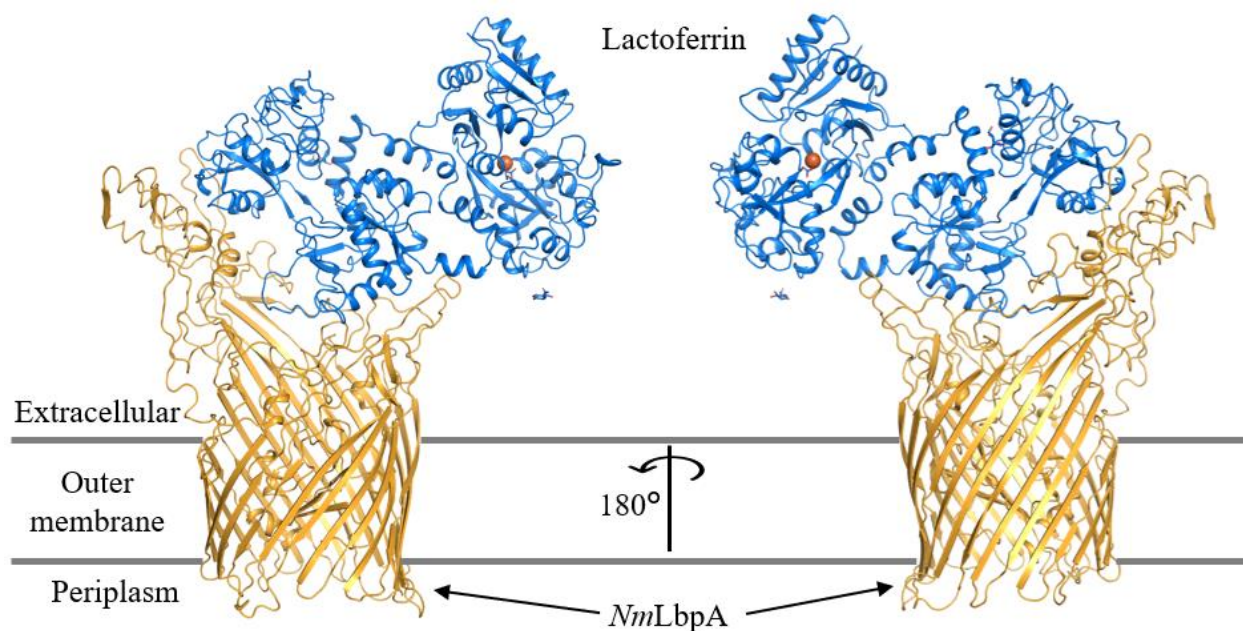


Figure 4.4. The structure of the *NmLbpA*-lactoferrin complex. *NmLbpA* (orange) binds to lactoferrin (marine blue) at the surface of the pathogen. The iron atom in the lactoferrin is shown as brown sphere.

and transferrin⁴³. The *NmLbpA* structure displays characteristic features of a typical TonB-dependent transporter, consisting of 22-strand transmembrane β -barrel (residues 190-943) occluded with amino-terminal plug domain (residues 1-189) (**Figure 4.5A**). The *NmLbpA* N-terminus was flexible and could not be resolved in the cryo-EM map. The plug domain structure consists of four strand β -sheets flanked by small α -helices and loops. A long loop between β -strand 2 and 3, termed plug loop, extends out of the barrel and is exposed to the extracellular environment. In the lumen of the β -barrel, this plug loop also contains the conserved EIEYE motif, which has been shown to be critical for iron import by TbpA¹¹⁵. The β -strands of the transmembrane barrel are connected through 11 small periplasmic and 11 large extracellular loops (ECLs). Some of these extracellular loops, namely loop 2, 3, and 5, extend ~ 60 Å above the bacterial surface to mediate lactoferrin binding.

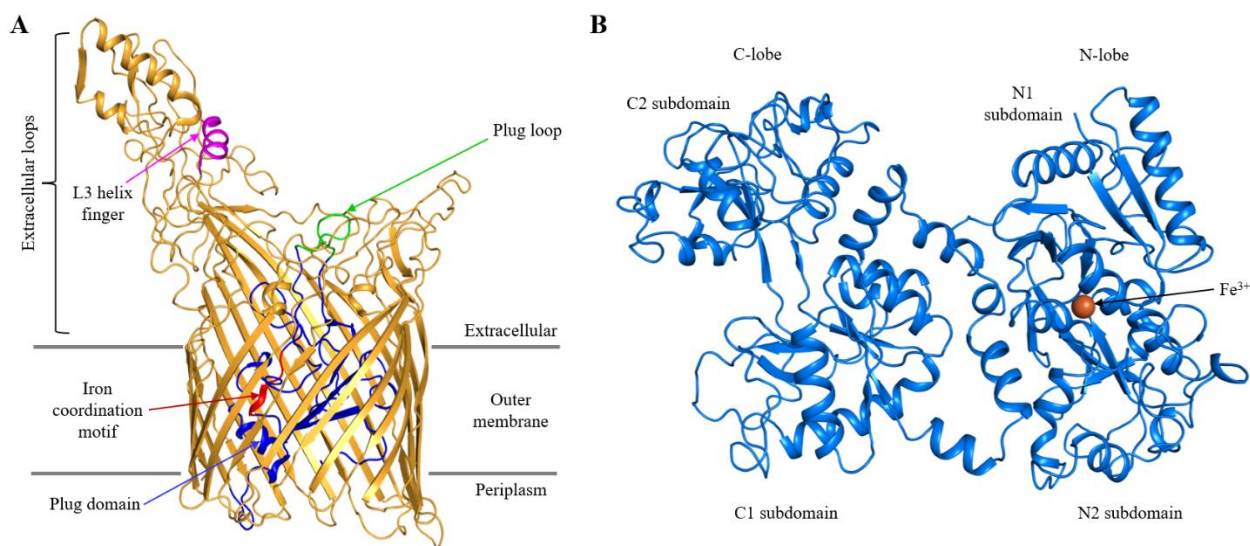


Figure 4.5. Structural features of the *NmLbpA*-lactoferrin complex. (A) *NmLbpA* is composed of an N-terminus plug domain (blue) and C-terminus 22-stranded β -barrel (orange). The plug domain contains a surface exposed loop termed plug loop (green) and an iron-coordination motif (red) in the lumen of the barrel. (B) Lactoferrin (blue) is composed of two lobes, N- and C-lobe. The N-lobe of lactoferrin contains an iron atom (red sphere).

Lactoferrin is composed of two lobes, N-lobe and C-lobe. The N-lobe contains an iron ion whereas C-lobe does not. In the *NmLbpA*-lactoferrin complex, *NmLbpA* interacts exclusively with C-lobe lactoferrin through an extensive binding interface formed by extracellular loops. The interaction interface is predominantly composed of polar interactions with a buried surface area of ~ 2371.4 Å². *NmLbpA* interacts with lactoferrin at three principal sites: (i) ECL2, 3, and 5 of *NmLbpA* to the C2 subdomain of lactoferrin, (ii) ECL5, 7, 8 and 10 of *NmLbpA* to the C1

subdomain of lactoferrin, and (iii) ECL3 of *NmLbpA* at the C1-C2 subdomain interface in lactoferrin (**Figure 4.6A**).

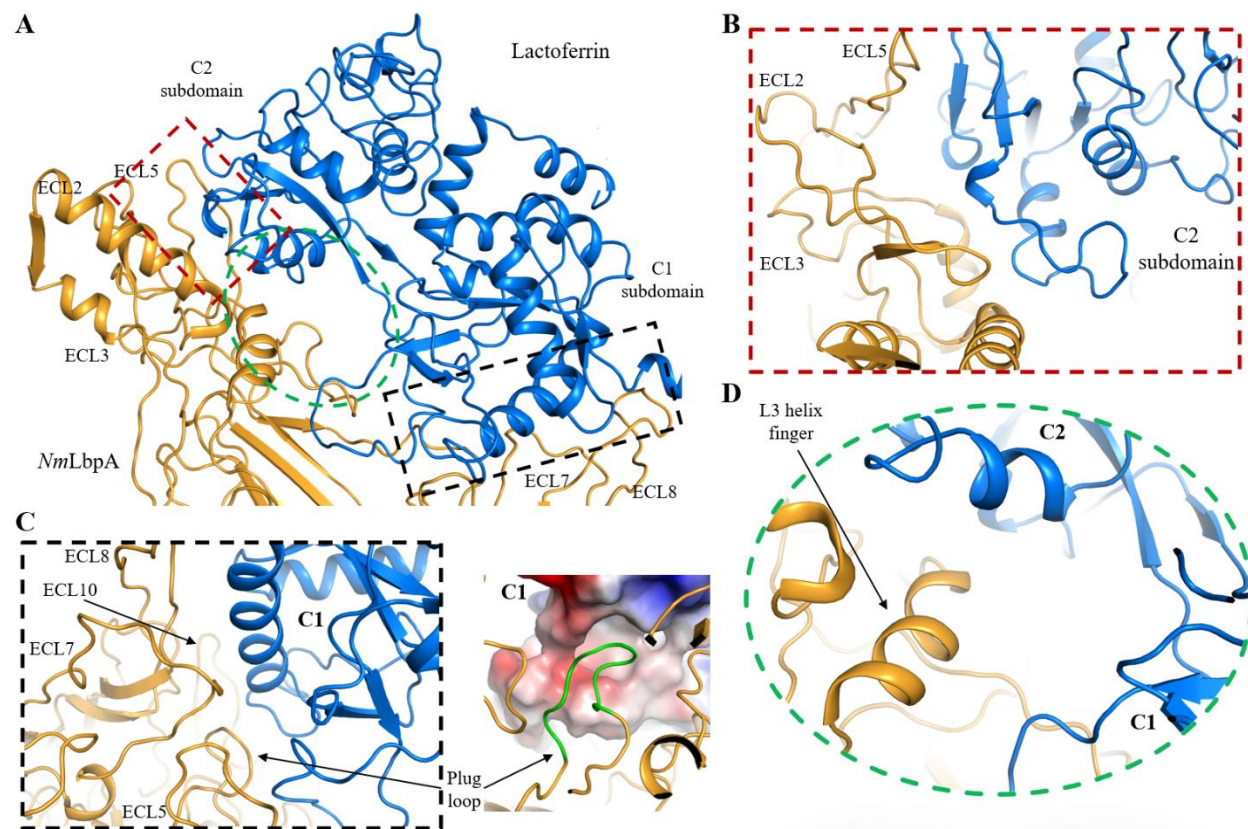


Figure 4.6. The *NmLbpA*-lactoferrin binding interface. (A) Lactoferrin C-lobe (marine blue) binds to an extensive interface along with extracellular loops (ECL) of *NmLbpA* (orange). The binding interface can be divided into three regions (dashed boxes and oval). (B) At site 1, C2 subdomain of Lactoferrin interacts with ECL2, 3 and 5 of *NmLbpA*. (C) At site 2, C1 subdomain contacts with ECL5, 7, 8 and 10. Furthermore, plug loop from the lumen of the barrel docks into a hydrophobic pocket of C1 subdomain (inset). (D) A helix in the ECL3 (L3 helix finger) docks at the edge of the cleft between C1 and C2 subdomains of lactoferrin.

The lactoferrin C2 subdomain interacts with surface extended extracellular loops of *NmLbpA* at site 1 and 3, encompassing $\sim 889.2 \text{ \AA}^2$ of buried surface area (**Figure 4.6B**). The C1 subdomain of lactoferrin primarily interacts with the ECL5, 7, 8, and 10 of *NmLbpA* with $\sim 1376 \text{ \AA}^2$ of buried surface area (**Figure 4.6C**). Additionally, the loop from the plug domain of *NmLbpA* docks at a small hydrophobic pocket in the C1 subdomain of lactoferrin (**Figure 4.6C, inset**). ECL3 of *NmLbpA* interacts with both the C1 and C2 subdomains of lactoferrin. At site 3, ECL3 is docked at the edge of the cleft between C1 and C2 subdomains (**Figure 4.6D**). These interactions could be partially responsible for lactoferrin conformation change.

4.4.4 *NmLbpA*-mediated iron extraction from lactoferrin upon binding

Holo-lactoferrin contains two irons, one in each lobe. The iron is coordinated by residues contributed from both subdomains of a lobe, thereby representing a closed conformation. In the current study, holo-lactoferrin was used for complex formation with *NmLbpA*, however, the C-lobe is in an intermediate open conformation in the *NmLbpA*-lactoferrin structure whereas N-lobe is in closed conformation as observed by comparing to holo¹²⁴- and apo-lactoferrin¹²⁶ (**Figures 4.5B and 4.7**). Structural alignment focused on C1 shows ~27° rigid body rotation of the C2

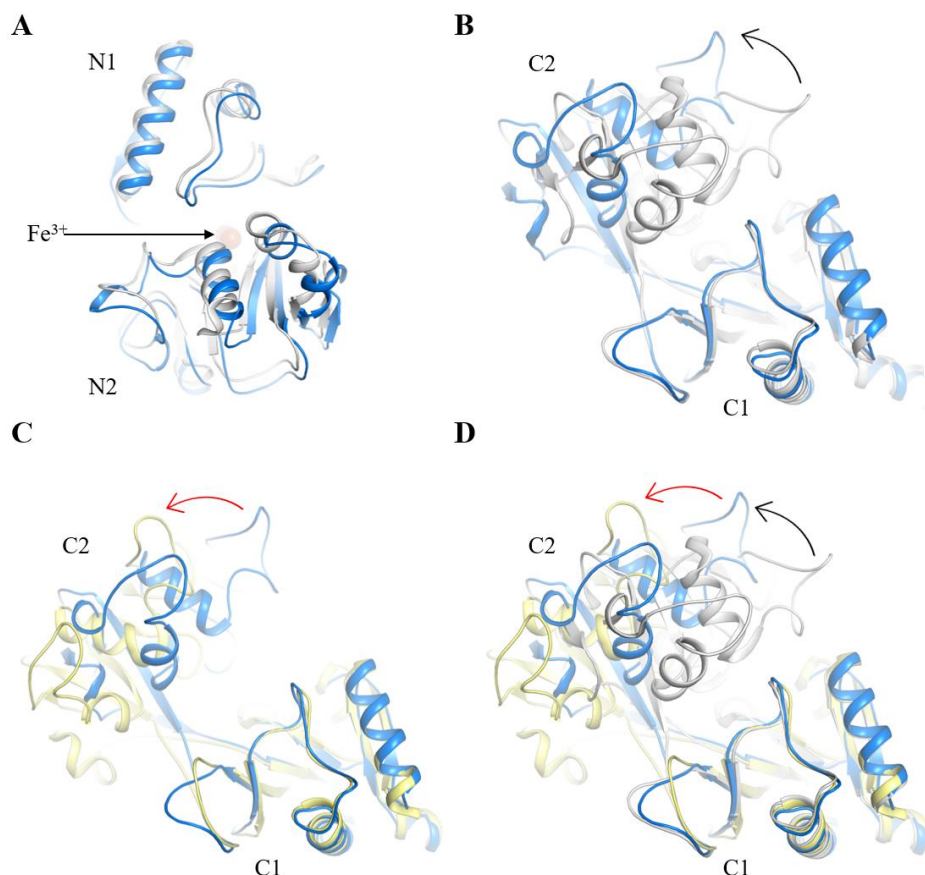


Figure 4.7. A structural comparison of apo-, holo-, and LbpA-bound lactoferrin. (A) An alignment of lactoferrin N-lobe from the complex (marine) with holo-lactoferrin N-lobe (grey; PDB ID 2BJJ¹²⁴). Structural alignment of lactoferrin C-lobe from the complex (marine) with holo-lactoferrin C-lobe (B), apo-lactoferrin C-lobe (yellow; PDB ID 1DTZ¹²⁶) (C) and both holo- and apo-lactoferrin (D). The curved black arrow represents the rotation of C2 subdomain from closed to open intermediate conformation. The Red arrow represents the rotation of C2 subdomain from intermediate to fully open conformation. The iron ion is shown as brown sphere.

compared to holo-lactoferrin. This conformational change would disrupt the iron coordination, promoting release from lactoferrin. Therefore, we postulate that upon binding *NmLbpA*,

lactoferrin undergoes a conformational change which ejects the iron for subsequent import through the barrel. Further studies are needed to test this hypothesis and to determine the exact mechanism.

4.5 Discussion and conclusion

To obtain iron during pathogenesis, *Neisseria* must sequester iron from host iron-containing proteins. LbpA binds to lactoferrin and acquires iron from it through an unknown mechanism. Our cryo-EM structure of *NmLbpA*-lactoferrin complex provides insights into this process. The extracellular loops of *NmLbpA* form an extensive binding interface for lactoferrin. ECL3 helix finger docks at the edge of the cleft between the C1 and C2 subdomains of lactoferrin, inducing a conformational transition from an iron-bound closed conformation to an iron-free intermediate open conformation. This observation likely explains why *NmLbpA* cannot differentiate between apo- or holo-lactoferrin. An additional binding partner, *NmLbpB*, is required for selective recognition of holo-lactoferrin for iron acquisition. Indeed, the *NmLbpB*-lactoferrin crystal structure indicates that *NmLbpB* selectively binds to holo-lactoferrin and traps it in an iron-bound closed conformation¹⁸⁸ (Chapter 2), suggesting that tandem binding to *NmLbpB* and *NmLbpA* ensures efficient iron acquisition.

The periplasm exposed N-terminal residues of *NmLbpA* harboring the TonB-box were not resolved in the cryo-EM density. Although it is plausible that docking of the plug loop into the hydrophobic pocket of the lactoferrin C1 subdomain could induce a conformational change in the TonB-box, further studies are needed to address lactoferrin sensing and TonB-box plasticity.

The overall architecture of the *NmLbpA*-lactoferrin complex displays high similarity to the *NmTbpA*-transferrin complex (PDB ID 3V8X⁴³; RMSD 2.759 Å for overall alignment and 0.912 Å for TbpA focused alignment) (**Figure 4.8A**). Although the N-lobe of lactoferrin and transferrin are in closed and open conformation, respectively, the C-lobe of both proteins are in an intermediate open conformation. In the complex, iron-free C-lobe subdomain C2 undergo $\sim 27^\circ$ rigid-body rotation with respect to C1 subdomain when compared to iron-bound closed conformation. The plug and β -barrel domains of both TbpA and LbpA align very well (RMSD 0.912 Å), whereas major differences stem from the length and conformation of extracellular loops (**Figure 4.8B and C**). Three major differences occur at the protein-protein binding interface: (i) rigid body rotation of transferrin/lactoferrin, (ii) plug loop docking site, and (iii) ECL3 helix finger (L3 helix) conformations. Lactoferrin is rotated $\sim 10^\circ$ compared to transferrin with respect to the

binding interface. This difference could be attributed to differential conformations of the extracellular loops. The plug loop from *NmLbpA* is positioned in a small hydrogen pocket underneath the C1 subdomain of lactoferrin, whereas the *NmTbpA* plug loop docks at a relatively larger negatively charged pocket (Figure 4.6C, inset and 4.8C). Finally, the *NmLbpA* L3 helix docks at the edge of the cleft in the C-lobe of lactoferrin, whereas the *NmTbpA* L3 helix is positioned inside the cleft (Figure 4.8D).

In the absence of the *NmLbpA*-*NmLbpB*-lactoferrin ternary complex structure, we created an *in-silico* model of the ternary complex by aligning the lactoferrin N-lobes of the *NmLbpA*-lactoferrin cryo-EM structure and the *NmLbpB*-lactoferrin crystal structure (PDB 7JRD¹⁸⁸). The assembled triple complex shows that both *NmLbpA* and *NmLbpB* bind to the C-lobe of lactoferrin, albeit at distinct sites (Figure 4.9). The overall architecture of the triple complex resembles the low-resolution negative stain EM classes of the *NmTbpA*-*NmTbpB*-transferrin complex⁴³.

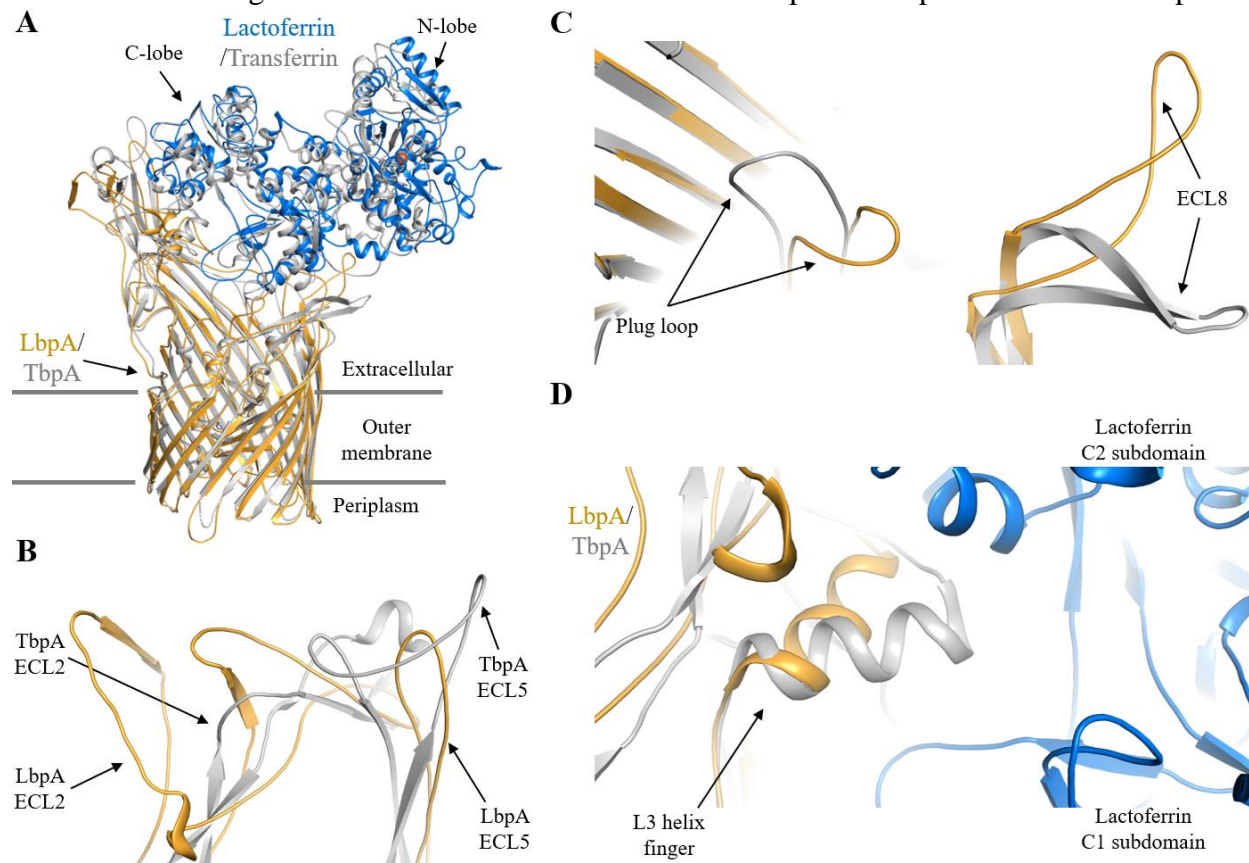


Figure 4.8. A structural comparison of LbpA-lactoferrin with TbpA-transferrin. (A) Structural superposition of LbpA-lactoferrin (orange/marine blue) structure with TbpA-transferrin structure (PDB ID 3V8X⁴³, grey) shows similar architecture of these complexes. However, there are differences in the conformation of the extracellular loops (B), the plug loop (C), and L3 helix finger (D)

Additionally, the model suggests that the *NmLbpB* N-lobe handle domain might interact with ECL10 of *NmLbpA* (**Figure 4.9**). The triple complex formation on the bacterial surface may

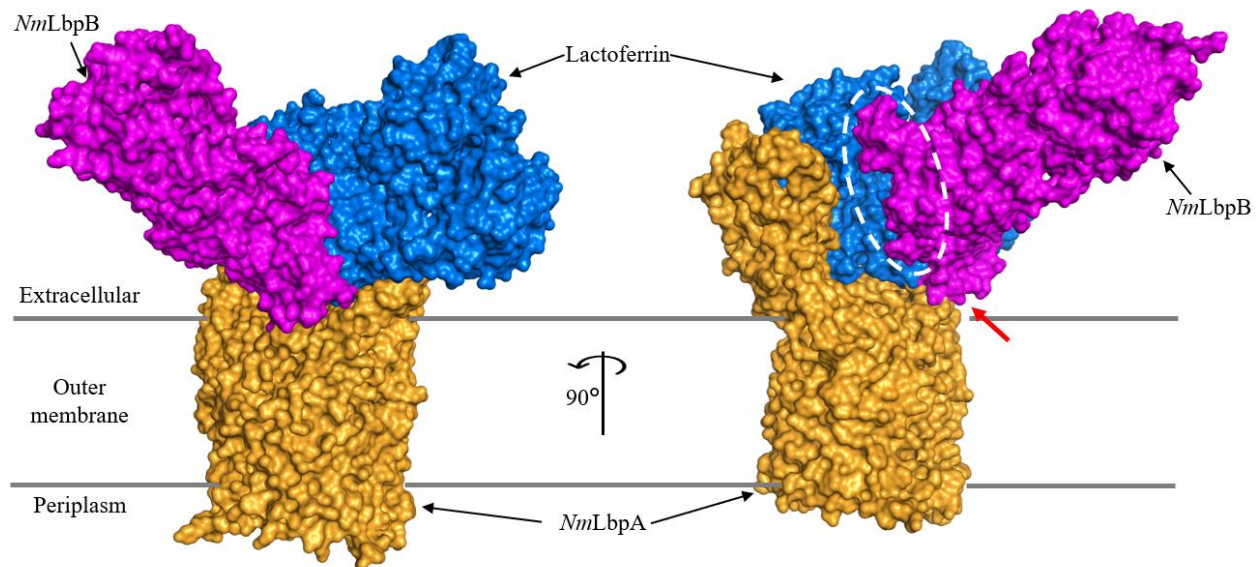


Figure 4.9. In-silico complex formation between *NmLbpA*, *NmLbpB*, and lactoferrin. The N-lobe of lactoferrin from LbpB-lactoferrin structure was aligned with the N-lobe of lactoferrin in LbpA-lactoferrin. The modelled complex suggests that LbpA and LbpB bind to distinct sites on lactoferrin (white oval). In the triple complex, LbpA and LbpB form minimal contact with each other (red arrow).

ensure iron trapping inside a cavity and stop diffusion of the extracted iron in the extracellular space.

In the *NmTbpA*-apo-transferrin structure, *NmTbpA* L3 helix finger docks into a cleft between C1 and C2 subdomains of transferrin⁴³. This L3 helix finger induces a conformational change in transferrin, leading to iron release. However, the L3 helix finger of *NmLbpA* docks at the edge of the cleft between the C1 and C2 subdomains of lactoferrin (**Figure 4.6A**). Superposition of holo-lactoferrin along C1 subdomain in the complex suggests that *NmLbpA* residues K390 and K394 create a local positive charged patch that would potentially repulse the R588 side chain positioned in the cleft in holo-lactoferrin and drive a conformational change in lactoferrin (**Figure 4.10**). Although these sequences of events are plausible, they are speculative and warrant further investigation.

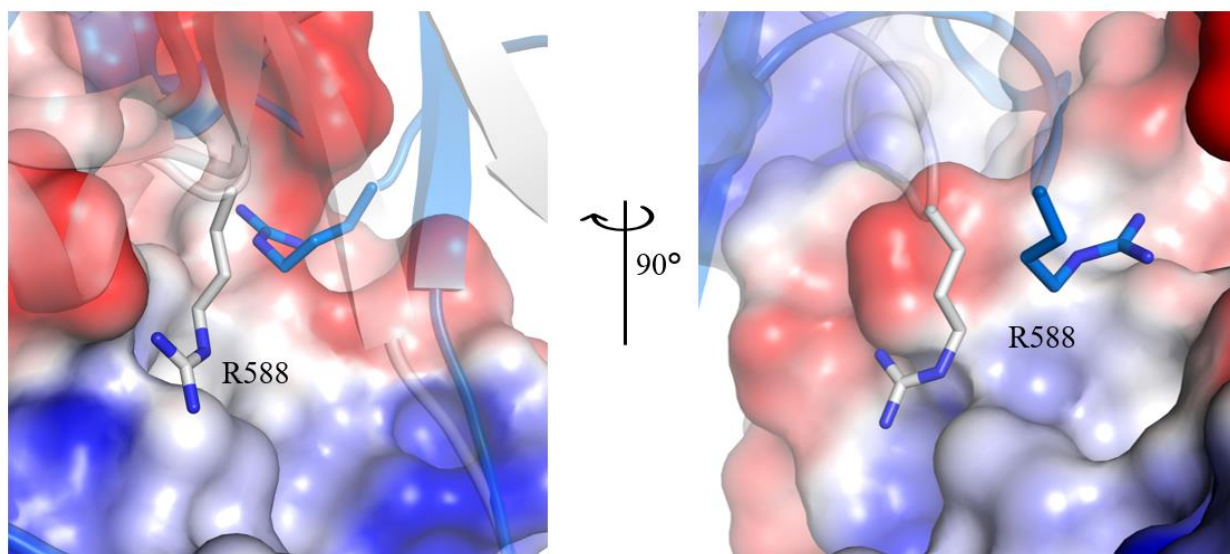


Figure 4.10. A plausible conformation change driver in LbpA. (A) Residue R588 of lactoferrin C2 subdomain undergoes large conformational shift from holo-lactoferrin (grey) to apo-lactoferrin (marine blue) upon binding to LbpA (electrostatic potential surface). The local charge distribution at the L3 helix finger might be causing the conformation transition from holo- to apo-lactoferrin.

CHAPTER 5. SUMMARY AND FUTURE DIRECTIONS

The overall goal of the current study was to determine the molecular mechanism of lactoferrin binding proteins. While more studies are required to assemble all the pieces of the puzzle, our structural and functional studies provide insights into the role of LbpA and LbpB in iron acquisition from lactoferrin. Furthermore, we characterized LbpB's role in protecting the pathogen from the host cationic antimicrobial peptide Lfcn. Thus, the knowledge gained from our studies can be used for therapeutic drug development against *Neisseria*.

Neisseria utilize various outer-membrane proteins to obtain iron from the host proteins⁷⁵. Lactoferrin binding proteins, LbpA and LbpB, bind to human lactoferrin and extract iron from it^{76-79,134}. Previous studies have shown that LbpA alone is sufficient for iron acquisition from lactoferrin, however, it shows no specific preference between apo- or holo-lactoferrin^{79,136}. Conversely, LbpB shows a higher preference towards holo-lactoferrin over apo-lactoferrin¹¹⁶. Even though LbpB is not required for iron acquisition, LbpB⁺ gonococcal strains showed significantly higher iron uptake than LbpB⁻ strains¹³⁶. However, the role of LbpB in this process has remained elusive.

We determined the three-dimensional structures of the Nme and Ngo LbpBs in complex with human lactoferrin. In both structures, the N-lobe of LbpB binds to the C-lobe of lactoferrin. In the complex structure, lactoferrin is present in an iron-bound closed conformation and shows minimal to no conformational change when compared to the holo-lactoferrin structure. Analysis of protein-protein binding interfaces suggested that apo-lactoferrin would not be able to maintain the necessary interactions with LbpB. This observation is consistent with previous results, thereby demonstrating LbpB's preference for holo-lactoferrin over apo-lactoferrin. Comparison of the LbpB-lactoferrin with TbpB-transferrin complex shows a high structural and potentially functional similarity between them. Therefore, we propose that LbpB binds to holo-lactoferrin and traps it in an iron-bound closed conformation for iron extraction by LbpA.

The cryo-EM structure of LbpA in complex with lactoferrin showed that both subdomains of the lactoferrin C-lobe bind to a large interface formed by the extracellular loops of LbpA. Additionally, the LbpA plug loop docks at a hydrophobic pocket in the C1 subdomain of lactoferrin. In the complex, lactoferrin C-lobe undergoes a large conformational change from an iron-bound closed conformation to an iron-free intermediate open conformation, whereas the N-

lobe maintains its closed conformation. LbpA's ability to induce a conformational transition from holo-lactoferrin to apo-lactoferrin would enable it to acquire iron in the absence of LbpB, however, it would not be able to differentiate between apo- and holo-lactoferrin. These results are consistent with previous studies that focused on LbpA-mediated iron acquisition.

Based on our structures of LbpA and LbpB in complex with lactoferrin, we propose the following mechanism of iron acquisition from lactoferrin. *Neisseria* utilize the surface anchored lipoprotein LbpB to selectively bind to holo-lactoferrin and trap it in an iron-bound closed conformation. Subsequently, LbpB shuttles the trapped holo-lactoferrin to LbpA and forms a triple complex. In the triple complex, LbpA binding induces conformational changes in lactoferrin, leading to iron release from lactoferrin. The LbpA plug loop senses the bound lactoferrin, resulting in TonB binding to the periplasmic face of the β -barrel. Powered by the Ton complex, TonB perturbs the plug domain and enables the iron to be transported across the bacteria's outer membrane. The plug domain perturbations might destabilize LbpA's interaction with lactoferrin, which leads to dissociation of the LbpB-lactoferrin complex from LbpA. Subsequently, LbpB disassociates from apo-lactoferrin. Upon transport of iron, TonB disassociates from LbpA, and the plug domain occludes the β -barrel again, thus completing the iron acquisition cycle.

5.1 Dual function of LbpB

Both LbpA and LbpB can bind to lactoferrin and are involved in iron acquisition process. Since LbpB is not required for iron acquisition and can be released from the surface, this suggests that it may play some additional function during pathogenesis¹⁴⁴. Indeed, LbpB protects the Nme from the antimicrobial activity of the cationic peptides^{132,145,146}. However, no further studies have explored the molecular mechanism behind LbpB-mediated cationic antimicrobial peptide neutralization.

As mentioned above, the N-lobe of LbpB binds to holo-lactoferrin and delivers it to LbpA for iron extraction. Additionally, we employed SEC-SAXS, mutagenesis and ITC to study the Lfcn binding to LbpB. Lfcn induces local conformational changes upon binding to anionic loops in the C-lobe of LbpB. Lfcn and lactoferrin bind to LbpB at distinct sites and do not affect each other's binding to LbpB. Based on these observations, we propose that LbpB serves a dual function in mediating *Neisseria* pathogenesis. At the bacterial surface, the LbpB N-lobe binds to lactoferrin and traps it in an iron-bound closed conformation and then shuttles it to LbpA. Simultaneously,

the LbpB C-lobe anionic loops bind to Lfcn and neutralize its antimicrobial activity through an unknown mechanism. During infection, LbpB is proteolytically cleaved from the bacterial surface by the NalP autotransporter¹⁴⁴. Upon release, LbpB diffuses into the host environment and prevents Lfcn from reaching the bacterial surface by binding to it. Therefore, LbpB is important for protecting the pathogen from Lfcn-mediated killing.

5.2 Outstanding questions

Overall, our structural and functional studies provide a framework for understanding the molecular mechanisms of LbpA- and LbpB-mediated iron import and LbpB's role in immune evasion. However, there are still many outstanding questions that need to be answered, including: how does LbpA induce conformational changes in lactoferrin? What conformational changes does TonB binding induce? What is the exact mechanism of lactoferrin dissociation from LbpA? How does LbpB neutralize Lfcn? And can LbpB bind to other cationic antimicrobial peptides? Thus, future research endeavors will need to address these unanswered questions to help bridge the gap in our understanding of *Neisseria* pathogenesis, as well as to aid in therapeutic drug development against the widespread pathogen.

REFERENCES

- 1 Seifert, H. S. Location, Location, Location—Commensalism, Damage and Evolution of the Pathogenic *Neisseria*. *Journal of Molecular Biology* **431**, 3010-3014, doi:10.1016/j.jmb.2019.04.007 (2019).
- 2 Harrison, O. B. *et al.* Description and Nomenclature of *Neisseria meningitidis* Capsule Locus. *Emerging Infectious Diseases* **19**, 566-573, doi:10.3201/eid1904.111799 (2013).
- 3 Caugant, D. A. Population genetics and molecular epidemiology of *Neisseria meningitidis*. *APMIS* **106**, 505-525, doi:10.1111/j.1699-0463.1998.tb01379.x (1998).
- 4 Caugant, D. A. *et al.* Asymptomatic carriage of *Neisseria meningitidis* in a randomly sampled population. *Journal of Clinical Microbiology* **32**, 323-330, doi:doi:10.1128/jcm.32.2.323-330.1994 (1994).
- 5 Cartwright, K. A. V., Stuart, J. M., Jones, D. M. & Noah, N. D. The Stonehouse survey: nasopharyngeal carriage of meningococci and *Neisseria lactamica*. *Epidemiology and Infection* **99**, 591-601, doi:10.1017/s0950268800066449 (1987).
- 6 Claus, H. *et al.* Genetic Analysis of Meningococci Carried by Children and Young Adults. *The Journal of Infectious Diseases* **191**, 1263-1271, doi:10.1086/428590 (2005).
- 7 Stephens, D. S., Greenwood, B. & Brandtzaeg, P. Epidemic meningitis, meningococcaemia, and *Neisseria meningitidis*. *The Lancet* **369**, 2196-2210, doi:10.1016/s0140-6736(07)61016-2 (2007).
- 8 Johswich, K. Innate immune recognition and inflammation in *Neisseria meningitidis* infection. *Pathogens and Disease* **75**, doi:10.1093/femspd/ftx022 (2017).
- 9 Macneil, J. R. *et al.* Epidemiology of Infant Meningococcal Disease in the United States, 2006-2012. *PEDIATRICS* **135**, e305-e311, doi:10.1542/peds.2014-2035 (2015).
- 10 Christensen, H., May, M., Bowen, L., Hickman, M. & Trotter, C. L. Meningococcal carriage by age: a systematic review and meta-analysis. *The Lancet Infectious Diseases* **10**, 853-861, doi:10.1016/s1473-3099(10)70251-6 (2010).
- 11 Coureuil, M. *et al.* Pathogenesis of Meningococcemia. *Cold Spring Harbor Perspectives in Medicine* **3**, a012393-a012393, doi:10.1101/cshperspect.a012393 (2013).
- 12 McCarthy, P. C., Sharyan, A. & Sheikh Moghaddam, L. Meningococcal Vaccines: Current Status and Emerging Strategies. *Vaccines* **6**, 12, doi:10.3390/vaccines6010012 (2018).
- 13 Hedari, C., Khinkarly, R. & Dbaiibo, G. Meningococcal serogroups A, C, W-135, and Y tetanus toxoid conjugate vaccine: a new conjugate vaccine against invasive meningococcal disease. *Infection and Drug Resistance*, 85, doi:10.2147/idr.s36243 (2014).
- 14 Shao, P.-L. *et al.* Safety and Immunogenicity of a Tetravalent Polysaccharide Vaccine Against Meningococcal Disease. *Journal of the Formosan Medical Association* **108**, 539-547, doi:10.1016/s0929-6646(09)60371-5 (2009).
- 15 Feavers, I. M., Maiden, M. C. J. & Papasian, C. J. Recent Progress in the Prevention of Serogroup B Meningococcal Disease. *Clinical and Vaccine Immunology* **24**, e00566-00516, doi:doi:10.1128/CVI.00566-16 (2017).
- 16 Mazamay, S. *et al.* An overview of bacterial meningitis epidemics in Africa from 1928 to 2018 with a focus on epidemics “outside-the-belt”. *BMC Infectious Diseases* **21**, doi:10.1186/s12879-021-06724-1 (2021).

- 17 Van Kessel, F., Van Den Ende, C., Oordt-Speets, A. M. & Kyaw, M. H. Outbreaks of meningococcal meningitis in non-African countries over the last 50 years: a systematic review. *Journal of Global Health* **9**, doi:10.7189/jogh.09.010411 (2019).
- 18 Soeters, H. M. *et al.* University-Based Outbreaks of Meningococcal Disease Caused by Serogroup B, United States, 2013–2018. *Emerging Infectious Diseases* **25**, 434-440, doi:10.3201/eid2503.181574 (2019).
- 19 Quillin, S. J. & Seifert, H. S. *Neisseria gonorrhoeae* host adaptation and pathogenesis. *Nature Reviews Microbiology* **16**, 226-240, doi:10.1038/nrmicro.2017.169 (2018).
- 20 Humbert, M. V. & Christodoulides, M. Atypical, Yet Not Infrequent, Infections with *Neisseria* Species. *Pathogens* **9**, 10, doi:10.3390/pathogens9010010 (2019).
- 21 Unemo, M. & Shafer, W. M. Antibiotic resistance in *Neisseria gonorrhoeae*: origin, evolution, and lessons learned for the future. *Annals of the New York Academy of Sciences* **1230**, E19-E28, doi:10.1111/j.1749-6632.2011.06215.x (2011).
- 22 CDC. Antibiotic Resistance Threats in the United States. (2019).
- 23 Gianecini, R., Oviedo, C., Stafforini, G. & Galarza, P. *Neisseria gonorrhoeae* Resistant to Ceftriaxone and Cefixime, Argentina. *Emerging Infectious Diseases* **22**, 1139-1141, doi:10.3201/eid2206.152091 (2016).
- 24 Russell, M. W., Jerse, A. E. & Gray-Owen, S. D. Progress Toward a Gonococcal Vaccine: The Way Forward. *Frontiers in Immunology* **10**, doi:10.3389/fimmu.2019.02417 (2019).
- 25 Yadav, R. *et al.* Structural Basis for Evasion of Nutritional Immunity by the Pathogenic *Neisseriae*. *Frontiers in Microbiology* **10**, doi:10.3389/fmicb.2019.02981 (2020).
- 26 Fitzpatrick, A. W. P. *et al.* Structure of the MacAB–TolC ABC-type tripartite multidrug efflux pump. *Nature Microbiology* **2**, 17070, doi:10.1038/nmicrobiol.2017.70 (2017).
- 27 Koebnik, R., Locher, K. P. & Van Gelder, P. Structure and function of bacterial outer membrane proteins: barrels in a nutshell. *Molecular Microbiology* **37**, 239-253, doi:10.1046/j.1365-2958.2000.01983.x (2000).
- 28 Noinaj, N., Guillier, M., Barnard, T. J. & Buchanan, S. K. TonB-Dependent Transporters: Regulation, Structure, and Function. *Annual Review of Microbiology* **64**, 43-60, doi:10.1146/annurev.micro.112408.134247 (2010).
- 29 Biswas, G. D., Anderson, J. E. & Sparling, P. F. Cloning and functional characterization of *Neisseria gonorrhoeae* tonB, exbB and exbD genes. *Molecular Microbiology* **24**, 169-179, doi:10.1046/j.1365-2958.1997.3421692.x (1997).
- 30 Stojiljkovic, I. & Srinivasan, N. *Neisseria meningitidis* tonB, exbB, and exbD genes: Ton-dependent utilization of protein-bound iron in *Neisseriae*. *Journal of Bacteriology* **179**, 805-812, doi:10.1128/jb.179.3.805-812.1997 (1997).
- 31 Celia, H. *et al.* Structural insight into the role of the Ton complex in energy transduction. *Nature* **538**, 60-65, doi:10.1038/nature19757 (2016).
- 32 Maki-Yonekura, S. *et al.* Hexameric and pentameric complexes of the ExbBD energizer in the Ton system. *eLife* **7**, doi:10.7554/elife.35419 (2018).
- 33 Sverzhinsky, A. *et al.* Membrane Protein Complex ExbB₄-ExbD₁-TonB₁ from *Escherichia coli* Demonstrates Conformational Plasticity. *Journal of Bacteriology* **197**, 1873-1885, doi:10.1128/JB.00069-15 (2015).
- 34 Sverzhinsky, A. *et al.* Coordinated Rearrangements between Cytoplasmic and Periplasmic Domains of the Membrane Protein Complex ExbB-ExbD of *Escherichia coli*. *Structure* **22**, 791-797, doi:10.1016/j.str.2014.02.010 (2014).

- 35 Higgs, P. I., Larsen, R. A. & Postle, K. Quantification of known components of the Escherichia coli TonB energy transduction system: TonB, ExbB, ExbD and FepA. *Molecular Microbiology* **44**, 271-281, doi:https://doi.org/10.1046/j.1365-2958.2002.02880.x (2002).
- 36 Pramanik, A. *et al.* Oligomeric Structure of ExbB and ExbB-ExbD Isolated from Escherichia coli As Revealed by LILBID Mass Spectrometry. *Biochemistry* **50**, 8950-8956, doi:10.1021/bi2008195 (2011).
- 37 Celia, H. *et al.* Cryo-EM structure of the bacterial Ton motor subcomplex ExbB–ExbD provides information on structure and stoichiometry. *Communications Biology* **2**, doi:10.1038/s42003-019-0604-2 (2019).
- 38 Ollis, A. A., Manning, M., Held, K. G. & Postle, K. Cytoplasmic membrane protonmotive force energizes periplasmic interactions between ExbD and TonB. *Molecular Microbiology* **73**, 466-481, doi:10.1111/j.1365-2958.2009.06785.x (2009).
- 39 Schauer, K., Rodionov, D. A. & De Reuse, H. New substrates for TonB-dependent transport: do we only see the ‘tip of the iceberg’? *Trends in Biochemical Sciences* **33**, 330-338, doi:10.1016/j.tibs.2008.04.012 (2008).
- 40 Anderson, J. E., Hobbs, M. M., Biswas, G. D. & Sparling, P. F. Opposing selective forces for expression of the gonococcal lactoferrin receptor. *Molecular Microbiology* **48**, 1325-1337, doi:10.1046/j.1365-2958.2003.03496.x (2003).
- 41 Wang, J., Xiong, K., Pan, Q., He, W. & Cong, Y. Application of TonB-Dependent Transporters in Vaccine Development of Gram-Negative Bacteria. *Frontiers in Cellular and Infection Microbiology* **10**, doi:10.3389/fcimb.2020.589115 (2021).
- 42 Fegan, J. E. *et al.* Utility of Hybrid Transferrin Binding Protein Antigens for Protection Against Pathogenic Neisseria Species. *Frontiers in Immunology* **10**, doi:10.3389/fimmu.2019.00247 (2019).
- 43 Noinaj, N. *et al.* Structural basis for iron piracy by pathogenic Neisseria. *Nature* **483**, 53-58, doi:10.1038/nature10823 (2012).
- 44 Moynié, L. *et al.* The complex of ferric-enterobactin with its transporter from Pseudomonas aeruginosa suggests a two-site model. *Nature Communications* **10**, doi:10.1038/s41467-019-11508-y (2019).
- 45 Bhamidimarri, S. P. *et al.* Acquisition of ionic copper by the bacterial outer membrane protein OprC through a novel binding site. *PLOS Biology* **19**, e3001446, doi:10.1371/journal.pbio.3001446 (2021).
- 46 Ferguson, A. D. *et al.* Crystal structure of the antibiotic albomycin in complex with the outer membrane transporter FhuA. *Protein Science* **9**, 956-963, doi:10.1110/ps.9.5.956 (2000).
- 47 Cobessi, D., Meksem, A. & Brillet, K. Structure of the heme/hemoglobin outer membrane receptor ShuA from Shigella dysenteriae: Heme binding by an induced fit mechanism. *Proteins: Structure, Function, and Bioinformatics* **78**, 286-294, doi:10.1002/prot.22539 (2010).
- 48 Lukacik, P. *et al.* Structural engineering of a phage lysin that targets Gram-negative pathogens. *Proceedings of the National Academy of Sciences* **109**, 9857-9862, doi:10.1073/pnas.1203472109 (2012).
- 49 Cherezov, V. *et al.* In Meso Structure of the Cobalamin Transporter, BtuB, at 1.95 Å Resolution. *Journal of Molecular Biology* **364**, 716-734, doi:10.1016/j.jmb.2006.09.022 (2006).

- 50 Krieg, S. *et al.* Heme uptake across the outer membrane as revealed by crystal structures of the receptor-hemophore complex. *Proceedings of the National Academy of Sciences* **106**, 1045-1050, doi:10.1073/pnas.0809406106 (2009).
- 51 Locher, K. P. *et al.* Transmembrane Signaling across the Ligand-Gated FhuA Receptor. *Cell* **95**, 771-778, doi:10.1016/s0092-8674(00)81700-6 (1998).
- 52 Tuckman, M. & Osburne, M. S. In vivo inhibition of TonB-dependent processes by a TonB box consensus pentapeptide. *Journal of Bacteriology* **174**, 320-323, doi:10.1128/jb.174.1.320-323.1992 (1992).
- 53 Gumbart, J., Wiener, M. C. & Tajkhorshid, E. Mechanics of Force Propagation in TonB-Dependent Outer Membrane Transport. *Biophysical Journal* **93**, 496-504, doi:10.1529/biophysj.107.104158 (2007).
- 54 Cadieux, N., Bradbeer, C. & Kadner, R. J. Sequence Changes in the Ton Box Region of BtuB Affect Its Transport Activities and Interaction with TonB Protein. *Journal of Bacteriology* **182**, 5954-5961, doi:10.1128/jb.182.21.5954-5961.2000 (2000).
- 55 Shultis, D. D., Purdy, M. D., Banchs, C. N. & Wiener, M. C. Outer Membrane Active Transport: Structure of the BtuB:TonB Complex. *Science* **312**, 1396-1399, doi:doi:10.1126/science.1127694 (2006).
- 56 Hickman, S. J., Cooper, R. E. M., Bellucci, L., Paci, E. & Brockwell, D. J. Gating of TonB-dependent transporters by substrate-specific forced remodelling. *Nature Communications* **8**, 14804, doi:10.1038/ncomms14804 (2017).
- 57 Chimento, D. P., Kadner, R. J. & Wiener, M. C. Comparative structural analysis of TonB-dependent outer membrane transporters: Implications for the transport cycle. *Proteins: Structure, Function, and Bioinformatics* **59**, 240-251, doi:10.1002/prot.20416 (2005).
- 58 Scott, D. C. *et al.* Exchangeability of N Termini in the Ligand-gated Porins of Escherichia coli. *Journal of Biological Chemistry* **276**, 13025-13033, doi:10.1074/jbc.m011282200 (2001).
- 59 Braun, M., Killmann, H. & Braun, V. The beta-barrel domain of FhuADelta5-160 is sufficient for TonB-dependent FhuA activities of Escherichia coli. *Molecular Microbiology* **33**, 1037-1049, doi:10.1046/j.1365-2958.1999.01546.x (1999).
- 60 Ma, L. *et al.* Evidence of Ball-and-chain Transport of Ferric Enterobactin through FepA. *Journal of Biological Chemistry* **282**, 397-406, doi:10.1074/jbc.m605333200 (2007).
- 61 Weinberg, E. D. Iron and infection. *Microbiological Reviews* **42**, 45-66, doi:10.1128/mr.42.1.45-66.1978 (1978).
- 62 Johnson, A. P. The effect of iron on the metabolism and pathogenicity of Neisseria gonorrhoeae. *FEMS Microbiology Letters* **32**, 81-85, doi:10.1111/j.1574-6968.1985.tb01184.x (1985).
- 63 Raymond, K. N., Dertz, E. A. & Kim, S. S. Enterobactin: An archetype for microbial iron transport. *Proceedings of the National Academy of Sciences* **100**, 3584-3588, doi:10.1073/pnas.0630018100 (2003).
- 64 Otto, B. R., Verweij-Van Vught, A. M. J. J. & Maclaren, D. M. Transferrins and Heme-Compounds as Iron Sources for Pathogenic Bacteria. *Critical Reviews in Microbiology* **18**, 217-233, doi:10.3109/10408419209114559 (1992).
- 65 Weinberg, E. D. Nutritional Immunity. *JAMA* **231**, 39, doi:10.1001/jama.1975.03240130021018 (1975).
- 66 Hennigar, S. R. & Mcclung, J. P. Nutritional Immunity. *American Journal of Lifestyle Medicine* **10**, 170-173, doi:10.1177/1559827616629117 (2016).

- 67 Kumar, P., Khan, J. A., Yadav, S. & Singh, T. P. Crystal structure of equine apolactoferrin at 303 K providing further evidence of closed conformations of N and C lobes. *Acta Crystallographica Section D Biological Crystallography* **58**, 225-232, doi:10.1107/s090744490101993x (2002).
- 68 Dierick, M., Vanrompay, D., Devriendt, B. & Cox, E. Lactoferrin, a versatile natural antimicrobial glycoprotein that modulates the host's innate immunity. *Biochemistry and Cell Biology* **99**, 61-65, doi:10.1139/bcb-2020-0080 (2021).
- 69 Ferguson, A. D., Hofmann, E., Coulton, J. W., Diederichs, K. & Welte, W. Siderophore-Mediated Iron Transport: Crystal Structure of FhuA with Bound Lipopolysaccharide. *Science* **282**, 2215-2220, doi:doi:10.1126/science.282.5397.2215 (1998).
- 70 Schalk, I. J., Mislin, G. L. A. & Brillet, K. in *Metal Transporters* 37-66 (Elsevier, 2012).
- 71 Wyckoff, E. E., Allred, B. E., Raymond, K. N., Payne, S. M. & DiRita, V. J. Catechol Siderophore Transport by *Vibrio cholerae*. *Journal of Bacteriology* **197**, 2840-2849, doi:doi:10.1128/JB.00417-15 (2015).
- 72 Norrod, P. & Williams, R. P. Growth of *Neisseria gonorrhoeae* in media deficient in iron without detection of siderophores. *Current Microbiology* **1**, 281-284, doi:10.1007/bf02601682 (1978).
- 73 West, S. E. & Sparling, P. F. Response of *Neisseria gonorrhoeae* to iron limitation: alterations in expression of membrane proteins without apparent siderophore production. *Infection and Immunity* **47**, 388-394, doi:doi:10.1128/iai.47.2.388-394.1985 (1985).
- 74 Mckenna, W. R., Mickelsen, P. A., Sparling, P. F. & Dyer, D. W. Iron uptake from lactoferrin and transferrin by *Neisseria gonorrhoeae*. *Infection and Immunity* **56**, 785-791, doi:10.1128/iai.56.4.785-791.1988 (1988).
- 75 Rohde, K. H. & Dyer, D. W. Mechanisms of iron acquisition by the human pathogens *Neisseria meningitidis* and *Neisseria gonorrhoeae*. *Frontiers in Bioscience-Landmark* **8**, 1186-1218, doi:10.2741/1133 (2003).
- 76 Biswas, G. D. & Sparling, P. F. Characterization of lbpA, the structural gene for a lactoferrin receptor in *Neisseria gonorrhoeae*. *Infection and Immunity* **63**, 2958-2967, doi:10.1128/iai.63.8.2958-2967.1995 (1995).
- 77 Pettersson, A., Klarenbeek, V., Van Deurzen, J., Poolman, J. T. & Tommassen, J. Molecular characterization of the structural gene for the lactoferrin receptor of the meningococcal strain H44/76. *Microbial Pathogenesis* **17**, 395-408, doi:10.1006/mpat.1994.1085 (1994).
- 78 Pettersson, A., Prinz, T., Umar, A., Van Der Biezen, J. & Tommassen, J. Molecular characterization of LbpB, the second lactoferrin-binding protein of *Neisseria meningitidis*. *Molecular Microbiology* **27**, 599-610, doi:10.1046/j.1365-2958.1998.00707.x (1998).
- 79 Schryvers, A. B. & Morris, L. J. Identification and characterization of the human lactoferrin-binding protein from *Neisseria meningitidis*. *Infection and Immunity* **56**, 1144-1149, doi:10.1128/iai.56.5.1144-1149.1988 (1988).
- 80 Schryvers, A. B. & Morris, L. J. Identification and characterization of the transferrin receptor from *Neisseria meningitidis*. *Molecular Microbiology* **2**, 281-288, doi:10.1111/j.1365-2958.1988.tb00029.x (1988).
- 81 Lewis, L. A. & Dyer, D. W. Identification of an iron-regulated outer membrane protein of *Neisseria meningitidis* involved in the utilization of hemoglobin complexed to haptoglobin. *Journal of Bacteriology* **177**, 1299-1306, doi:10.1128/jb.177.5.1299-1306.1995 (1995).

- 82 Lewis, L. A., Gray, E., Wang, Y. P., Roe, B. A. & Dyer, D. W. Molecular characterization of hpuAB, the haemoglobin-haptoglobin-utilization operon of *Neisseria meningitidis*. *Molecular Microbiology* **23**, 737-749, doi:10.1046/j.1365-2958.1997.2501619.x (1997).
- 83 Chen, C. J., Sparling, P. F., Lewis, L. A., Dyer, D. W. & Elkins, C. Identification and purification of a hemoglobin-binding outer membrane protein from *Neisseria gonorrhoeae*. *Infection and Immunity* **64**, 5008-5014, doi:10.1128/iai.64.12.5008-5014.1996 (1996).
- 84 Khun, H. H., Kirby, S. D. & Lee, B. C. A *Neisseria meningitidis* fbpABC Mutant Is Incapable of Using Nonheme Iron for Growth. *Infection and Immunity* **66**, 2330-2336, doi:doi:10.1128/IAI.66.5.2330-2336.1998 (1998).
- 85 Cash, D. R., Noinaj, N., Buchanan, S. K., Cornelissen, C. N. & Roy, C. R. Beyond the Crystal Structure: Insight into the Function and Vaccine Potential of TbpA Expressed by *Neisseria gonorrhoeae*. *Infection and Immunity* **83**, 4438-4449, doi:doi:10.1128/IAI.00762-15 (2015).
- 86 Pettersson, A. *et al.* Vaccine potential of the *Neisseria meningitidis* lactoferrin-binding proteins LbpA and LbpB. *Vaccine* **24**, 3545-3557, doi:10.1016/j.vaccine.2006.02.003 (2006).
- 87 Tandara, L. & Salamunic, I. Iron metabolism: current facts and future decisions. *Biochemia Medica*, 311-328, doi:10.11613/bm.2012.034 (2012).
- 88 Steere, A. N., Byrne, S. L., Chasteen, N. D. & Mason, A. B. Kinetics of iron release from transferrin bound to the transferrin receptor at endosomal pH. *Biochimica et Biophysica Acta (BBA) - General Subjects* **1820**, 326-333, doi:10.1016/j.bbagen.2011.06.003 (2012).
- 89 Wally, J. *et al.* The Crystal Structure of Iron-free Human Serum Transferrin Provides Insight into Inter-lobe Communication and Receptor Binding. *Journal of Biological Chemistry* **281**, 24934-24944, doi:10.1074/jbc.m604592200 (2006).
- 90 Steinlein, L. M., Ligman, C. M., Kessler, S. & Ikeda, R. A. Iron Release Is Reduced by Mutations of Lysines 206 and 296 in Recombinant N-Terminal Half-Transferrin. *Biochemistry* **37**, 13696-13703, doi:10.1021/bi980318s (1998).
- 91 Halbrooks, P. J. *et al.* Investigation of the Mechanism of Iron Release from the C-Lobe of Human Serum Transferrin: Mutational Analysis of the Role of a pH Sensitive Triad. *Biochemistry* **42**, 3701-3707, doi:10.1021/bi027071q (2003).
- 92 Steere, A. N. *et al.* Evidence that His349 acts as a pH-inducible switch to accelerate receptor-mediated iron release from the C-lobe of human transferrin. *JBIC Journal of Biological Inorganic Chemistry* **15**, 1341-1352, doi:10.1007/s00775-010-0694-2 (2010).
- 93 Mickelsen, P. A. & Sparling, P. F. Ability of *Neisseria gonorrhoeae*, *Neisseria meningitidis*, and commensal *Neisseria* species to obtain iron from transferrin and iron compounds. *Infection and Immunity* **33**, 555-564, doi:10.1128/iai.33.2.555-564.1981 (1981).
- 94 Lee, B. C. & Schryvers, A. B. Specificity of the lactoferrin and transferrin receptors in *Neisseria gonorrhoeae*. *Molecular Microbiology* **2**, 827-829, doi:10.1111/j.1365-2958.1988.tb00095.x (1988).
- 95 Schryvers, A. B. & Gonzalez, G. C. Receptors for transferrin in pathogenic bacteria are specific for the host's protein. *Canadian Journal of Microbiology* **36**, 145-147, doi:10.1139/m90-026 %M 2110858 (1990).
- 96 Blanton, K. J. *et al.* Genetic evidence that *Neisseria gonorrhoeae* produces specific receptors for transferrin and lactoferrin. *Journal of Bacteriology* **172**, 5225-5235, doi:10.1128/jb.172.9.5225-5235.1990 (1990).

- 97 Agarwal, S. *et al.* The Gonococcal Fur-Regulated *tbpA* and *tbpB* Genes Are Expressed during Natural Mucosal Gonococcal Infection. *Infection and Immunity* **73**, 4281-4287, doi:10.1128/IAI.73.7.4281-4287.2005 (2005).
- 98 Cornelissen, C. N. *et al.* The transferrin receptor expressed by gonococcal strain FA1090 is required for the experimental infection of human male volunteers. *Molecular Microbiology* **27**, 611-616, doi:10.1046/j.1365-2958.1998.00710.x (1998).
- 99 Rokbi, B. *et al.* Allelic Diversity of the Two Transferrin Binding Protein B Gene Isotypes among a Collection of Neisseria meningitidis Strains Representative of Serogroup B Disease: Implication for the Composition of a Recombinant TbpB-Based Vaccine. *Infection and Immunity* **68**, 4938-4947, doi:10.1128/iai.68.9.4938-4947.2000 (2000).
- 100 Rokbi, B. *et al.* Evaluation of recombinant transferrin-binding protein B variants from Neisseria meningitidis for their ability to induce cross-reactive and bactericidal antibodies against a genetically diverse collection of serogroup B strains. *Infection and Immunity* **65**, 55-63, doi:10.1128/iai.65.1.55-63.1997 (1997).
- 101 West, D. *et al.* Recombinant Neisseria meningitidis Transferrin Binding Protein A Protects against Experimental Meningococcal Infection. *Infection and Immunity* **69**, 1561-1567, doi:10.1128/iai.69.3.1561-1567.2001 (2001).
- 102 Thomas, C. E. *et al.* Vaccination of Mice with Gonococcal TbpB Expressed In Vivo from Venezuelan Equine Encephalitis Viral Replicon Particles. *Infection and Immunity* **74**, 1612-1620, doi:10.1128/IAI.74.3.1612-1620.2006 (2006).
- 103 Cornelissen, C. N. *et al.* Gonococcal transferrin-binding protein 1 is required for transferrin utilization and is homologous to TonB-dependent outer membrane receptors. *Journal of Bacteriology* **174**, 5788-5797, doi:10.1128/jb.174.18.5788-5797.1992 (1992).
- 104 Legrain, M. *et al.* Cloning and characterization of Neisseria meningitidis genes encoding the transferrin-binding proteins Tbp1 and Tbp2. *Gene* **130**, 73-80, doi:10.1016/0378-1119(93)90348-7 (1993).
- 105 Noinaj, N., Buchanan, S. K. & Cornelissen, C. N. The transferrin-iron import system from pathogenic Neisseria species. *Molecular Microbiology* **86**, 246-257, doi:10.1111/mmi.12002 (2012).
- 106 Burns, D. L., Cornelissen, C. N., Anderson, J. E., Boulton, I. C. & Sparling, P. F. Antigenic and Sequence Diversity in Gonococcal Transferrin-Binding Protein A. *Infection and Immunity* **68**, 4725-4735, doi:10.1128/IAI.68.8.4725-4735.2000 (2000).
- 107 Renauld-MongéNé, G. V. *et al.* Role of Transferrin Receptor from a Neisseria meningitidis *tbpB* Isotype II Strain in Human Transferrin Binding and Virulence. *Infection and Immunity* **72**, 3461-3470, doi:10.1128/iai.72.6.3461-3470.2004 (2004).
- 108 Boulton, I. C. *et al.* Transferrin-binding protein B isolated from Neisseria meningitidis discriminates between apo and diferric human transferrin. *Biochemical Journal* **334**, 269-273, doi:10.1042/bj3340269 (1998).
- 109 Retzer, M. D., Yu, R.-H., Zhang, Y., Gonzalez, G. C. & Schryvers, A. B. Discrimination between apo and iron-loaded forms of transferrin by transferrin binding protein B and its N-terminal subfragment. *Microbial Pathogenesis* **25**, 175-180, doi:10.1006/mpat.1998.0226 (1998).
- 110 Anderson, J. E., Sparling, P. F. & Cornelissen, C. N. Gonococcal transferrin-binding protein 2 facilitates but is not essential for transferrin utilization. *Journal of Bacteriology* **176**, 3162-3170, doi:10.1128/jb.176.11.3162-3170.1994 (1994).

- 111 Pintor, M., Gomez, J. A., Ferron, L., Ferreira, C. M. & Criado, M. T. Analysis of TbpA and TbpB functionality in defective mutants of *Neisseria meningitidis*. *Journal of Medical Microbiology* **47**, 757-760, doi:10.1099/00222615-47-9-757 (1998).
- 112 Gómez, J. A., Criado, M. T. & Ferreira, C. M. Cooperation between the components of the meningococcal transferrin receptor, TbpA and TbpB, in the uptake of transferrin iron by the 37-kDa ferric-binding protein (FbpA). *Research in Microbiology* **149**, 381-387, doi:10.1016/s0923-2508(98)80320-3 (1998).
- 113 Kenney, C. D. & Cornelissen, C. N. Demonstration and Characterization of a Specific Interaction between Gonococcal Transferrin Binding Protein A and TonB. *Journal of Bacteriology* **184**, 6138-6145, doi:10.1128/JB.184.22.6138-6145.2002 (2002).
- 114 Adamiak, P., Calmettes, C., Moraes, T. F. & Schryvers, A. B. Patterns of structural and sequence variation within isotype lineages of the *Neisseria meningitidis* transferrin receptor system. *MicrobiologyOpen* **4**, 491-504, doi:10.1002/mbo3.254 (2015).
- 115 Noto, J. M. & Cornelissen, C. N. Identification of TbpA Residues Required for Transferrin-Iron Utilization by *Neisseria gonorrhoeae*. *Infection and Immunity* **76**, 1960-1969, doi:10.1128/iai.00020-08 (2008).
- 116 Ostan, N. K. H. *et al.* Lactoferrin binding protein B – a bi-functional bacterial receptor protein. *PLOS Pathogens* **13**, e1006244, doi:10.1371/journal.ppat.1006244 (2017).
- 117 Guizzo, J. A. *et al.* The amino acid selected for generating mutant TbpB antigens defective in binding transferrin can compromise the in vivo protective capacity. *Scientific Reports* **8**, doi:10.1038/s41598-018-25685-1 (2018).
- 118 Retzer, M. D., Yu, R.-H. & Schryvers, A. B. Identification of sequences in human transferrin that bind to the bacterial receptor protein, transferrin-binding protein B. *Molecular Microbiology* **32**, 111-121, doi:10.1046/j.1365-2958.1999.01331.x (1999).
- 119 Krell, T. *et al.* Insight into the Structure and Function of the Transferrin Receptor from *Neisseria meningitidis* Using Microcalorimetric Techniques. *Journal of Biological Chemistry* **278**, 14712-14722, doi:10.1074/jbc.m204461200 (2003).
- 120 DeRocco, A. J. & Cornelissen, C. N. Identification of Transferrin-Binding Domains in TbpB Expressed by *Neisseria gonorrhoeae*. *Infection and Immunity* **75**, 3220-3232, doi:10.1128/IAI.00072-07 (2007).
- 121 Calmettes, C., Alcantara, J., Yu, R.-H., Schryvers, A. B. & Moraes, T. F. The structural basis of transferrin sequestration by transferrin-binding protein B. *Nature Structural & Molecular Biology* **19**, 358, doi:10.1038/nsmb.2251 (2012).
- 122 Kanyshkova, T. G., Buneva, V. N. & Nevinsky, G. A. *Biochemistry (Moscow)* **66**, 1-7, doi:10.1023/a:1002817226110 (2001).
- 123 SCHLABAC, M. R. & BATES, G. W. The synergistic binding of anions and Fe³⁺ by transferrin. Implications for the interlocking sites hypothesis. *The Journal of Biological Chemistry* **250**, 2182-2188 (1975).
- 124 Thomassen, E. A. J., Veen, H. A. V., Berkel, P. H. C. V., Nuijens, J. H. & Abrahams, J. P. The protein structure of recombinant human lactoferrin produced in the milk of transgenic cows closely matches the structure of human milk-derived lactoferrin. *Transgenic Research* **14**, 397-405, doi:10.1007/s11248-005-3233-0 (2005).
- 125 Norris, G. E., Anderson, B. F. & Baker, E. N. Molecular replacement solution of the structure of apolactoferrin, a protein displaying large-scale conformational change. *Acta Crystallographica Section B Structural Science* **47**, 998-1004, doi:10.1107/s0108768191008418 (1991).

- 126 Khan, J. A. *et al.* Camel Lactoferrin, a Transferrin-cum-Lactoferrin: Crystal Structure of Camel Apolactoferrin at 2.6Å Resolution and Structural Basis of its Dual Role. *Journal of Molecular Biology* **309**, 751-761, doi:10.1006/jmbi.2001.4692 (2001).
- 127 Jameson, G. B., Anderson, B. F., Norris, G. E., Thomas, D. H. & Baker, E. N. Structure of Human Apolactoferrin at 2.0 Å Resolution. Refinement and Analysis of Ligand-Induced Conformational Change. *Acta Crystallographica Section D Biological Crystallography* **54**, 1319-1335, doi:10.1107/s0907444998004417 (1998).
- 128 Jones, E. M., Smart, A., Bloomberg, G., Burgess, L. & Millar, M. R. Lactoferricin, a new antimicrobial peptide. *Journal of Applied Bacteriology* **77**, 208-214, doi:10.1111/j.1365-2672.1994.tb03065.x (1994).
- 129 Gifford, J. L., Hunter, H. N. & Vogel, H. J. Lactoferricin. *Cellular and Molecular Life Sciences* **62**, 2588-2598, doi:10.1007/s00018-005-5373-z (2005).
- 130 Nibbering, P. H. *et al.* Human Lactoferrin and Peptides Derived from Its N Terminus Are Highly Effective against Infections with Antibiotic-Resistant Bacteria. *Infection and Immunity* **69**, 1469-1476, doi:10.1128/iai.69.3.1469-1476.2001 (2001).
- 131 Dijkshoorn, L. *et al.* The Synthetic N-Terminal Peptide of Human Lactoferrin, hLF(1-11), Is Highly Effective against Experimental Infection Caused by Multidrug-Resistant *Acinetobacter baumannii*. *Antimicrobial Agents and Chemotherapy* **48**, 4919-4921, doi:10.1128/aac.48.12.4919-4921.2004 (2004).
- 132 MorgenthauAri, LivingstoneMargaret, AdamiakPaul & B., S. The role of lactoferrin binding protein B in mediating protection against human lactoferricin. *Biochemistry and Cell Biology* **90**, 417-423, doi:10.1139/o11-074 %M 22332888 (2012).
- 133 Mickelsen, P. A., Blackman, E. & Sparling, P. F. Ability of *Neisseria gonorrhoeae*, *Neisseria meningitidis*, and commensal *Neisseria* species to obtain iron from lactoferrin. *Infection and Immunity* **35**, 915-920, doi:10.1128/iai.35.3.915-920.1982 (1982).
- 134 Lewis, L. A. *et al.* Identification and Molecular Analysis of lbpBA, Which Encodes the Two-Component Meningococcal Lactoferrin Receptor. *Infection and Immunity* **66**, 3017-3023, doi:10.1128/iai.66.6.3017-3023.1998 (1998).
- 135 Wong, H. & Schryvers, A. B. Bacterial lactoferrin-binding protein A binds to both domains of the human lactoferrin C-lobe. *Microbiology* **149**, 1729-1737, doi:10.1099/mic.0.26281-0 (2003).
- 136 Biswas, G. D., Anderson, J. E., Chen, C.-J., Cornelissen, C. N. & Sparling, P. F. Identification and Functional Characterization of the *Neisseria gonorrhoeae* lbpB Gene Product. *Infection and Immunity* **67**, 455-459, doi:10.1128/iai.67.1.455-459.1999 (1999).
- 137 Noinaj, N., Cornelissen, C. N. & Buchanan, S. K. Structural insight into the lactoferrin receptors from pathogenic *Neisseria*. *Journal of Structural Biology* **184**, 83-92, doi:10.1016/j.jsb.2013.02.009 (2013).
- 138 Paul, A., J., B. A., Rolando, P. & B., S. A. Patterns of sequence variation within the *Neisseria meningitidis* lactoferrin binding proteins. *Biochemistry and Cell Biology* **90**, 339-350, doi:10.1139/o11-076 %M 22397513 (2012).
- 139 Ostan, N., Morgenthau, A., Yu, R. H., Gray-Owen, S. D. & Schryvers, A. B. A comparative, cross-species investigation of the properties and roles of transferrin- and lactoferrin-binding protein B from pathogenic bacteria. *Biochemistry and Cell Biology* **95**, 5-11, doi:10.1139/bcb-2016-0055 (2017).

- 140 Bonnah, R. A. & Schryvers, A. B. Preparation and Characterization of *Neisseria meningitidis* Mutants Deficient in Production of the Human Lactoferrin-Binding Proteins LbpA and LbpB. *Journal of Bacteriology* **180**, 3080-3090, doi:10.1128/jb.180.12.3080-3090.1998 (1998).
- 141 ArutyunovaElena *et al.* Crystal structure of the N-lobe of lactoferrin binding protein B from *Moraxella bovis*. *Biochemistry and Cell Biology* **90**, 351-361, doi:10.1139/o11-078 %M 22332934 (2012).
- 142 Brooks, C. L., Arutyunova, E. & Lemieux, M. J. The structure of lactoferrin-binding protein B from *Neisseria meningitidis* suggests roles in iron acquisition and neutralization of host defences. *Acta Crystallographica Section F Structural Biology Communications* **70**, 1312-1317, doi:10.1107/s2053230x14019372 (2014).
- 143 Pettersson, A., Van Der Biezen, J., Joosten, V., Hendriksen, J. & Tommassen, J. Sequence variability of the meningococcal lactoferrin-binding protein LbpB. *Gene* **231**, 105-110, doi:10.1016/s0378-1119(99)00109-2 (1999).
- 144 Roussel-JazéDé, V., Jongerius, I., Bos, M. P., Tommassen, J. & Van Ulsen, P. NalP-Mediated Proteolytic Release of Lactoferrin-Binding Protein B from the Meningococcal Cell Surface. *Infection and Immunity* **78**, 3083-3089, doi:10.1128/iai.01193-09 (2010).
- 145 Morgenthau, A., Beddek, A. & Schryvers, A. B. The Negatively Charged Regions of Lactoferrin Binding Protein B, an Adaptation against Anti-Microbial Peptides. *PLoS ONE* **9**, e86243, doi:10.1371/journal.pone.0086243 (2014).
- 146 Morgenthau, A., Partha, S. K., Adamiak, P. & Schryvers, A. B. The specificity of protection against cationic antimicrobial peptides by lactoferrin binding protein B. *BioMetals* **27**, 923-933, doi:10.1007/s10534-014-9767-y (2014).
- 147 Echenique-Rivera, H. *et al.* Transcriptome Analysis of *Neisseria meningitidis* in Human Whole Blood and Mutagenesis Studies Identify Virulence Factors Involved in Blood Survival. *PLoS Pathogens* **7**, e1002027, doi:10.1371/journal.ppat.1002027 (2011).
- 148 Tame, J. R. H. & Vallone, B. The structures of deoxy human haemoglobin and the mutant Hb Tyr α 42His at 120 K. *Acta Crystallographica Section D Biological Crystallography* **56**, 805-811, doi:10.1107/s0907444900006387 (2000).
- 149 Khoshouei, M., Radjainia, M., Baumeister, W. & Danev, R. Cryo-EM structure of haemoglobin at 3.2 Å determined with the Volta phase plate. *Nature Communications* **8**, doi:10.1038/ncomms16099 (2017).
- 150 Paoli, M., Liddington, R., Tame, J., Wilkinson, A. & Dodson, G. Crystal Structure of T State Haemoglobin with Oxygen Bound At All Four Haems. *Journal of Molecular Biology* **256**, 775-792, doi:10.1006/jmbi.1996.0124 (1996).
- 151 Thomas, J. O. & Edelstein, S. J. Observation of the Dissociation of Unliganded Hemoglobin. *Journal of Biological Chemistry* **247**, 7870-7874, doi:10.1016/s0021-9258(20)81781-5 (1972).
- 152 Shim, B.-S., Lee, T.-H. & Kang, Y.-S. Immunological and Biochemical Investigations of Human Serum Haptoglobin: Composition of Haptoglobin-Haemoglobin Intermediate, Haemoglobin-Binding Sites and Presence of Additional Alleles for β -Chain. *Nature* **207**, 1264-1267, doi:10.1038/2071264a0 (1965).
- 153 Kristiansen, M. *et al.* Identification of the haemoglobin scavenger receptor. *Nature* **409**, 198-201, doi:10.1038/35051594 (2001).

- 154 Lane-Serff, H., Macgregor, P., Lowe, E. D., Carrington, M. & Higgins, M. K. Structural basis for ligand and innate immunity factor uptake by the trypanosome haptoglobin-haemoglobin receptor. *eLife* **3**, doi:10.7554/elife.05553 (2014).
- 155 Stødtkilde, K., Torvund-Jensen, M., Moestrup, S. K. & Andersen, C. B. F. Structural basis for trypanosomal haem acquisition and susceptibility to the host innate immune system. *Nature Communications* **5**, 5487, doi:10.1038/ncomms6487 (2014).
- 156 Andersen, C. B. F. *et al.* Structure of the haptoglobin-haemoglobin complex. *Nature* **489**, 456-459, doi:10.1038/nature11369 (2012).
- 157 Dyer, D. W., West, E. P. & Sparling, P. F. Effects of serum carrier proteins on the growth of pathogenic neisseriae with heme-bound iron. *Infection and Immunity* **55**, 2171-2175, doi:doi:10.1128/iai.55.9.2171-2175.1987 (1987).
- 158 Lewis, L. A., Sung, M.-H., Gipson, M., Hartman, K. & Dyer, D. W. Transport of Intact Porphyrin by HpuAB, the Hemoglobin-Haptoglobin Utilization System of *Neisseria meningitidis*. *Journal of Bacteriology* **180**, 6043-6047, doi:doi:10.1128/JB.180.22.6043-6047.1998 (1998).
- 159 Chen, C.-J., Elkins, C. & Sparling, P. F. Phase Variation of Hemoglobin Utilization in *Neisseria gonorrhoeae*. *Infection and Immunity* **66**, 987-993, doi:10.1128/iai.66.3.987-993.1998 (1998).
- 160 Stojiljkovic, I., Larson, J., Hwa, V., Anic, S. & So, M. HmbR outer membrane receptors of pathogenic *Neisseria* spp.: iron-regulated, hemoglobin-binding proteins with a high level of primary structure conservation. *Journal of Bacteriology* **178**, 4670-4678, doi:10.1128/jb.178.15.4670-4678.1996 (1996).
- 161 Rohde, K. H., Gillasp, A. F., Hatfield, M. D., Lewis, L. A. & Dyer, D. W. Interactions of haemoglobin with the *Neisseria meningitidis* receptor HpuAB: the role of TonB and an intact proton motive force. *Molecular Microbiology* **43**, 335-354, doi:10.1046/j.1365-2958.2002.02745.x (2002).
- 162 Lewis, L. A. *et al.* Phase variation of HpuAB and HmbR, two distinct haemoglobin receptors of *Neisseria meningitidis* DNM2. *Molecular Microbiology* **32**, 977-989, doi:10.1046/j.1365-2958.1999.01409.x (1999).
- 163 Tauseef, I. *et al.* Influence of the combination and phase variation status of the haemoglobin receptors HmbR and HpuAB on meningococcal virulence. *Microbiology* **157**, 1446-1456, doi:10.1099/mic.0.046946-0 (2011).
- 164 Harrison, O. B., Bennett, J. S., Derrick, J. P., Maiden, M. C. J. & Bayliss, C. D. Distribution and diversity of the haemoglobin-haptoglobin iron-acquisition systems in pathogenic and non-pathogenic *Neisseria*. *Microbiology* **159**, 1920-1930, doi:10.1099/mic.0.068874-0 (2013).
- 165 Rohde, K. H. & Dyer, D. W. Analysis of Haptoglobin and Hemoglobin-Haptoglobin Interactions with the *Neisseria meningitidis* TonB-Dependent Receptor HpuAB by Flow Cytometry. *Infection and Immunity* **72**, 2494-2506, doi:doi:10.1128/IAI.72.5.2494-2506.2004 (2004).
- 166 Wong, C. T. *et al.* Structural analysis of haemoglobin binding by HpuA from the *Neisseriaceae* family. *Nature Communications* **6**, 10172, doi:10.1038/ncomms10172 (2015).
- 167 Stojiljkovic, I. *et al.* The *Neisseria meningitidis* haemoglobin receptor: its role in iron utilization and virulence. *Molecular Microbiology* **15**, 531-541, doi:10.1111/j.1365-2958.1995.tb02266.x (1995).

- 168 Bidmos, F. A. *et al.* Investigation into the Antigenic Properties and Contributions to
Growth in Blood of the Meningococcal Haemoglobin Receptors, HpuAB and HmbR.
PLOS ONE **10**, e0133855, doi:10.1371/journal.pone.0133855 (2015).
- 169 Harrison, B., Odile *et al.* Epidemiological Evidence for the Role of the Hemoglobin
Receptor, HmbR, in Meningococcal Virulence. *The Journal of Infectious Diseases* **200**,
94-98, doi:10.1086/599377 (2009).
- 170 Sevestre, J. *et al.* Differential expression of hemoglobin receptor, HmbR, between carriage
and invasive isolates of *Neisseria meningitidis* contributes to virulence: lessons from a
clonal outbreak. *Virulence* **9**, 923-929, doi:10.1080/21505594.2018.1460064 (2018).
- 171 Richardson, A. R. & Stojiljkovic, I. HmbR, a Hemoglobin-Binding Outer Membrane
Protein of *Neisseria meningitidis*, Undergoes Phase Variation. *Journal of
Bacteriology* **181**, 2067-2074, doi:10.1128/JB.181.7.2067-2074.1999 (1999).
- 172 Perkins-Balding, D., Baer, M. T. & Stojiljkovic, I. Identification of functionally important
regions of a haemoglobin receptor from *Neisseria meningitidis*. *Microbiology* **149**, 3423-
3435, doi:10.1099/mic.0.26448-0 (2003).
- 173 Manalastas-Cantos, K. *et al.* ATSAS 3.0: expanded functionality and new tools for small-
angle scattering data analysis. *Journal of Applied Crystallography* **54**, 343-355,
doi:10.1107/s1600576720013412 (2021).
- 174 Hopkins, J. B., Gillilan, R. E. & Skou, S. BioXTAS RAW: improvements to a free open-
source program for small-angle X-ray scattering data reduction and analysis. *Journal of
Applied Crystallography* **50**, 1545-1553, doi:10.1107/s1600576717011438 (2017).
- 175 Otwinowski, Z. & Minor, W. in *Methods in Enzymology* 307-326 (Elsevier, 1997).
- 176 Adams, P. D. *et al.* PHENIX: a comprehensive Python-based system for macromolecular
structure solution. *Acta Crystallographica Section D Biological Crystallography* **66**, 213-
221, doi:10.1107/s0907444909052925 (2010).
- 177 McCoy, A. J. *et al.* Phaser crystallographic software. *Journal of Applied Crystallography*
40, 658-674, doi:10.1107/s0021889807021206 (2007).
- 178 Emsley, P., Lohkamp, B., Scott, W. G. & Cowtan, K. Features and development of Coot.
Acta Crystallographica Section D Biological Crystallography **66**, 486-501,
doi:10.1107/s0907444910007493 (2010).
- 179 Afonine, P. V. *et al.* Towards automated crystallographic structure refinement with
phenix.refine. *Acta Crystallographica Section D Biological Crystallography* **68**, 352-367,
doi:10.1107/s0907444912001308 (2012).
- 180 Krissinel, E. & Henrick, K. Inference of Macromolecular Assemblies from Crystalline
State. *Journal of Molecular Biology* **372**, 774-797, doi:10.1016/j.jmb.2007.05.022 (2007).
- 181 Winn, M. D. *et al.* Overview of the CCP4 suite and current developments. *Acta
Crystallographica Section D Biological Crystallography* **67**, 235-242,
doi:10.1107/s0907444910045749 (2011).
- 182 Cheng, A. *et al.* Leginon: New features and applications. *Protein Science* **30**, 136-150,
doi:10.1002/pro.3967 (2021).
- 183 Punjani, A., Rubinstein, J. L., Fleet, D. J. & Brubaker, M. A. cryoSPARC: algorithms for
rapid unsupervised cryo-EM structure determination. *Nature Methods* **14**, 290-296,
doi:10.1038/nmeth.4169 (2017).
- 184 Zheng, S. Q. *et al.* MotionCor2: anisotropic correction of beam-induced motion for
improved cryo-electron microscopy. *Nature Methods* **14**, 331-332,
doi:10.1038/nmeth.4193 (2017).

- 185 Lander, G. C. *et al.* Appion: An integrated, database-driven pipeline to facilitate EM image
processing. *Journal of Structural Biology* **166**, 95-102, doi:10.1016/j.jsb.2009.01.002
(2009).
- 186 Pettersen, E. F. *et al.* UCSF Chimera - A visualization system for exploratory research and
analysis. *Journal of Computational Chemistry* **25**, 1605-1612, doi:10.1002/jcc.20084
(2004).
- 187 Punjani, A., Zhang, H. & Fleet, D. J. Non-uniform refinement: adaptive regularization
improves single-particle cryo-EM reconstruction. *Nature Methods* **17**, 1214-1221,
doi:10.1038/s41592-020-00990-8 (2020).
- 188 Yadav, R. *et al.* Structural insight into the dual function of LbpB in mediating Neisserial
pathogenesis. *eLife* **10**, doi:10.7554/elife.71683 (2021).
- 189 Pettersen, E. F. *et al.* UCSF ChimeraX: Structure visualization for researchers, educators,
and developers. *Protein Science* **30**, 70-82, doi:10.1002/pro.3943 (2021).
- 190 Afonine, P. V. *et al.* Real-space refinement in PHENIX for cryo-EM and crystallography.
Acta Crystallographica Section D Structural Biology **74**, 531-544,
doi:10.1107/s2059798318006551 (2018).
- 191 Anderson, B. F., Baker, H. M., Norris, G. E., Rice, D. W. & Baker, E. N. Structure of
human lactoferrin: Crystallographic structure analysis and refinement at 2.8 Å resolution.
Journal of Molecular Biology **209**, 711-734, doi:10.1016/0022-2836(89)90602-5 (1989).
- 192 Stuwe, T. *et al.* Architecture of the fungal nuclear pore inner ring complex. *Science* **350**,
56-64, doi:10.1126/science.aac9176 (2015).
- 193 Sikora, A. E. *et al.* Structural and functional insights into the role of BamD and BamE
within the β -barrel assembly machinery in *Neisseria gonorrhoeae*. *Journal of Biological
Chemistry* **293**, 1106-1119, doi:10.1074/jbc.ra117.000437 (2018).

VITA

Ravi Yadav was born in a small village in Rajasthan, India. He got his Bachelor of Technology (B. Tech) degree in Biotechnology from Indian Institute of Technology Roorkee, India in 2015. As an undergraduate student, he joined Dr. Pravindra Kumar's group and studied the lipid A biosynthesis pathway. After graduation, he continued working in the same lab, focusing on structural and computational studies of bacterial and viral drug targets. There, he solved the crystal structure of the chorismate mutase-like domain in complex with an inhibitor. He joined Purdue University as a graduate student in 2016 and continued his training in structural biology and biophysics in Dr. Nicholas Noinaj's lab. His graduate thesis work has been focused on structural and functional studies of lactoferrin binding proteins from pathogenic *Neisseria meningitidis* and *N. gonorrhoeae*. He used X-ray crystallography, cryo-electron microscopy along with site-directed mutagenesis, and binding studies to study protein-protein and protein-peptide interactions. After graduating from Purdue, he plans to continue membrane protein research.

PUBLICATIONS

- Iyamu ID, Vilseck JZ, **Yadav R**, Noinaj N, Huang R (2021). Exploring unconventional SAM analogs to build cell-potent bisubstrate inhibitors for Nicotinamide N-Methyltransferase. (submitted)
- **Yadav R**, Govindan S, Daczkowski C, Mesecar A, Chakravarthy S, Noinaj N (2021). Structural insight into the dual function of LbpB in mediating *Neisserial* pathogenesis. *eLife*, 10:e71683.
- **Yadav R**, Noinaj N, Ostan N, Moraes T, Stoudenmire J, Maurakis S, Cornelissen CN (2020). Structural basis for evasion of nutritional immunity by the pathogenic *Neisseriae*. *Frontiers in Microbiology*, 10:2981.
- Chen D, Li L, Diaz K, Iyamu ID, **Yadav R**, Noinaj N, Huang R (2019). Novel propargyl-linked bisubstrate analogues as tight-binding inhibitors for Nicotinamide N-Methyltransferase. *Journal of Medicinal Chemistry*, 62: 10783-10797.

Prior to Purdue University

- Aggarwal M, Kaur R, Saha A, Mudgal R, **Yadav R**, Dash PK, Parida M, Kumar P, Tomar S (2017). Evaluation of antiviral activity of piperazine against Chikungunya virus targeting hydrophobic pocket of alphavirus capsid protein. *Antiviral Research*, 146: 102-111.
- Pratap S[‡], Dev A[‡], Sharma V[‡], **Yadav R[‡]**, Narwal M, Tomar S, Kumar P (2017). Structure of chorismate mutase-like domain of DAHPS from *Bacillus subtilis* complexed with novel inhibitor reveals conformational plasticity of active site. *Scientific Reports*, 7 (1):6364. (‡ represents co-first authors).
- Pratap S, Kesari P, **Yadav R**, Dev A, Narwal M, Kumar P (2017). Acyl chain preference and inhibitor identification of *Moraxella catarrhalis* LpxA: Insight through crystal structure and computational studies. *International Journal of Biological Macromolecules*, 96: 759-765.

POSTER PRESENTATIONS

- 2021 Gordon Research Seminar/Conference on Cell Biology of Metals, West Dover, VT.
- 2021 The Nutrition, Immunity, and Inflammation Conference: From Model Systems to Human Trials, FASEB virtual conference.
- 2020 American Crystallographic Association (ACA) annual meeting, virtual conference.
- 2019 American Crystallographic Association (ACA) annual meeting, Covington, KY.
- 2019 Hitchhiker's Guide to Biomolecular Galaxy Symposium, Purdue University, IN.
- 2019 14th Midwest Conference on Protein Folding, Assemblies and Molecular Motions, University of Notre Dame, IN.
- 2019 OIGP Spring Reception, Purdue University, IN.
- 2019 Missouri Symposium in Molecular Biophysics, University of Missouri, Columbia, MO.
- 2018 Purdue Cryo-EM Symposium, Purdue University, IN.
- 2018 Hitchhiker's Guide to Biomolecular Galaxy Symposium, Purdue University, IN.

- 2018 13th Midwest Conference on Protein Folding, Assemblies and Molecular Motions, University of Notre Dame, IN.
- 2018 OIGP Spring Reception, Purdue University, IN.
- 2017 Department of Biological Sciences Fall 2017 Retreat, Purdue University, IN.

ORAL PRESENTATIONS

- 2021 American Crystallographic Association (ACA) annual meeting, virtual conference.
- 2021 Hitchhiker's Guide to Biomolecular Galaxy Symposium, Purdue University, IN.
- 2021 Structural and Computational Biology and Biophysics Graduate Student Spring Symposium, Purdue University, IN.
- 2021 Structural Biology and Biophysics Club (SBBC) Inaugural Symposium, Purdue University, West Lafayette, IN.
- 2019 Department of Biological Sciences Fall 2019 Retreat, Purdue University, IN.
- 2018 Hitchhiker's Guide to Biomolecular Galaxy Symposium, Purdue University, IN.
- 2018 13th Midwest Conference on Protein Folding, Assemblies and Molecular Motions, University of Notre Dame, IN.

AWARDS

- **Purdue Graduate Student Government (PGSG) travel award** to present poster at Cell Biology of Metals GRS/GRC conference, West Dover, VT (2021)
- **Second runner-up** for oral presentation at Hitchhiker's Guide to Biomolecular Galaxy Symposium, Purdue University, USA (2021)
- **Faculty Choice Award** for oral presentation at Structural and Computational Biology and Biophysics Graduate Student Spring Symposium, Purdue University, USA (2021)
- **Bilsland Dissertation Fellowship**, Purdue University, USA (2021)
- **Audience Choice Poster Prize** for poster presentation at PULSe virtual fair poster competition (2021)
- **RCSB PDB Poster Prize Honorable Mention** for poster presentation at virtual ACA annual meeting (2020)
- **Purdue Research Foundation Fellowship** for academic session 2020-21 by Executive Vice President for Research and Partnerships, Purdue University, USA (2020)
- **2019 Linus Pauling Poster Prize** for poster presentation at ACA annual meeting, Covington, KY, USA (2019)
- **Certificate of Excellence in Interdisciplinary Research (Life Sciences)** for poster presentation at OIGP spring reception, Purdue University, USA (2019)
- **Certificate of Excellence in Interdisciplinary Research (Life Sciences)** for poster presentation at OIGP spring reception, Purdue University, USA (2018)
- **Lynn Fellowship** for the academic session 2016-17 by PULSe program, Purdue University, USA (2016)